Tuning damage in porous architectured materials inspired by osteonal bone

Auteur : Depas, Cyrielle
Promoteur(s) : Ruffoni, Davide
Faculté : Faculté des Sciences appliquées
Diplôme : Master en ingénieur civil biomédical, à finalité spécialisée
Année académique : 2023-2024
URI/URL : http://hdl.handle.net/2268.2/20404

UNIVERSITY OF LIÈGE

FACULTY OF APPLIED SCIENCES

Tuning damage in porous architectured materials inspired by osteonal bone

Master thesis conducted by

CYRIELLE DEPAS

with the aim of obtaining the degree of Master in Biomedical Engineering

Academic year 2023 - 2024

SUPERVISOR: Davide Ruffoni

PHD STUDENT SUPERVISOR: Timothy Volders

JURY: Davide Ruffoni, Laura Zorzetto, Anne Mertens

Abstract

The intricate relationship between the structure, the mechanical properties and the toughening mechanisms in biological materials needs to be understood in order to develop resilient bio-inspired synthetic materials with enhanced mechanical properties.

There are many examples of biological materials around the world (*e.g.*, bone, nacre, glass sponge, teeth), that possess different mechanisms to mitigate crack propagation. Our focus is on how a porosity pattern can influence the interaction between a weak spot and a propagating crack. In our context, we draw inspiration from the osteonal bone, which employs multiple mechanisms, potentially including porosity, to protect its weak spot (*i.e.*, the Haversian canal containing its vascularisation).

The thesis therefore combines finite element simulations and additive manufacturing to study crack propagation and damage evolution. The simulations focus on notch sensitivity, hole attraction and the overall mechanical performance of the materials. The results reveal a complex interplay between material parameters that govern the damage initiation and evolution. In addition, incorporating a linear porosity pattern allows, depending on the features of the pattern such as pore spacing, to program the cracking behaviour by guiding cracks along predetermined paths. Although one week interface allows to deviate the crack, it does not improve the overall toughness of the system, suggesting that more weak interfaces may be combined, as seen in numerous biological materials.

To translate the computational models into physical prototypes, an additive manufacturing technique is employed, specifically PolyJet 3D printing. This method enables precise control over the microstructure and porosity of the materials, facilitating the creation of samples that closely align with the modelled designs. This experimental part thus involves designing, manufacturing and testing these samples to observe the damage evolution and fracture patterns. The results appear to corroborate the computational results.

Overall, this interdisciplinary approach, combining bio-inspiration with numerical simulations and an additive manufacturing technique, holds promise for the development of novel damage-tolerant materials for biomedical and engineering applications, motivating further research in this field.

Keywords: Biomimicry, Bio-inspired materials, Finite element simulation, 3D printing, Mechanical testing, Crack propagation, Mechanical properties, Damage-tolerant materials.

Acknowledgements

This work gave me my first insight into the world of research and allowed me to apply the knowledge and skills I have acquired throughout my academic career. Working on this long-term project has been an incredibly rewarding experience. However, this thesis was made possible by the precious support of a number of people, to whom I would like to express my deepest gratitude.

First of all, I would like to sincerely thank my supervisor, Professor Davide Ruffoni, for his mentorship, expertise, availability, patience and trust throughout this research project. His wise advice and support during our biweekly meetings guided and helped me find solutions to move forward. His enthusiasm for my work greatly motivated me during the realisation of this thesis.

Thanks also to the members of my jury for agreeing to serve, for taking the time to review this thesis and for attending my defence.

Additionally, I would like to hugely thank Timothy Volders, the PhD student who supervised me and provided the subject of my master thesis. He was always present to guide me through various aspects of the project, from the explanation about how to use the software and conduct experiments, to the analysis of the results and the redaction of the thesis. His judicious comments and suggestions greatly helped me to improve the quality of my work. I am therefore deeply grateful for his constant kindness and support during the year, his patience in challenging moments and his availability to answer my countless questions at any time.

Finally, I would like to personally thank all the other people who, directly or indirectly, contributed to the achievement of my thesis, whether through enriching discussions, advice or simply their presence. I am grateful to all the PhD students of the Mechanics of Biological and Bioinspired Materials Laboratory (University of Liège) for their reassurance, useful advice and enlightening opinions during the lab meetings. Special thanks also to my family and friends for their unwavering support throughout the ups and downs of this project, for their encouragement and for always believing in me.

Contents

Introduction

Today, biomimicry offers a unique perspective on natural design principles, via refinement over millions of years, to inspire innovative solutions to human challenges and technological advancements. Recently, the study of biological materials has attracted significant attention due to their microstructures and remarkable mechanical properties, that often exceed those of their individual components by orders of magnitude. This growing interest has paved the way for bio-inspired material design, which holds great promise for the creation of innovative multifunctional materials with diverse technological applications [1, 2].

Many biological materials are in fact composites, integrating both stiff inorganic and soft organic components arranged in a hierarchical structure from the molecular to the macrostructural level. Most importantly, nature has the ability to combine the advantageous properties of these components, which often seem contradictory; a feat that remains a challenge for engineers. In general, strong/stiff materials are brittle, while tough materials are weak [3]. However, nature manages to strike a balance of high toughness, high stiffness and high strength. Among others, bone is a fascinating biological structure from which we can draw inspiration [1, 2].

This thesis is divided into five main chapters. The first chapter provides a theoretical explanation of concepts relevant to our subject. At the beginning, the performance of monolithic and architectured materials is compared. Fundamental notions about the hierarchical structure and toughening mechanisms found in various biological materials (*e.g.*, bone, nacre, glass sponge and teeth) are then described. Following this, several research articles are reviewed to illustrate how damage modelling in bio-inspired materials can be carried out in order to support the relevancy of this study. Next, a brief explanation of the operating principles of the 3D printing process of interest, along with some practical applications, is presented. Finally, the main aims of the master thesis are introduced in detail.

The two next chapters are entirely dedicated to 2D damage finite element simulations conducted on simplified models inspired by the osteonal bone structure, including a pre-existing notch [4]. The second chapter explores how changes in model material properties affect crack propagation, in terms of progressive damage evolution and failure. The third chapter investigates the impact of structural changes on crack propagation, introducing a porosity pattern in the previous models, to determine if we are able to program cracking behaviour by guiding the crack through the pores.

The fourth chapter describes mechanical tests conducted on 3D-printed samples, serving as a proof-of-concept study to support and hopefully validate the computational results. The main objective is to observe damage propagation and fracture patterns.

The last chapter discusses the main results of this master thesis and suggests ideas for possible future researches.

Chapter 1

Theoretical background

The objective of this chapter is to introduce the general context of this project. The first section compares the toughness capacities of monolithic materials with architectured materials. The second section details examples of architectural and material features that confer to the biological materials an outstanding fracture resistance. This is followed by an explanation of the general strategy from which this research draws inspiration. Since our study focuses on the modelling and printing of bio-inspired materials, the next two sections describe different approaches already explored in the literature. Finally, the main aims of the thesis are described in a last section.

1.1 Monolithic vs. Architectured materials

A monolithic material is essentially a solid block lacking any internal microstructure, where toughness is determined by the energy required to propagate a crack within it. In contrast, an architectured material consists of monolithic phase arranged into distinct stiff and hard building blocks with well-defined shapes, bonded by weaker interfaces. This configuration resembles a puzzle and positively alters the mechanical response of the material, particularly in fracture behaviour.

While toughness in monolithic materials remains constant regardless of crack length ratio, architectured materials can increase their toughness with crack propagation (Fig. 1.1). In fact, the crack tends initially to follow the path of least resistance along the weak interfaces surrounding the building blocks, leading to less energy demand than in monolithic materials. However, as crack propagates, the weaker interfaces can trap and guide the crack along a finer path, necessitating higher energy. This redirection of cracks into configurations where additional mechanisms prevent their further propagation enhances toughness, stabilising the material against damage and flaws [5]. Furthermore, if the interfaces can deform significantly and dissipate energy, quasi-ductile behaviours may emerge compared to the brittle behaviour of monolithic materials [6].
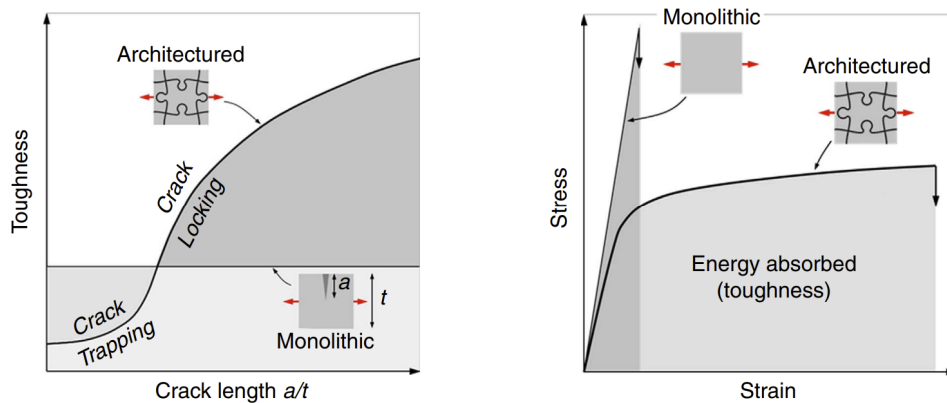

Figure 1.1: Comparison between a monolithic and an architectured material in terms of toughness, potential deformation and energy absorption capabilities [6].

1.2 Crack propagation and toughening mechanisms in biological materials

Biological materials exhibit sophisticated hierarchical architectures spread over multiple length scales. They were honed over millions of years of evolution to achieve outstanding mechanical properties that synthetic materials often struggle to match. Their remarkable combination of stiffness, lightweight, strength and toughness provides a unique source of inspiration for scientists, offering potential innovative solutions for the design and optimisation of the next generation of engineering materials. Hence, this section seeks to unravel the secrets behind the performance of biological materials such as bone, nacre, glass sponge and teeth, showcasing their impressive toughness, durability, damage resistance and even quasi-ductile characteristics.

1.2.1 Bone

Bone is a multi-functional endocrine organ metabolically active and capable of adapting its structure in response to changes in mechanical environmental constraints, thanks to its renewal and self-healing capabilities. With tendons, ligaments, joints, cartilage, muscles and other connective tissues, they constitute the musculoskeletal system. Among all the functions it fulfils, it gives the structural support of the body (facilitating locomotion by acting as levers for the muscles), protects vital organs, provides a medium for haematopoiesis and serves as a reservoir for minerals and growth factors, playing a role in homeostasis by maintaining the acid-base and mineral balance [7, 8, 9, 10].

Bone is organised as a hierarchical material formed by the progressive organisation of building blocks across different length scales (Fig. 1.2) [7, 8, 11]. At the macroscale, the structure differentiates into compact/cortical bone (*i.e.*, dense material mainly found at the surface of all bones) or spongy/trabecular bone (*i.e.*, interconnected foam-like network of stress-oriented 100–300 μm thick trabeculae [12, 13]).

Cortical bone is microscopically composed of a lamellar structure organised into osteons or Haversian systems. They consist of regular concentric fibre-reinforced lamellae (typically 10–15 in number, each about 3–7 μm thick) [8, 12, 14, 15], embedded into a more mineralised matrix made of interstitial lamellae [16]. Each osteon looks like a hollow cylinder, approximately 100–200 μm in diameter and 1–3 mm in length, which runs along the longitudinal axis of the bone [7, 17, 18, 19]. It thus has an inner central canal, called the Haversian canal (around 80 μm in diameter [18]), which serves as a protective conduit for blood vessels, lymphatic vessels and nerves. In cortical bone, porosity also manifests by the lacuno-canaliculi network (0.5 μm in diameter and 5–8 μm in length), which houses the osteocytes in unmineralised spaces between the lamellae. This network allows the exchange of nutrients and the removal of metabolic waste. Finally, the osteon is surrounded by a softer outer layer, called the cement line, measuring 1–5 μm in thickness [7, 20].

Each individual osteon lamella is composed of fibres arranged in geometric patterns similar to a positive spiral with a fibre angle changing from ∼10–60° relative to the longitudinal axis of the osteon, resulting in a rotated plywood structure [19, 21, 22]. This structural feature allows bones to adjust the material properties of osteons locally, enhancing energy absorption and crack resistance [7].

Each fibre is then a bundle of mineralised collagen fibrils. These ones are composite materials where tiny mineral crystals effectively fill and coat collagen fibrils in a staggered arrangement with a periodicity of 67 nm [14, 23, 24]. Collagen fibrils are made from collagen type-I molecules, known as tropocollagen (1.5 nm in diameter and 300 nm in length [12]), formed by three chains of amino acids bound together into a triple-helical arrangement via hydrogen bonds. The mineral crystals are mainly composed of calcium phosphate-based hydroxyapatite [$Ca_{10}(PO_4)_6(OH)_2$] and appear as tiny platelets ($50 \times 25 \times 3$ nm) that initially nucleate in gap spaces between collagen fibrils [7, 25, 26].

The organic and inorganic components of bone have contrasted mechanical properties: minerals are stiff and brittle, while collagen is soft and tough. However, the composite structure combines the advantageous properties of both constituents (*i.e.*, high stiffness and high toughness), allowing bones to resist breaking during daily activities. Essentially, bone mineral provides mechanical rigidity and load-bearing strength, while bone collagen imparts tensile strength, elasticity and flexibility [7, 11, 12, 14, 25].
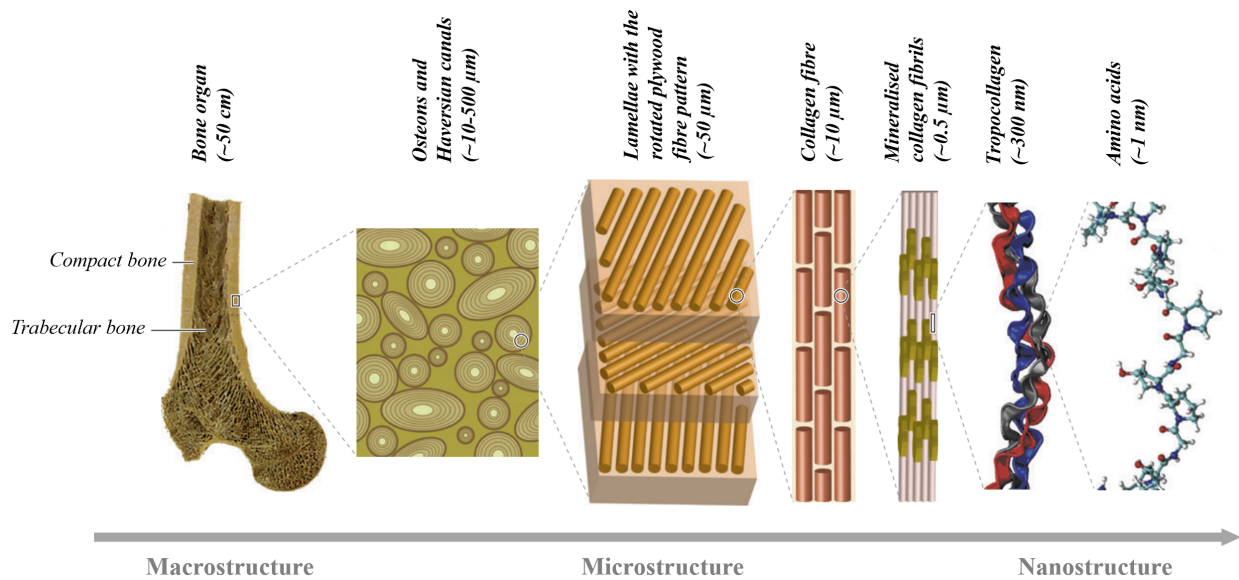
Figure 1.2: Hierarchical organisation of the bone structure (adapted from [27]).

Bone employs various toughening strategies to mitigate and arrest crack propagation and avoid catastrophic failure [28]. Bone resistance to fracture operates across multiple length scales, with each level of its structure finely tuned to enhance toughness. In principles, toughness is defined as the ability of a material to dissipate deformation energy without crack propagation. Crack toughening mechanisms in bone can be classified into intrinsic and extrinsic domains, though acting simultaneously [27].

Intrinsic toughening mechanisms increase the bone resistance at the crack tip during crack initiation and the early stage of crack propagation by promoting ductility and creating plastic zones to safeguard the overall structure [29, 30]. Specifically, intrinsic toughening relies on the energy needed for collagen molecules to unclamp and slide past each other, on the formation of nano/microcracks inside the collagen fibrils, and on sacrificial hydrogen-bonds within or between collagen molecules that break to dissipate energy and reform once the load is removed (Fig. 1.3 up) [31].

Extrinsic shielding mechanisms aim to mitigate crack growth by decreasing the applied crack-driving force behind the crack tip [29, 32]. Four types of mechanisms exist (Fig. 1.3 down): crack deflection and twisting, uncracked-ligament bridging, intact collagen-fibril bridging and constrained microcracking (that primarily develops around the main crack to decrease local stress concentration).

Figure 1.3: Intrinsic and extrinsic fracture-toughening mechanisms in cortical bone (adapted from [27]).

The anisotropic strength of cortical bone can be understood by examining crack propagation along its main axes. Crack trajectories are in fact determined by the interplay between the direction of the maximum driving force and the path of weakest microstructure resistance. In cortical bone, the interfaces of osteons, known as cement lines, seems to provide weak pathways prone to cracking due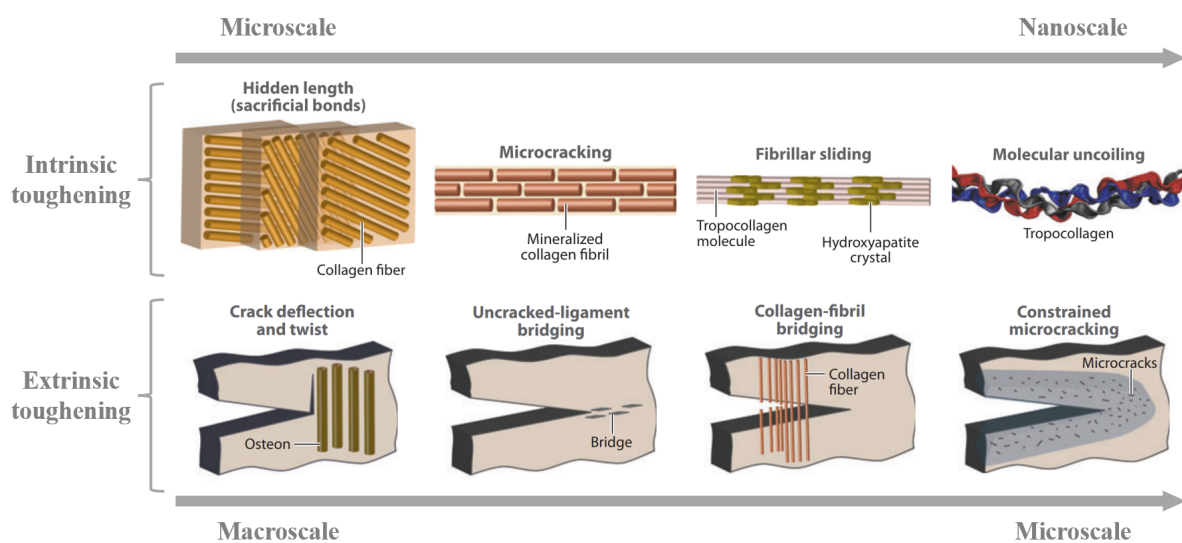 to their hypermineralised composition [33, 34, 35]. These regions thus serve as favoured sites for the formation of microcracks which seems to emerge from the fracture of hydroxyapatite crystals surrounding collagen fibres or from delamination at the interfaces between crystals and fibres [36].

For a transverse crack propagation, the cement lines tend to be perpendicular to the crack trajectory. This configuration induces multiple crack deflections and twists that lead to an extremely rough fracture surface (Figs. 1.4a–e). This highly tortuous crack path contributes to significant energy dissipation and ultimately results in high toughness [27]. In addition, the concentric layer system of lamellar bone plays a crucial role in strengthening bone and inhibiting crack propagation. The mineralised collagen fibrils demonstrate remarkable energy dissipation ability under axial loading, acting as barriers to crack advancement, consequently enhancing bone toughness [37].

Conversely, for a longitudinal crack propagation, the cement lines align roughly parallel to the growing crack. Here, the crack tends to propagate along the cement lines, resulting in a relatively smoother fracture surface (Figs. 1.4f–j). Furthermore, the fusion of microcracks with the main crack creates uncracked regions that bridge the crack, helping in load support and simultaneously reducing the energy required for additional crack propagation [33, 34, 38]. Although this mechanism of uncracked-ligament bridging contributes to toughening, its efficacy is inferior to the one of crack deflection and twisting.
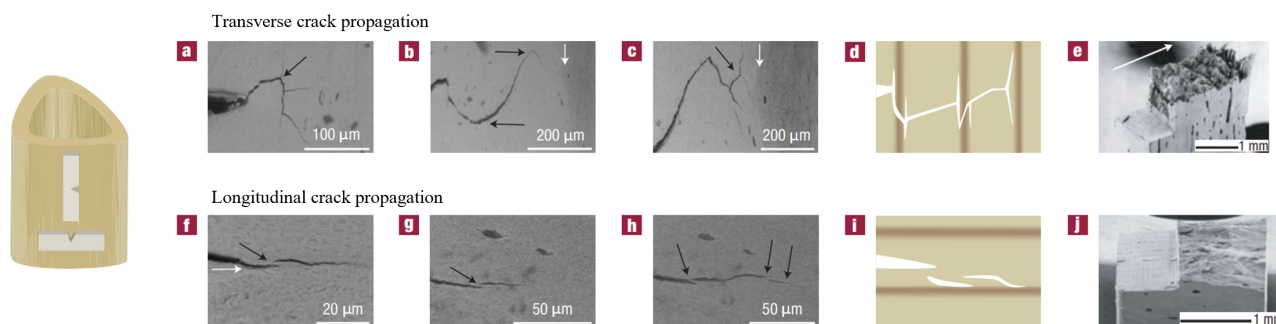
Figure 1.4: Crack propagation in a cortical bone sample for three different crack lengths in the (a–c) transverse and (f–h) longitudinal directions, (d,i) schematic representations and (e,j) fractography images (adapted from [33]).

1.2.2   Nacre from mollusc shells

Mollusc shells are an example of high-performance biological materials, offering vital protection for the organisms they house. These shells are primarily composed of calcium carbonate-based biominerals that are glued together by biopolymer adhesives. Among the diversity of shell arrangements proposed in [39], nacreous structures stand out for their exceptional strength and resilience.

The mollusc shell is structured as a two-layer armour system (Fig. 1.5). It comprises an outer prismatic layer, characterised by rigid but brittle calcite crystals, and a softer inner layer known as nacre. The microstructure of nacre resembles that of a brick-and-mortar pattern, due to its geometric similarity to masonry. In fact, nacre is an inorganic/organic composite material that primarily consists of 95 vol.% of microscopic mineral tablets ("bricks"), mainly made of aragonite ($CaCO_3$). These tablets have a polygonal flat shape measuring 0.4–0.5 μm in thickness and 8–10 μm in width. They are bound together in a staggered arrangement by a very small amount of softer organic materials ("mortar"), composed of chitin and proteins (20–50 nm thick) [40, 41, 42, 43].

Compared to the brittle failure of aragonite under tension, nacre demonstrates remarkable ductility (Fig. 1.6). This underscores how the optimal arrangement of aragonite in the nacrous architecture can impart toughness and ductility to the material, despite the brittle mechanical properties of its individual components. In fact, nacre is 3000 times tougher than monolithic aragonite [44].

Figure 1.5: Mollusc shell layers and crack propagation in nacre [6].

Figure 1.6: Tensile stress-strain curves for aragonite and nacre, and nacre associated deformation mode [42].

In nacre, cracks propagate along the soft interfaces, being systematically deflected by the mineral tablets. This crack deflection creat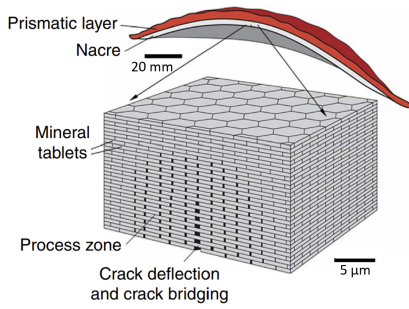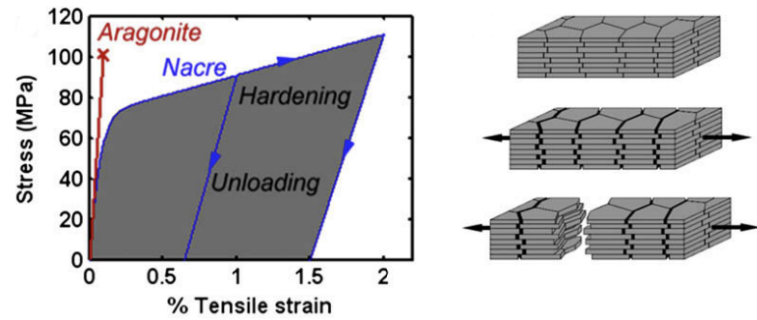es a highly tortuous crack path, which dissipates a huge amount of energy and enhances toughness [6, 45]. This behaviour is attributed to tablet sliding, which is caused by the shear yielding of the interfaces once the elastic limit is surpassed. This sliding produces local deformations that spread throughout the specimen. When the sliding potential of the tablets is exhausted, failure occurs by tablet pullout [46].

As illustrated in Fig. 1.5, in the process zone behind the crack tip, the tablets stay in contact and interact via mechanisms that resist sliding and exert closure forces to prevent further crack propagation (Fig. 1.7) [47, 48]. The interlocking of tablets and nanoasperities present on opposing tablet surfaces provide frictional resistance to sliding as the interface shears [46, 49]. Then, the molecular chains of the organic material can elongate and unfold, maintaining cohesion between tablets over long sliding distances [5]. The presence of mineral bridges may also reinforce the interfaces, since sliding requires the rupture of these bridges, which introduces additional frictional resistance [50].
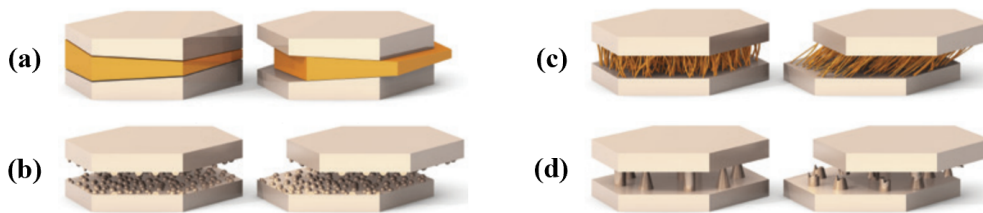
Figure 1.7: Nanoscale mechanisms controlling the sliding of the mineral tablets: (a) tablet interlocking during sliding, (b) aragonite asperities contact, (c) organic layer acting as viscoelastic glue and (d) breaking of mineral bridges [1].

1.2.3 Glass sponge

The inorganic sea sponge spicule also illustrates the remarkable ability of nature to design complex composites from relatively weak components. Despite being made of glass, individual spicules of the glass sponge possess both optical properties and structural resistance, exhibiting exceptional flexibility and toughness [51].

The skeleton of the sea sponge *Euplectella sp.* (Fig. 1.8a) presents a cylindrical cage-like structure made of glass with lateral openings. Anchored into soft sea floor sediments, the basal segment is loosely connected to the rigid cage. This configuration is finely tuned to withstand ocean currents and also houses breeding shrimps, forming a symbiotic relationship where the shrimps clean the cage while finding refuge from predators [52].

Reinforced by external ridges that spiral the cage at an angle of 45°, the surface of the cylindrical structure is composed of a regular square-grid lattice of vertical and horizontal struts, with diagonal elements positioned in every second square cell (Figs. 1.8b–c). Cross-sectional analysis reveals that each strut is made of a bundle of silica spicules embedded in a layered silica matrix (Figs. 1.8d–f). These spicules consist of concentric lamellae, with decreasing layer thickness from the centre to the periphery (Fig. 1.8g), which are separated by a thin organic interlayer (Fig. 1.8h). At the nanoscale, the basic building block of a glass sponge consists of consolidated hydrated silica nanoparticles (Fig. 1.8i) [53].

Figs. 1.8j–k show the fracture surface of a sponge spicule with its corresponding crack path. Indeed, the onion-like layers similar to osteons in cortical bone act as crack stoppers, deflecting cracks and absorbing energy at their organic interfaces. The stepwise shape of the crack path thus indicates that cracks cannot travel in a straight path, enhancing toughness over a monolithic material [51, 53].

Figure 1.8: Investigation into the structural composition and fracture resistance of *Euplectella sp.*'s skeleton. (a-c) Cylindrical cage-like structure. (d-f) Bundle of silica spicules embedded in a layered silica matrix. (g-i) Sili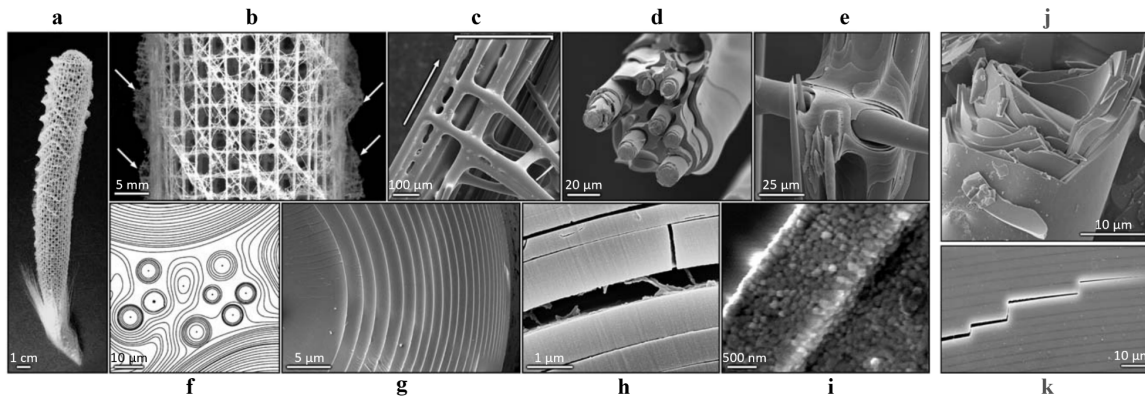ca lamellar structure separated by a thin organic interlayer. (j-k) Fracture surface of a spicule with its crack path [53].

1.2.4 Teeth

The tooth is a very resilient structure made up of two layers, primarily consisting of collagen fibres and hydroxyapatite crystals [54]. The arrangement and concentration of these organic and inorganic components are meticulously regulated throughout the material. Indeed, the structure of the tooth is designed to provide a hard external layer capable of withstanding mastication forces and a tougher internal core. Being the hardest tissue in the human body, the outer enamel layer is composed of highly mineralised collagen fibres (with 95 vol.% hydroxyapatite content) aligned in long rods perpendicular to the tooth surface [55]. In contrast, the inner dentine layer is made of less mineralised collagen fibres (with 50 vol.% hydroxyapatite content) oriented mainly parallel to the tooth surface. The transition zone between these two layers, known as the dentine-enamel junction, shows a gradual change in the orientation and concentration of these building blocks [56].

The intricate microstructure of the tooth plays a pivotal role in how it handles stress and strain, affecting its resistance to fracture (Fig. 1.9). When the tooth is subjected to mastication forces, cracks typically initiate from the enamel surface. However, the enamel layer has very low resistance to crack propagation, similar to that of glass [54]. Therefore, to prevent that a piece of enamel goes away, cracks are channelled away from the surface along the parallel rods. As cracks progress deeper into the enamel and reach the dentine-enamel junction, the rods bend and criss-cross to form a complex decussation that creates tortuous and deflected crack paths and hinders further crack growth [55]. In addition, the intact regions between the microcracks act as uncracked-ligament bridges that effectively stop cracks to prevent catastrophic failure [57, 58]. Consequently, the structural design of the dentin-enamel junction provides a crack-arrest barrier for flaws formed in brittle enamel, leading to a notable increase in the material fracture toughness.
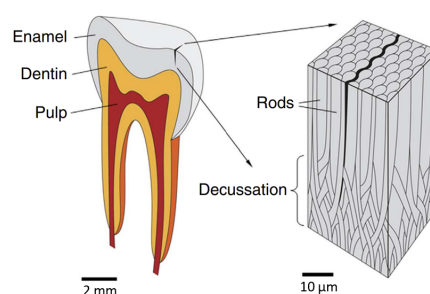
Figure 1.9: Structure and crack propagation in tooth enamel [6].

11

1.3 General concept: Overcoming the brittleness of glass

F. Barthelat et al. [6] aimed to improve glass toughness and its ability to deform. Their methodology involved inducing weak interfaces within the glass bulk through 3D laser engraving.

Initially, they fabricated glass samples including a pre-existing notch to evaluate the fracture toughness at the engraved interface, which comprised a series of equi-spaced micro-defects along the anticipated crack path (Fig. 1.10a). In fact, the change of defect size or spacing allowed them to fine-tune the interface toughness (Fig. 1.10b). As a result, when the defects were very closely spaced (numerous defects), they fused together during engraving without any external loading, causing the sample to break in two pieces and thus decreasing the interface toughness completely. In contrast, with greater spacing up to 130 μm (fewer defects), the interface toughness was improved. However, if the spacing between defects exceeded 130 μm, defects remained unaltered under external loading, leading to an apparent toughness similar to the one of intact glass.

After tailoring fracture specimens to have an interface with half the bulk glass toughness, they explored the impact of the interface inclination (Figs. 1.10c–d). They observed that the crack could be deflected along the weak interface within an angle range of 0° to 60°. Beyond a critical angle of 70°, the crack ignored the weak interface and propagated straight into the bulk glass. As predicted, the apparent toughness increased with bigger angles, ranging from half the glass toughness at 0° to the intact glass toughness at 70°.

In summary, crack deflection was achievable when the interface toughness was sufficiently lower than the bulk material toughness, and if the deflection angle was not too large. Moreover, adding only one weak interface was not enough to increase the material toughness. Hence, they employed alternative approaches detailed in the referenced article.

Figure 1.10: (a) Glass compact tension fracture specimen. (b) Effect of defect spacing on the fracture toughness of the interface. (c) Crack deflection investigation. (d) Apparent toughness as a function of the interface angle [6].

1.4 Modelling of damage in bio-inspired materials

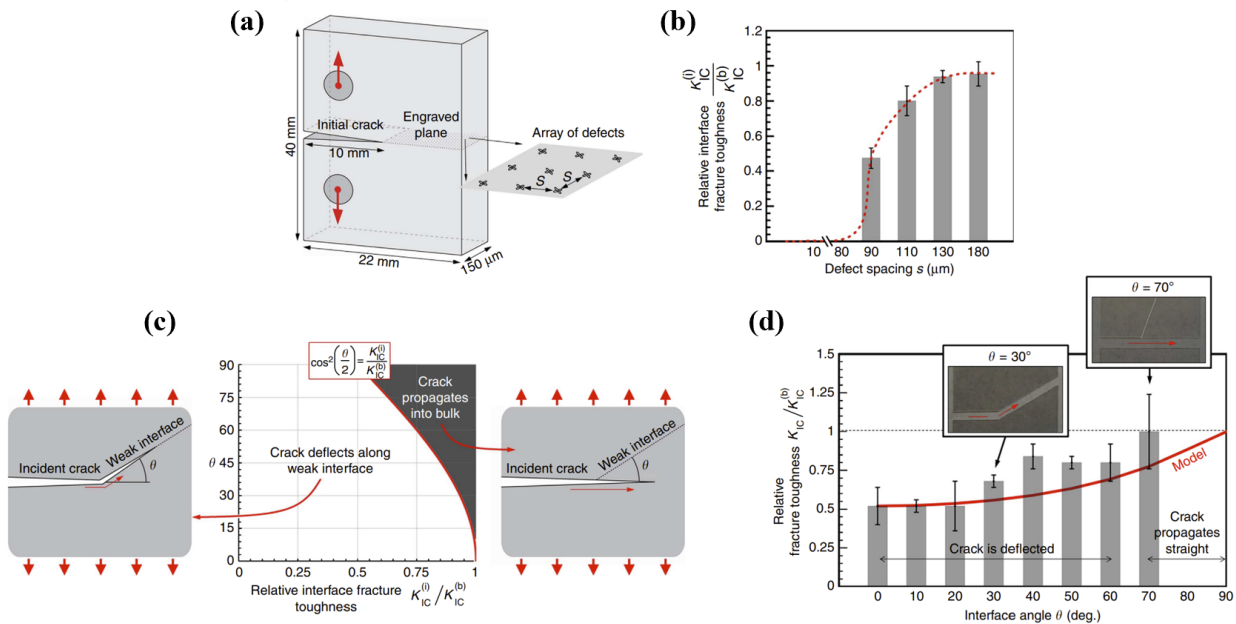In the previous sections, we demonstrate the ability of biological materials to obtain outstanding toughness properties thanks to their intricate architecture spanning over multiple length scales. Those architectures often combine hard building blocks and soft interfaces, allowing the material to control the crack propagation and increase the energy required for its propagation. This section aims to review some numerical methodologies and present researches that identified key toughening mechanisms from biological materials, and studied why and how they improve toughness using computer simulations.

1.4.1 Review of methodologies

Accurate simulation of fracture behaviour, including crack nucleation and propagation, is essential for analysing the integrity and durability of various materials and structures. A.E. Vellwock and F. Libonati [59] reviewed multiple approaches to illustrate the application of the extended finite element method (XFEM) to various bio-inspired materials. Here are some examples.

An interesting application of XFEM is the study of cortical bone. S. Li et al. [60] demonstrated that the cement line enhanced the material fracture toughness by deflecting and arresting cracks more effectively when its elastic modulus was 25% lower than that of the osteon (Fig. 1.11a). However, this finding was based on simplified models using perfectly circular osteons. In contrast, D. Yin et al. [61] explored more complex scenarios by simulating osteons of varying shapes (circular or elliptical) and orientations under constant pressure conditions from the interstitial matrix and Haversian canal. Their study revealed that, by changing the pressure from 8 MPa to 14 MPa, elliptical osteons could alter the crack path and mitigate material failure by guiding cracks along the annular direction rather than towards the Haversian canal (Fig. 1.11b).
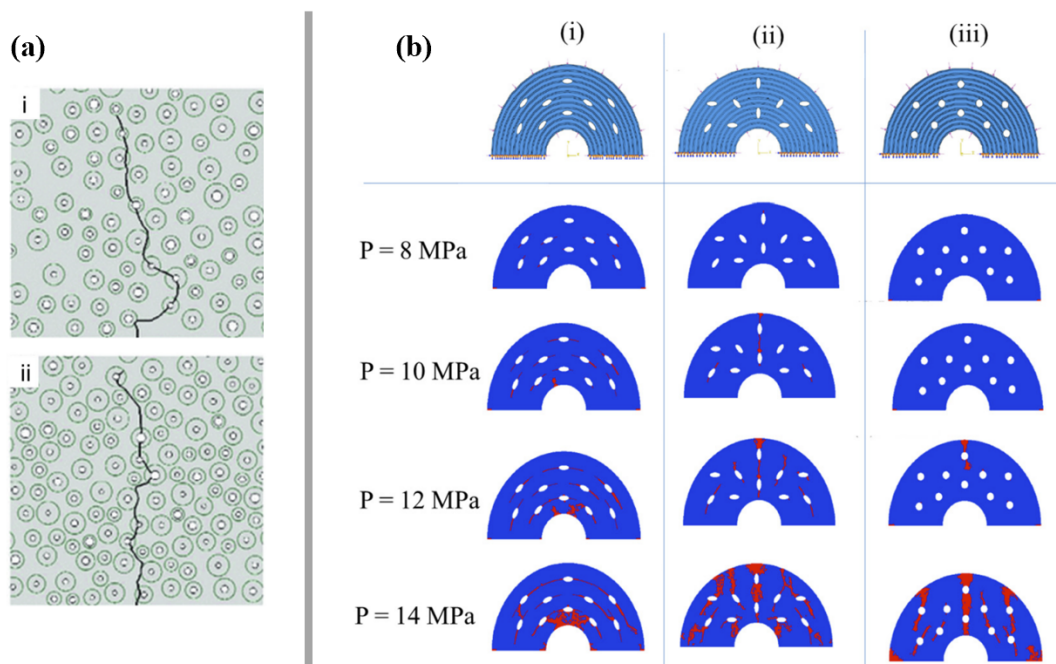
Figure 1.11: XFEM fracture analysis of cortical bone. (a) Crack propagation in cortical tissue with different cement line elastic moduli: (i) 25% lower vs. (ii) same as osteon [60]. (b) Influence of the interstitial matrix and Haversian canal pressure on the crack behaviour in osteons with (i) annular elliptical, (ii) random elliptical and (iii) circular lacunae structures [61].

XFEM has also proved its utility in dentistry. Z. Zhang et al. [62] studied the fracture resistance of molar teeth with carious lesions to identify the most effective restoration technique. Through 3D XFEM simulations, they compared conservative and invasive restoration methods, finding that conservative approaches preserved more material and thus better maintained the tooth fracture resistance. Similarly, Y. Zhang et al. [63] employed 3D XFEM modelling to show how cracks propagate in natural teeth under increasing bite forces (Fig. 1.12).
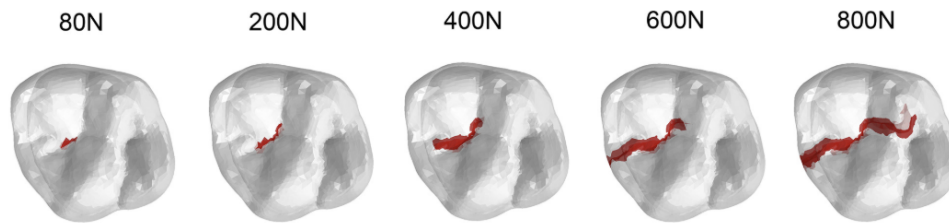
Figure 1.12: Crack propagation in a natural tooth with growing bite forces (from 80 N to 800 N) [63].

Furthermore, several other numerical methods are available for the field of bio-inspiration, each with its own advantages and limitations. Notable examples include the contour integral method (CIM), virtual crack closure technique (VCCT), cohesive zone model (CZM) and phase-field model (PFM). These methods offer trade-offs between accuracy, computational efficiency and ease of implementation. Selecting a finite element simulation technique for modelling damage in a structure depends on the objective of the study and a number of factors, such as the type of material (brittle or ductile), the material behaviour (elasticity, plasticity and/or viscoplasticity), the type of deterioration (crack initiation and/or propagation) and the loading conditions (static or dynamic), among others.

1.4.2 Concrete application to lamellar bone

H. Razi et al. [64] aimed to investigate whether the lamellar bone structure enhances toughness not only by energy dissipation through microcracking but also by decreasing the material susceptibility to cracks. They conducted 2D finite element simulations on a basic layered material model to analyse how layering affects crack propagation. Specifically, lamellar bone was modelled as a periodically inhomogeneous material with layers having varied mechanical properties and fibre orientation. These material properties were derived from previous experimental data, where variations in Young's modulus and strength were determined based on the composite anisotropy and the fibre orientation was defined along the axis perpendicular to the layers. Afterwards, this model was compared to another model featuring homogeneous average material properties. To simulate the damage propagation, a ductile damage plasticity model was used. This approach combines two key parameters: one for the damage initiation phase (the fracture strain) and one for the damage evolution (the energy release rate upon fracture). In fact, this model is also the one on which we will base our computational study.

Fig. 1.13a depicts the damage initiation, indicated by plastic deformation (in blue), and crack propagation, where elements have lost their stiffness and failed (in red), in tensile specimens including a notch. Homogeneous materials showed continuous plastic deformation and straight crack propagation, while in inhomogeneous materials, deformation and damage were discontinuous with crack splitting and damage occurring between layers. In addition, damage appeared more widespread in inhomogeneous materials, indicating greater energy dissipation compared to homogeneous materials. These observations were supported by the reaction force versus displacement curves (Fig. 1.13b). They showed that the reaction force and the critical displacement at failure were generally higher in inhomogeneous materials, except for one specific scenario (highlighted in yellow) where both materials reached the same plastic limit load.

Moreover, Fig. 1.13c provides the influence of different notch sizes on the mechanical response and toughness of the system. They saw that the periodic inhomogeneity mitigated the negative effects of large cracks on intrinsic properties. Hence, layering reduced stress concentration at the crack tip, resulting in a slower decline of nominal strength. This improvement was less pronounced for very small cracks near defect-free materials.

In summary, finite element simulations revealed that both strength and toughness were greater in the lamellar material compared to a homogeneous material with equivalent properties. This underscored the efficacy of lamellar plywood-like structures observed in bone, which adopt a damage-tolerance strategy by incorporating variations in material properties rather than maintaining uniform homogeneity.
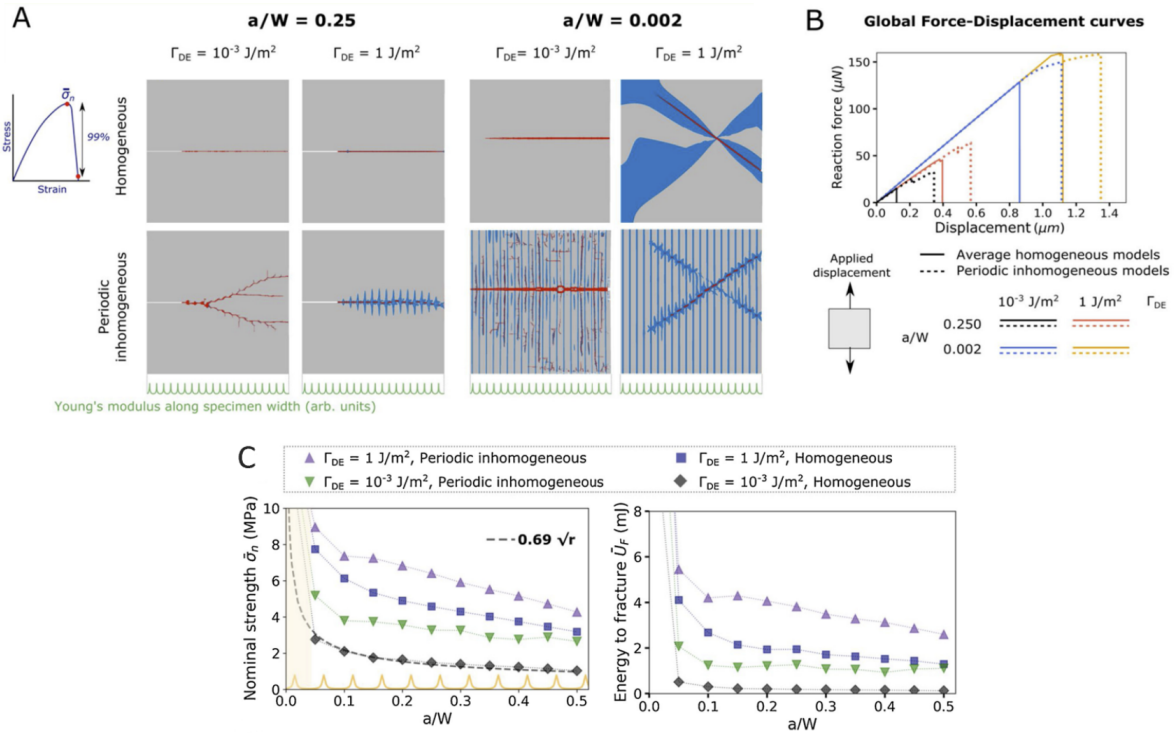
Figure 1.13: (A) Crack and damage propagation patterns. (B) Reaction force vs. displacement curves. (C) Nominal strength and energy to fracture vs. crack length curves (adapted from [64]).

1.4.3 Voids in crustacean dactyl clubs

S. Yin et al. [65] looked at the remarkable evolution of crustaceans, which have developed robust exoskeletons to resist attacks and even wield offensive weapons. Specifically, they focused on the dactyl clubs of *Odontodactylus japonicas*, highlighting the importance of the periodic region in absorbing energy during impacts. This region showed a distinct architecture with numerous randomly distributed elliptical voids.

One of their objectives was to explore the contribution of these voids to toughness using finite element modelling. To achieve this, the researchers investigated unidirectional fibre-reinforced composites containing matrix voids. They constructed 2D finite element models subjected to compact-tension loading, oriented either perpendicular or parallel to the fibres, with a notch present in the matrix (Fig. 1.14).

In case I, the crack propagated perpendicular to the fibres in the voided system. Initially, the crack moved towards the first fibre-matrix interface, but it deflected when it encountered the first void, subsequently travelling through adjacent voids. In case II, the crack progressed parallel to the fibres, with voids positioned between them. Here, the crack path went between two fibres, interacting with each void along its trajectory. Voids near the crack tip expanded and tended to coalesce, inducing plastic deformation in the surrounding matrix.

In summary, finite element modelling revealed that voids expanded and coalesced under loading, influencing in turn the fracture pattern. The analysis underscored the role of void collapse and associated microcracking in enhancing composite impact resistance.

Figure 1.14: Morphology of *Odontodactylus japonicas* with a SEM image of coronal section in periodic region and finite element modelling of unidirectional fibre-reinforced composites containing matrix voids [65].

1.5   Additive manufacturing and testing of bio-inspired materials

This thesis consists mainly of computer simulations but also includes some 3D printing and experimental tests. The traditional advantage of additive manufacturing lies in its ability to produce complex shapes. Nonetheless, the majority of 3D printing systems are constrained to u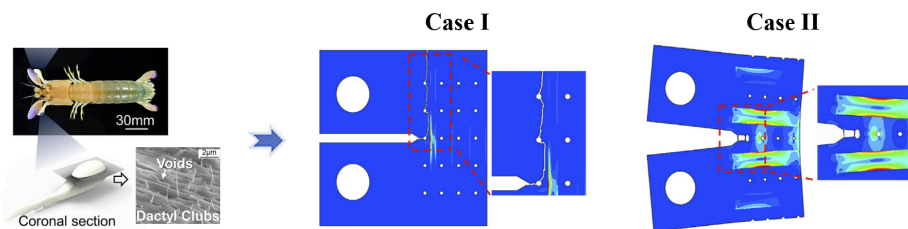se only one material, resulting in a performance exclusively dictated by geometry. Recently, diverse methods have been investigated to enable the fabrication of multimaterial structures through 3D printing technologies. This unique ability allows the creation of complex geometries with locally tuned chemical compositions, microstructures and mechanical properties within the same structure. In this work, a commercially mature technique, known as PolyJet 3D printing, is used to construct our samples. The aim of this section is to describe the principle behind this technique and to present some approaches using this technology, combined with mechanical testing, that have been explored in the literature to replicate nature design principles in the fabrication of synthetic bio-inspired composite materials.

1.5.1   Principle of PolyJet 3D printing

This 3D printing method consists in building parts layer by layer, guided by a computer-aided design, through a combination of inkjet technology and photopolymerisation (Fig. 1.15). Initially, tiny droplets (measuring 40 μm in diameter) of different liquid photo-curable polymers are deposited onto a built tray via a series of piezoelectric inkjet print heads. A roller then flattens the deposited droplets into a layer, which is then exposed to ultraviolet (UV) lamps to solidify the material by creating crosslinks between monomers. The build tray moves then down and the process repeats, layer by layer, until the entire object is fabricated. This iterative approach enables the creation of complex cm-sized structures with properties spatially tuned at the μm level [66, 67, 68].

Here are the essential technical specifications of the printer. The printer offers a resolution of 42 μm along the *x*-axis, 84 μm along the *y*-axis and 32 μm along the *z*-axis. The printer can create horizontal build layers as thin as 16 μm. Lastly, the maximum build size dimensions are $255 \times 252 \times 200$ mm [69].
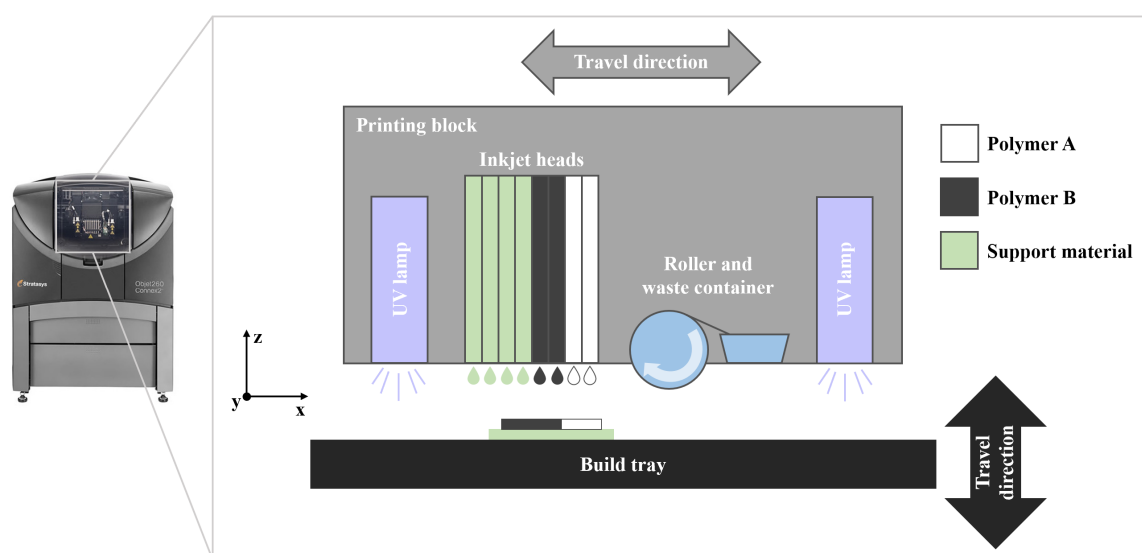
Figure 1.15: Scheme of the PolyJet printing process.

Photopolymerisation serves as a mechanism for the fabrication of highly-crosslinked polymer networks. It involves exposing liquid photosensitive thermoset resins to concentrated UV light sources, thereby inducing their solidification (Fig. 1.16). Photopolymers consist of a blend of monomers and oligomers, to which photoinitiators are added to initiate the reaction through their decomposition and inhibitors to prevent excessive polymerisation during storage (caused by ambient UV radiation).

Essentially, UV light cleaves the photoinitiators which produce free radicals (*i.e.*, molecules with free electrons). These radicals trigger a chain reaction by bonding with the monomers present in the resin. Subsequent exposure to light generates additional radicals on the newly incorporated monomers, promoting further monomer attachment. This cycle continues, facilitating the progressive growth of the polymer network [70].
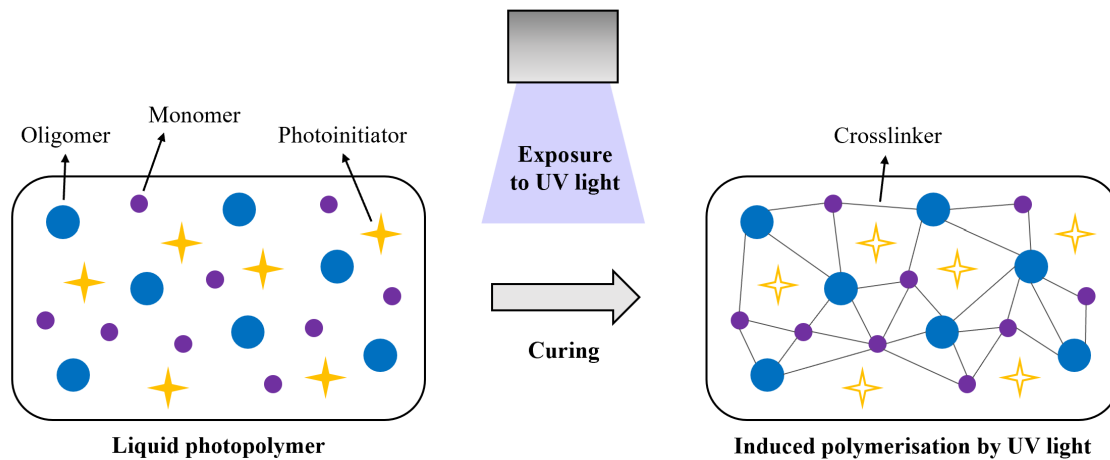
Figure 1.16: Scheme of the photopolymerisation process.

1.5.2   Replication of damage tolerance mechanisms of cortical bone

F. Libonati et al. [71] employed a PolyJet 3D printer to fabricate samples and explored their fracture behaviour through mechanical testing. Their primary focus was to integrate the toughening mechanisms found in cortical bone into new composite. To achieve this, they created simplified models by replicating some microstructural features, specifically the osteons (*i.e.*, only the Haversian structure), which were represented as cylinders embedded into a matrix. Given the printer resolution, they opted to maintain the same dimension for the osteon diameter but increased it by one order of magnitude.

Two key parameters were investigated: the geometry and the materials. The impact of the reinforcement geometry was examined by representing osteons as circular or elliptical inclusions (based on literature researches). In addition, the effect of the reinforcement-to-matrix stiffness ratio was explored by fabricating samples with both stiff reinforcement and soft matrix, as well as soft reinforcement and stiff matrix configurations. Notably, the latter strongly affected crack propagation and overall failure mode.

In the case of stiff inclusions and soft matrix, the effect of osteon geometry was more evident. Here, the compliant matrix allowed significant deformations that leaded to increased energy dissipation before fracture. This was facilitated by the formation of microvoids ahead of the crack tip, reducing stress concentration, and fibril bridging behind the crack tip, preventing crack propagation. Furthermore, the inclusions bore most of the load and guided crack paths along their boundaries, displaying a toothed crack pattern. Two key toughening mechanisms were observed: continuous crack branching for the elliptical pattern and continuous osteon-driven crack deviations for the circular one.

Conversely, in the case of soft inclusions and stiff matrix, the effect of osteon geometry on the failure mode was less apparent. The matrix bore most of the load and, being less deformable, surrounded the inclusions to prevent their initial deformation. Here, the primary toughening mechanisms were uncracked-ligament bridging within the matrix and fibril bridging within the soft inclusions. However, the overall mechanical properties were clearly influenced by the osteon geometry, with the elliptical pattern being the most successful. In fact, elliptical osteons are found in young and stronger bones.

In conclusion, the failure modes of the synthetic composites had similarities with the ones of cortical bone (corresponding to configurations with soft inclusions and stiff matrix), like crack branching and deflection, constrained microcracking and fibril bridging (Fig. 1.17). These findings thus validated the potential of the design to replicate bone fracture and toughening mechanisms.
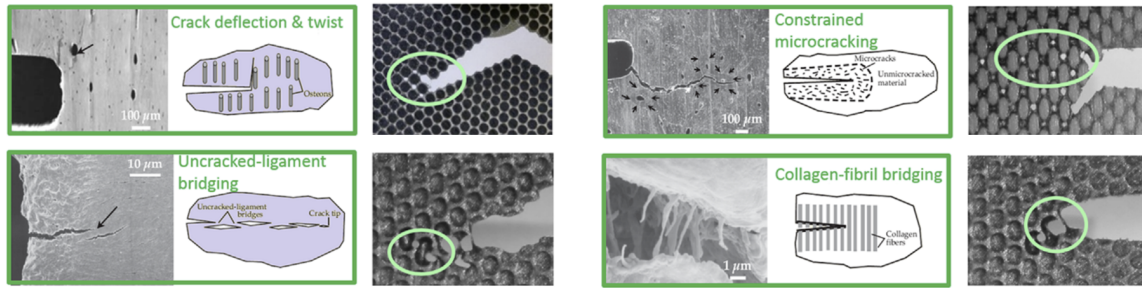
17

Figure 1.17: Primary toughening mechanisms observed in the bone-inspired composites (stiff material in black and soft material in grey) which are compared with those occurring in the microstructure of cortical bone [71].

1.5.3 Probing the role of bone lamellar patterns

The arrangement of collagen fibres in osteonal bone affects its mechanical properties, contributing to tissue anisotropy. Different fibre orientations are correlated to the main local loading, suggesting fibres align to bear specific loads. G. Grezzana et al. [72] investigated how different osteon morphotypes (OMs) relate to mechanical behaviour and why nature employs specific OMs in stress-dominated regions. They focused on the twisted osteon morphotype (TOM), resembling the twisted plywood with a continuous fibril rotation, prevalent in compressive-dominated areas and the vertical osteon morphotype (VOM) found in tensile-dominated areas.

Their methodology involved conducting mechanical tests on 3D-printed OM-inspired samples. In fact, the fibres were mimicked using a stiff material and the matrix was imitated with a soft material. The printing process used a PolyJet technology, ensuring a perfect material adhesion. While the chosen materials did not precisely replicate the stiffness ratio of mineralised collagen fibres and the matrix, they have been demonstrated to correctly replicate some mechanisms observed in several biological materials [73, 74, 75, 76].

Compression tests revealed that VOM had a higher stiffness than TOM. However, TOM behaved better under compression, showcasing greater strength and toughness (Fig. 1.18a). This was attributed to the presence of ring-like tilted fibres that restricted the radial deformation and delayed buckling, thereby enhancing overall performance. In contrast, VOM experienced collective buckling (Fig. 1.18b). The analysis of crack propagation mechanisms revealed distinct patterns (Figs. 1.18c–f). In VOM samples, the crack initiated at the Haversian canal and propagated by crossing lamellae, being deflected by fibrils. Conversely, in TOM samples, the crack developed between adjacent layers without reaching the Haversian canal. Lamellar orientation influenced crack growth, leading to delayed propagation and higher energy dissipation. In conclusion, these findings clearly demonstrated the stress-tailored nature of OMs, with VOM and TOM performing better under tension and compression, respectively.
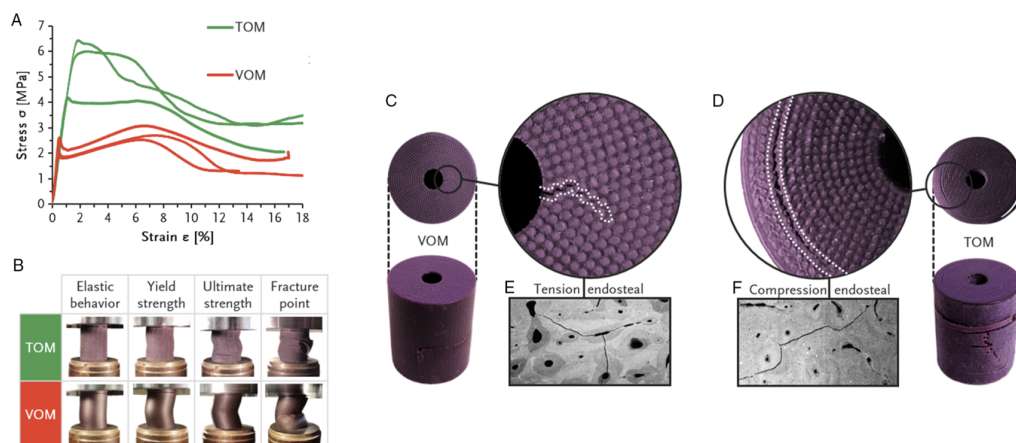

Figure 1.18: (A) Experimental stress-strain curves. (B) Deformation and failure mechanisms. (C–F) Comparison between crack propagation observed in the 3D-printed samples (VOM and TOM) and the crack patterns observed in bone endosteal regions subjected to tension and compression, respectively [72].

18

1.5.4 Controlling failure regimes in brick-and-mortar structures

G. Hunter et al. [77] investigated the influence of design parameters on the failure mechanisms of brick-and-mortar structures, which is essential for predicting and controlling their strength and toughness. These structures were composed of stiff rectangular bricks connected by a soft interface, with the number of bricks in each direction and brick aspect ratios selected based on previous studies (Fig. 1.19a). The samples were fabricated using a Polyjet 3D printer, using stiff VeroWhitePlus and soft TangoBlackPlus materials, and tested under uniaxial tension. Their goal was to predict new failure regimes and demonstrate that these regimes could be controlled by adjusting the brick aspect ratio.

Figs. 1.19b–c illustrate the stress-strain response for two different aspect ratios (AR 2.5 and AR 6.1), along with snapshots taken at high deformation stages. For both aspect ratios, initial damage and failure occurred within only a couple of adjacent rows of the normal layers (point A). Further failure events then differed between the two structures.

For the smaller aspect ratio (AR 2.5), the next failure event was the failure of the shear layers that connected the already failed normal layers (point B). This resulted in an uninterrupted line of failure through the structure, leading to its complete failure (point C). This behaviour was characterised as a 'two-peak' failure response.

For the larger aspect ratio (AR 6.1), the next failure event involved the progressive failure of the normal layers, which corresponds to the plateau region in the stress-strain response. Once all the normal layers had failed, the shear layers subsequently failed (point B), resulting in the complete failure of the structure (point C). This failure regime was denoted a 'peak-plateau-peak' failure response due to the shape of the stress-strain curve.

These two failure regimes highlighted the ability of the structure to distribute damage prior to failure, with the 'peak-plateau-peak' regime being more effective than the 'two-peak' failure response. Indeed, the toughness of the structure significantly increased as it transitioned from a 'two-peak' to a 'peak-plateau-peak' failure response, without compromising its strength and stiffness.

Moreover, literature has identified two distinct failure regimes for brick-and-mortar structures under this loading condition: failure through the layer and failure through the bricks. This study successfully demonstrated two additional failure regimes within the category of failure through the layers.
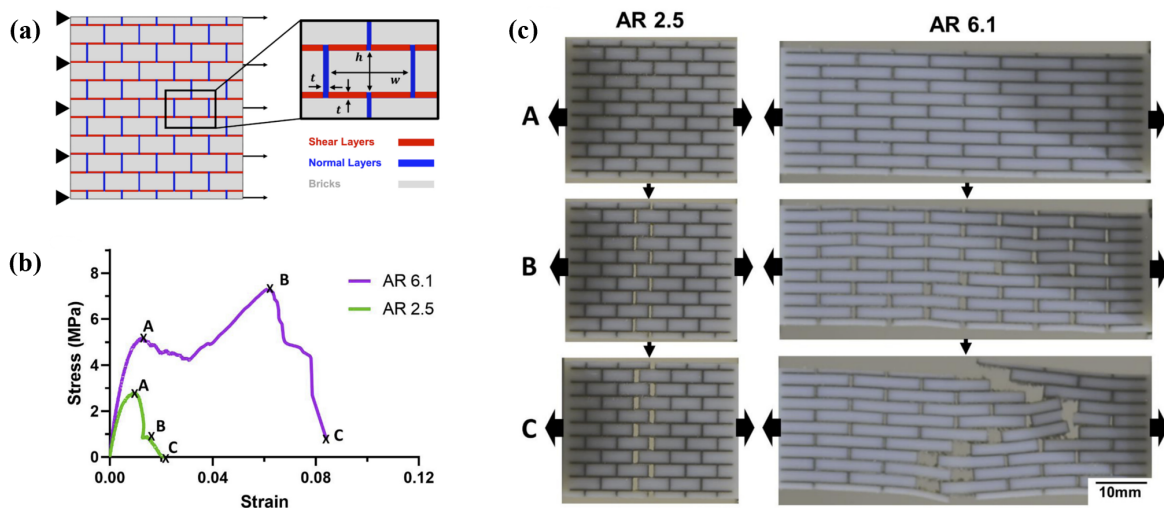

Figure 1.19: (a) Schematic representation of a brick-and-mortar structure. (b) Experimental stress-strain response of the structures with aspect ratio of 2.5 and 6.1, respectively. (c) Snapshots of the key failure sequence events [77].

1.6 Main aims of the master thesis

From literature, it can be observed that there is considerable interest to draw inspiration from the damage tolerance mechanisms present in biological materials. By replicating these principles, scientists and engineers can create bio-inspired designs with improved performances, notably toughness, suitable for various applications.

Our main goal is to assess how cracks interact with a weak region in presence of an interface depending on the model material properties. From the osteon architecture, we retrieve the concept of protecting a hole (representing the Haversian canal) from incoming cracks. The interface investigated is a porosity pattern, that we assume capable of deviating and trapping crack propagation. As previously explained, porosity is also spotted inside the osteonal structure with osteocytes located in the lacunae. Although this porosity has a heterogeneous distribution rather than a defined pattern, it could play a role in mitigating micro-crack propagation.

The objective of this master thesis is threefold:

1. From these assumptions, we design a simple rectangular model with a notch located on the right side and the addition or not of a half-hole located on the opposite side. Based on this geometry, we first conduct an extensive parametric study. The parameters explored include the model material properties, notch location and notch size. Their influences on the crack trajectory and the model toughness are assessed. For the material properties, two variables are considered: the fracture strain and the damage evolution energy. These two parameters define, respectively, the damage initiation and damage evolution phases in our ductile damage modelling approach, as proposed by [64].

2. Following this preliminary study, a set of parameters is selected to further explore the model, now including a porosity arrangement. Drawing inspiration from [6], we introduce a linear pattern of pores.

   - We start by examining a model with a planar pattern (*i.e.*, without any inclination) to be able to assess the toughness of the interface by varying the spacing between consecutive pores and testing different combinations of the two model material properties.

   - Next, based on the same parameters, this pattern is tilted at different angles to observe how the inclination affects the mechanical response of the model and the way cracks propagate.

   - Lastly, we add the half-hole to determine under which configurations the crack is either shielded or not, and with which proportion.

3. Finally, a selection of samples is 3D printed and tested in tension using the equipment available at the MBBM laboratory. These experimental tests serve as a proof-of-concept study to support and validate computational results.

Consequently, this thesis really adopts an integrative approach, combining computer simulations, multimaterial 3D printing and experimental testing to explore the mechanical efficiency of bio-inspired architectured materials. The outcomes should guide the development of flaw-tolerant materials with a fully programmable failure behaviour.

Chapter 2

Preliminary parameters study

The objective of this first chapter is to investigate all the parameters at our disposal in order to better understand their interplay within the simplest form of our geometries: a rectangle that may or may not include a half-hole inspired by the Haversian canal of the osteonal bone, and a notch to initiate a source of crack. The parameters studied include the material properties of the model, as well as the location and size of the notch. For the material properties, we focus on two main variables: the fracture strain and the damage evolution energy, as previously explained. This preliminary analysis thus uses finite element simulations to see how changes in these parameters affect crack propagation, in terms of progressive damage evolution and failure.

This chapter is structured into three main sections. Initially, the methodology is presented, outlining the development of finite element models. This includes the modelling approach, geometry definition, mesh generation, notch creation, material properties definition, boundary conditions set up, and specifications regarding the solver and output data. Then, the results obtained from the simulations carried out on the developed models are provided. Finally, these results are discussed in order to draw conclusions and highlight key insights learned from our investigation.

2.1 Methods

2.1.1 Modelling approach

The Finite Element Method (FEM) is a numerical technique used to find approximate solutions to complex partial differential equations by converting them into a set of algebraic equations through a process called spatial discretisation. To initiate this method, a mesh (or grid) is generated to approximate the structure geometry. This involves dividing the structure into discrete sub-units, known as finite elements, similar to assembling pieces in a "LEGO game". These elements usually have simple shapes like quadrilaterals or triangles in 2D and are interconnected at points called nodes. These nodes ensure that the field quantities (such as the displacement) remain continuous across adjacent elements, thereby sharing the same degrees of freedom (DOF) at connecting nodes. This continuity is achieved through piecewise polynomial interpolations over the mesh. In essence, FEM converts a continuum problem, which has an infinite number of DOF, into a discretised problem with a finite number of DOF represented by nodal values [78].

This section aims to introduce a phenomenological model called the "ductile damage plasticity model", already implemented in the finite element simulation software, ABAQUS [79, 80].

Ductile fracture happens when a material undergoes permanent plastic deformations, associated with the gradual accumulation of damage leading to crack propagation. In ABAQUS, the framework for modelling failure involves four main steps, as shown in Fig. 2.1: specifying the initial undamaged material response (curve a-b-c-d'), determining the criterion for damage initiation (point c), defining the rule for damage evolution (curve c-d), and providing an option for element removal when the material stiffness is completely degraded (point d).
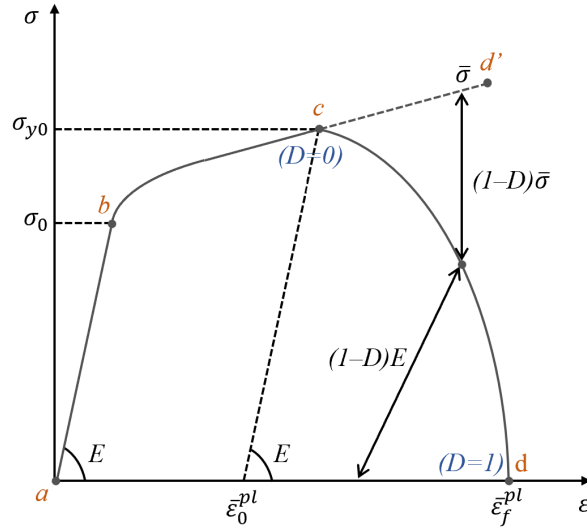
Figure 2.1: Uniaxial tensile stress-strain curve for a ductile material. Dashed curve (c-d') = undamaged response. Solid curve (c-d) = progressive damaged response.

Ductile damage initiation

Damage and fractures in ductile metals occur due to various microscopic deformation mechanisms. These include ductile fracture due to void nucleation, growth and coalescence, shear fracture caused by the development of micro-shear bands, and the initiation of micro-cracks. Each of these mechanisms requires different criteria to determine when damage begins. Our focus here is only on the ductile criterion.

This criterion assumes that the equivalent plastic strain at the onset of damage ($\bar{\varepsilon}_D^{pl}$) depends on the stress triaxiality (η) and the equivalent plastic strain rate ($\dot{\bar{\varepsilon}}^{pl}$). This relationship is expressed as $\bar{\varepsilon}_D^{pl}(\eta, \dot{\bar{\varepsilon}}^{pl})$, where $\eta = -p/q$ with p the pressure or hydrostatic stress and q the Von Mises equivalent stress.

The condition for damage initiation is met when the incremental increase in equivalent plastic strain satisfies the following condition. In other words, the model assumes that initiating damage requires reaching a critical equivalent plastic strain.

$$\omega_D = \int \frac{d\bar{\varepsilon}^{pl}}{\bar{\varepsilon}_D^{pl}(\eta, \dot{\bar{\varepsilon}}^{pl})} = 1 \tag{2.1}$$

For each increment, the value of ω_D will increase as

$$\Delta\omega_D = \frac{\Delta\bar{\varepsilon}^{pl}}{\bar{\varepsilon}_D^{pl}(\eta, \dot{\bar{\varepsilon}}^{pl})} \geq 0. \tag{2.2}$$

Ductile damage evolution

After reaching the damage initiation criterion (*i.e.*, when $\omega_D \geq 1$), the damage evolution law describes how the material stiffness and strength degrade over time. Initially, the overall damage (D) starts at 0 upon damage initiation and gradually increases to 1 as the material approaches complete failure. This increase in damage implies that both the elastic modulus (E) and the strength of the damaged elements goes to 0.

Consequently, the stress tensor of the material (σ) is determined by the following scalar damage equation

$$\sigma = (1 - D)\bar{\sigma}, \tag{2.3}$$

where $\bar{\sigma}$ is the effective (or undamaged) stress tensor that reflects the stress distribution in the material without damage. In other words, the stress in the element is reduced from its original undamaged value.

In addition, σ_{y0} and $\bar{\varepsilon}^{pl}$ represent the yield stress and the equivalent plastic strain at the onset of damage, while $\bar{\varepsilon}^{pl}_f$ is the equivalent plastic strain at total failure. The transition between these two points involves the dissipation of a specific damage evolution energy (G_f) in the element. The fracture energy is calculated as

$$G_f = \int_{\bar{\varepsilon}^{pl}_0}^{\bar{\varepsilon}^{pl}_f} L\sigma \, d\bar{\varepsilon}^{pl} = \int_0^{\bar{u}^{pl}_f} \sigma \, d\bar{u}^{pl}, \tag{2.4}$$

where L is the characteristic length of the element. This expression introduces the concept of equivalent plastic displacement ($\bar{u}^{pl}$). Before damage initiation, $\dot{u}^{pl} = 0$, while after damage initiation, $\dot{u}^{pl} = L\,\dot{\bar{\varepsilon}}^{pl}$.

Removing the element from the mesh

In ABAQUS, elements are removed from the mesh once they achieve maximum degradation (D_{max}) across all section points at any integration location. By default, if elements are deleted upon reaching this threshold, D_{max} is set to 1; otherwise, it is adjusted to 0.99. In fact, once D reaches D_{max}, there is no additional damage accumulation at the integration point and the material loses its load-bearing capacity.

2.1.2 Geometries

In this study, two types of geometry are considered. The first one, called the full model, is a rectangular model ($H = 54$ mm in height and $W = 37.5$ mm in width), which includes simply a notch (see Section 2.1.4 for details) (Fig. 2.2a). The second one, called the hole model, is similar but features an additional element: a half-circular hole ($r = 5.1$ mm in radius) inspired by the Haversian canal of the osteonal bone, creating a weak spot in the structure (Fig. 2.2b).

(a) Full model.   **(b)** Hole model.
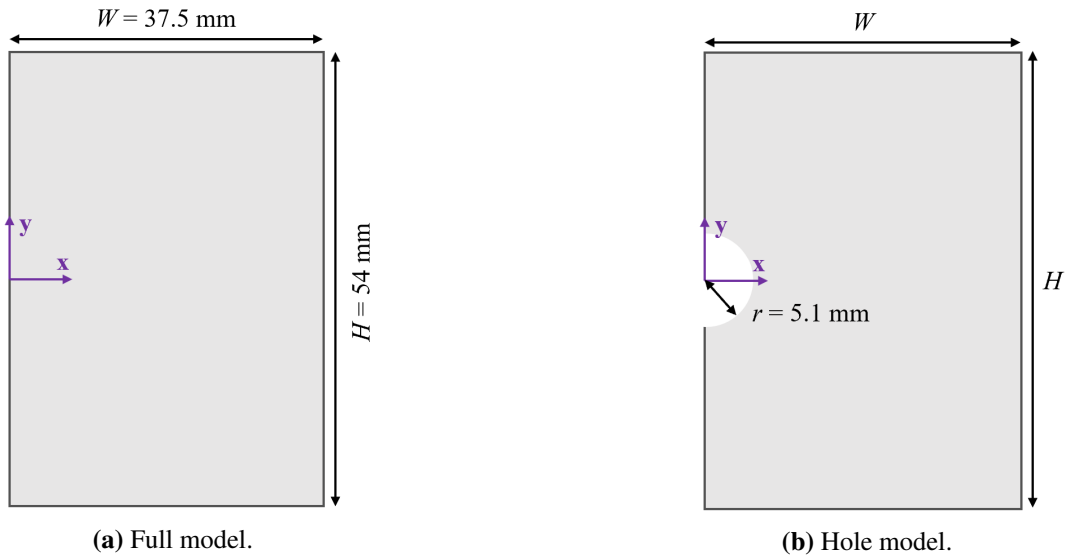
Figure 2.2: Schemes of the two different types of model geometry.

2.1.3 Meshing

Once the geometries are built, it is necessary to create meshes for the models. The meshing generation procedure is based on a MATLAB code and is illustrated in Fig. 2.3.

The mesh is made up of identical square elements, with a side length of 0.15 mm. This element type is referred to CPS4R in ABAQUS and represents four-node plane stress elements. The choice of both the element type and size was previously performed by T. Volders in his PhD framework. Indeed, the chosen element size is relatively small and similar to the one used by [64], and this kind of element gives a good compromise between response accuracy and simulation time.

To create the geometry in ABAQUS, two crucial components are required: a node list and an element list, which are intrinsically linked. The node list comprises the node number and its corresponding x- and y-coordinates, while the element list contains the element number and the numbers of the four nodes forming the element. Two important features are considered in the generation script: the nodes of an element are always defined along the same anti-clockwise sequence and same defined nodes are re-used in multiple interconnected elements.

The integration of the half-circular hole relies on a specific condition. This condition is defined using node coordinates and the formula for computing the radius of a circle: $r = \sqrt{(x+0.075)^2 + (y+0.075)^2}$. Elements are created if their centre point lies beyond the circle radius ($r \geq 5.1$ mm), while they are omitted if their centre point falls within this radius ($r < 5.1$ mm).
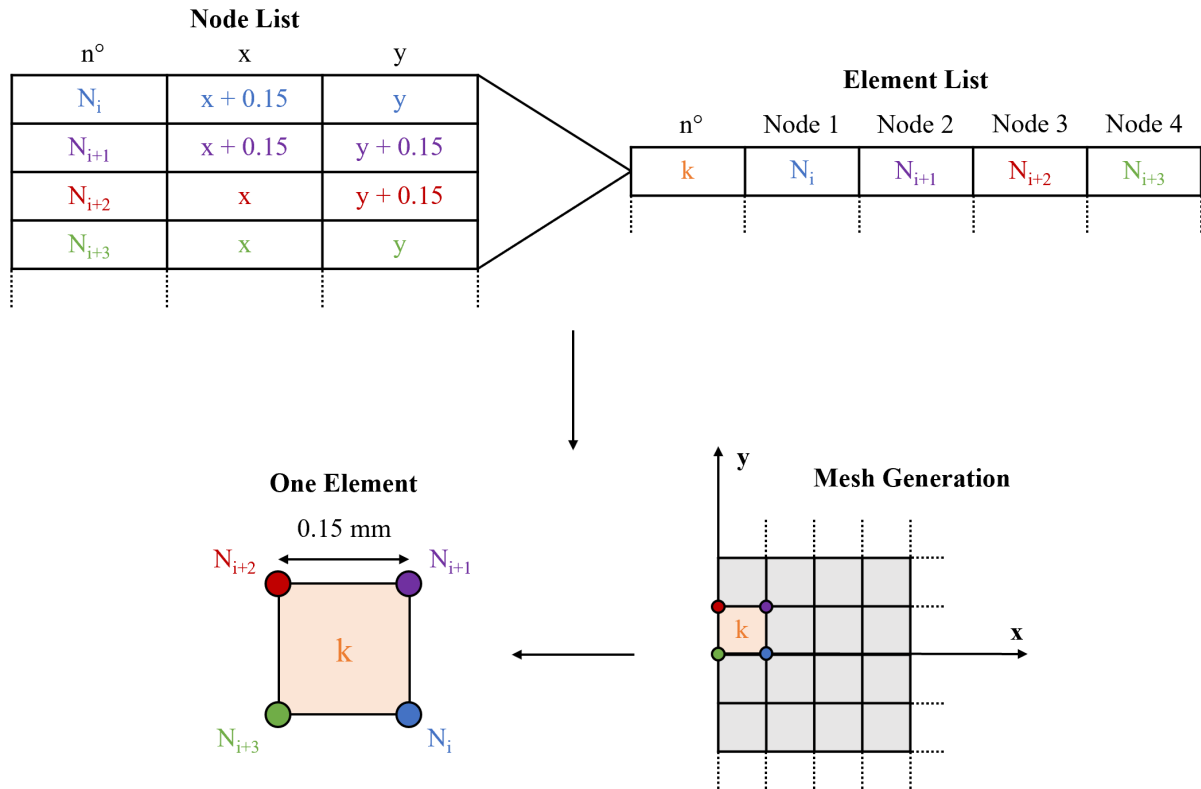
Figure 2.3: Mesh generation principle.

2.1.4 Initial notch creation

From a geometric point of view, the last step involves the creation of the notch. Two different methods exist to achieve this, such as removing elements, but we opt to disconnect elements from each other. In fact, the method involves duplicating the nodes shared by the elements we want to disconnect. These nodes are located in a specific interval of x-coordinates, defining the notch length, and at a particular y-coordinate, which represents the vertical position of the notch. The only exception is at the crack tip, where only one node requires duplication while the other remains unchanged (Fig. 2.4).

Two parameters thus need to be defined here. Firstly, the initial crack length is always fixed at the beginning to determine the x-coordinate of the node where the crack starts (*i.e.*, how far the elements need to be disconnected). This initial crack length (a/W) varies from 1.8 to 18.75 mm (*i.e.*, 5 to 50% of the model width). Secondly, the notch vertical position must also be determined. To test its influence, pre-existing cracks are first positioned one element above the midpoint of the right boundary. Then, in the case of the hole model, we search the critical y-position of the notch, at which the crack is no longer attracted by the hole.
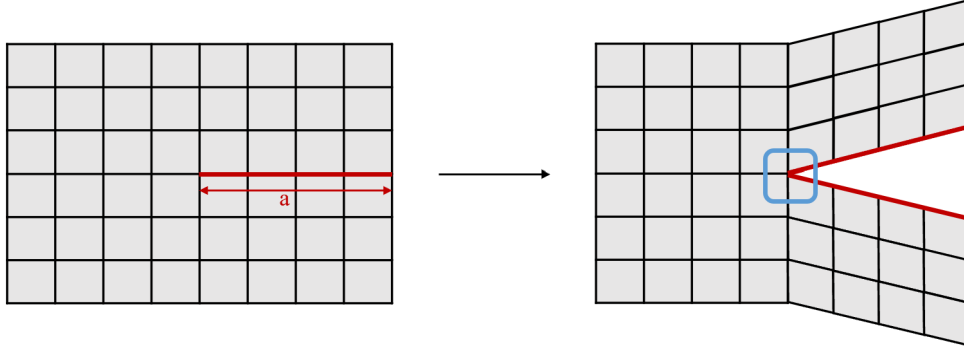
Figure 2.4: Zoom on the notch position (in red, notch length and in blue, notch tip).

2.1.5 Material properties

After the construction of the mesh, material properties need to be assigned to the model. These properties will remain consistent across all elements of the model.

Our base material is the Grey60, a PolyJet ink used in the 3D printer at the MBBM laboratory. In this study, we simplify its elastic and plastic properties, which were measured experimentally. The material has a relatively high Young's modulus of 1500 MPa, a yield stress of 30 MPa and a yield strain of 0.02. In addition, we account for a 3% stress hardening and a significant strain hardening between the yield point and the onset of damage, with a plastic strain (ε_f^{pl}) of 0.1 (Table 2.1).

	Grey60 ink	**Units**
Young's modulus (E)	1500	MPa
Yield stress (σ_y)	30	MPa
Yield strain (ε_y)	0.02	-
Fracture stress (σ_f)	30.9	MPa
Fracture strain (ε_f)	0.12	-
Plastic fracture strain (ε_f^{pl})	0.1	-

Table 2.1: Elastic and plastic material properties (for Grey60 ink).

Next, we need to determine the parameters for the ductile damage plasticity model (*i.e.*, fracture strain and damage evolution energy). In fact, damage initiation requires a plastic strain (ε_{DI}) and consumes a specific amount of plastic strain energy per unit volume (ω_{DI}). Then, damage evolution requires a strain (ε_{DE}) and depletes a fracture energy per unit volume (ω_{DE}). Consequently, the total dissipated energy per unit volume is $\omega_{FR} = \omega_{DI} + \omega_{DE}$ [64].

Fig. 2.5 shows the stress-strain behaviour of a ductile material undergoing damage. As can be seen, there exists an interplay between these two energies, which are computed as specific areas under the stress-strain curve.

$$\omega_{DI} \approx \sigma_y \varepsilon_{DI} + \frac{1}{2} \Delta\sigma \varepsilon_{DI} \quad \Rightarrow \quad \omega_{DI} \approx \left(\sigma_y + \frac{1}{2} \Delta\sigma \right) \varepsilon_{DI} \quad \text{with} \quad \varepsilon_{DI} = \varepsilon_f^{pl} = \varepsilon_f - \varepsilon_y \tag{2.5}$$

$$\omega_{DE} \approx \frac{1}{2} \sigma_y \varepsilon_{DE} \quad \text{with} \quad \varepsilon_{DE} = \frac{u_f}{u_i} = \frac{u_f}{0.15} = \frac{2G_f}{0.15\,\sigma_f} \quad \Rightarrow \quad \omega_{DE} \approx \frac{\sigma_y\,G_f}{0.15\,\sigma_f} \tag{2.6}$$

where $u_i = 1$ mm is the initial displacement, u_f is the displacement at fracture and G_f is the damage evolution energy.
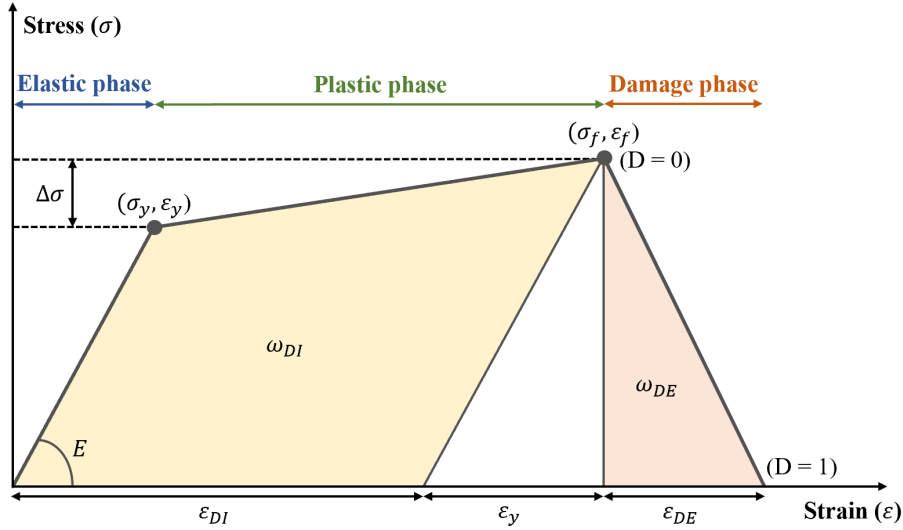
Figure 2.5: Schematic stress-strain curve of a ductile material subjected to damage, applied to our current study.

To investigate the impact of the damage evolution energy (G_f), three main values are initially studied: 0.01, 0.1 and 1 mJ/mm^2. These values describe materials that range from inherently more brittle to inherently more ductile. As will be demonstrated later, the intermediate value is only considered at the beginning of the analysis, but the focus quickly shifts to the two other values. Fracture strain (ε_f) is first treated as a variable, ranging from 0.03 (a value very close to the yield strain of Grey60) to 0.12 (its experimentally measured fracture strain).

Fig. 2.6 provides the values of ω_{DI} and ω_{DE} for different fracture strains. Notably, for varying damage evolution energy values, ω_{DI} remains consistent, while ω_{DE} undergoes significant changes. Two opposite trends can be observed. For $G_f = 0.01$ mJ/mm^2, indicative of a more brittle material, increasing the fracture strain results in a bigger difference between ω_{DI} and ω_{DE}. Conversely, for $G_f = 1$ mJ/mm^2, corresponding to a more ductile material, increasing the fracture strain leads to a smaller difference between ω_{DI} and ω_{DE}.

(a) $G_f = 0.01$ mJ/mm^2.

(b) $G_f = 1$ mJ/mm^2.
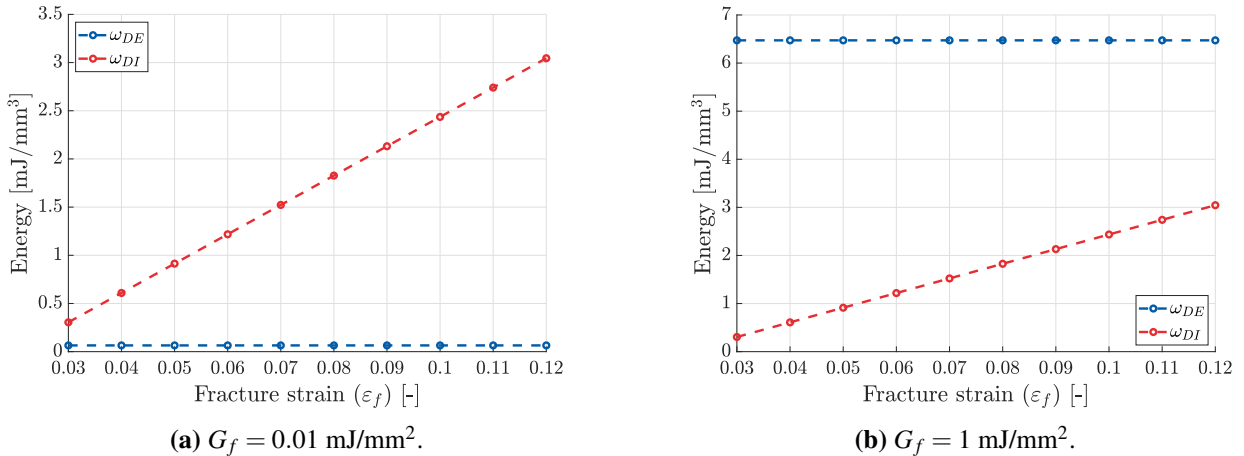
Figure 2.6: Plastic strain energy (ω_{DI}) and fracture energy (ω_{DE}) as a function of the fracture strain (ε_f) for two different values of damage evolution energy (G_f).

Based on these results, we gain a better understanding of the relationship between the two energies as a function of the model damage parameters. Finally, two fracture strain values are selected: $\varepsilon_f = 0.03$ (significantly reducing the strain hardening) and $\varepsilon_f = 0.12$, along with two damage evolution energy values ($G_f = 0.01$ mJ/mm^2 and $G_f = 1$ mJ/mm^2). As a result, there are four possible combinations in total. This range allows us to explore a variety of material behaviours, from brittle to ductile. Fig. 2.7 represents the nominal stress-strain curves for the defined material across the different combinations of ε_f and G_f, facilitating a visual understanding of the energy proportions.

(a) $\varepsilon_f = 0.03$.

(b) $\varepsilon_f = 0.12$.
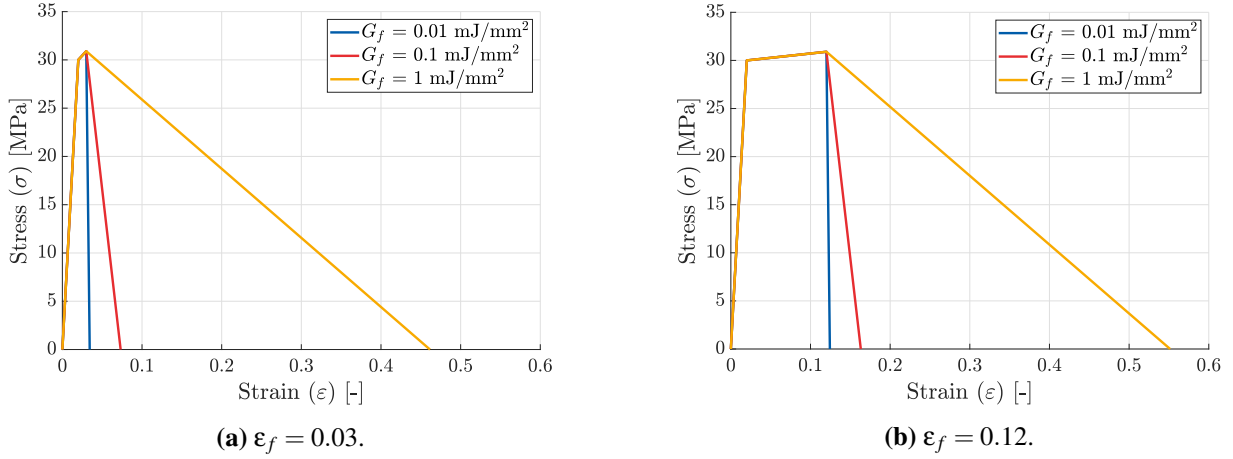
Figure 2.7: Nominal stress-strain curves of a ductile material for two different fracture strain values (ε_f).

Moreover, the elastic and plastic material properties presented in Table 2.1 are derived from previous experiments. Consequently, these nominal data need to be converted into true values for ABAQUS inputs. Appendix A provides a detailed description of the conversion process. Finally, Poisson's ratio ($\nu = 0.3$) and density ($\rho = 1.18 \times 10^{-9}$ t/mm^3) are considered globally constant across all models.

2.1.6 Boundary conditions

When creating a finite element model, one critical step is to define the boundary conditions. In this study, identical boundary conditions are applied to both geometries.

Since we focus on a 2D model, it is essential to impose the plane stress condition to ensure that stresses only occur within the $x - y$ plane. In practice, the normal stress (σ_z) and the shear stresses (τ_{xz}, τ_{yz}) directed perpendicular to the $x - y$ plane are assumed to be zero. This means that any displacements along the z-axis or rotations around the x- and y-axes are allowed. In addition, to prevent any singularities arising from rigid body motion, the model has to be fixed at certain points. Indeed, the bottom boundary nodes are blocked in both the x- and y-directions (equal to an embedding), while the top boundary nodes are restricted only in the x-direction. Lastly, a uniform prescribed displacement of $u_y = 1$ mm/s is applied to the top boundary nodes.

As a consequence, the model is fully constrained (Fig. 2.8). This choice is made bearing in mind that we wanted to reproduce the experimental test conditions in order to ensure consistency and enable comparison between computational and experimental results.
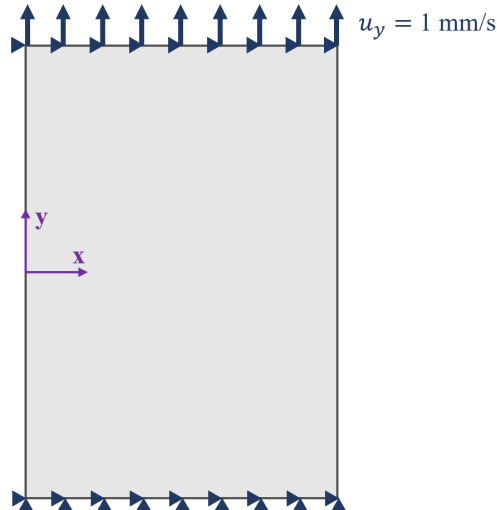

Figure 2.8: Illustration of the boundary conditions (example for the full model).

2.1.7 Solver features

The FE models described above are created using MATLAB scripts, which generate input files (`.inp`). Table 2.2 provides the number of nodes and elements contained in each meshed geometry. These models are then processed using ABAQUS software on a computer of the MBBM laboratory. This computer is equipped with an AMD Ryzen Threadripper PRO 5955WX processor with a base speed of 4.00 GHz, 16 cores and 32 GB of installed RAM. The resulting output files (`.odb`) are finally obtained, with sizes ranging from 2 to 9.5 GB.

	Number of nodes	Number of elements
Full model	90 611	90 000
Hole model	88 825	88 180

Table 2.2: Total number of nodes and elements for the different meshed geometries.

For all simulations, a dynamic explicit step is employed with a time period of 1 second and a maximum of 1000 intervals. Furthermore, the `Nlgeom` setting in ABAQUS is activated to account for geometric non-linearities resulting from large displacements and deformations under loading conditions.

Typically, one simulation requires an average CPU time of 3 hours, depending mainly on the initial notch length, the fracture strain and the damage evolution energy. This duration is considerable due to the high resolution of the model. In total, 110 simulations were conducted for this first part of the thesis. However, it is important to note that these CPU times do not include the time needed for the software to read and compute the mesh elements and to extract the results, which is more or less around 5 minutes per simulation.

2.1.8 Outputs exportation

From the simulation results (located in `.odb` files), both qualitative and quantitative analyses can be conducted using visualisation tools provided by ABAQUS and MATLAB. This process involves extracting two distinct types of output.

Initially, our attention is directed towards node-related outputs. Specifically, translations (UT) and reaction forces (RF and RT) at the upper nodes are acquired. To refine the node outputs and mitigate numerical instability, a second order Butterworth filter with a cut-off frequency of 150 Hz is applied (during the simulations).

Then, outputs related to the elements are obtained. This includes the Von Mises stress, maximum and minimum principal stress components (S), as well as nominal and logarithmic strain components (NE and LE). In addition, interest is placed on damage initiation criteria (DMICRT), especially the ductile damage initiation criterion (DUCTCRT), and on damage evolution, particularly the overall scalar stiffness degradation (SDEG). Finally, the status of each element (1 if active, 0 if inactive) is also extracted (STATUS).

Finally, MATLAB codes have been developed to process the above output data, both in the creation of customised images of crack and damage propagation and in the generation of graphs. Specifically, in these images, regions experiencing damage initiation (0 < DUCTCRT < 1), damage evolution (SDEG < 1) and cracking (SDEG = 1) are represented in blue, green and red, respectively. Global reaction force (normalised by the width) vs. displacement curves are also generated. These graphs enable the computation of peak forces which can be plotted against the initial crack length (a/W).

2.2 Results

This section presents the results of the extensive parametric study on the two distinct models. First, a qualitative analysis of the fracture patterns is presented. Then, we provide insights into how the two types of model respond to variations in notch length as a function of the fracture strain (ε_f) and damage initiation energy (G_f), while maintaining a constant notch vertical position near half of the model height. Afterwards, a second part studies the influence of the notch vertical position in the model featuring a half-circular hole, regarding the interplay between the notch and the weak spot. One objective is to identify the critical notch vertical position so that the crack is no longer attracted by the hole, regarding different model material properties configurations.

2.2.1 Fracture patterns analysis

Fig. 2.9 illustrates the different fracture patterns for the two types of model. Notably, as the notch is located near the middle side of the model, it is evident that the crack will propagate through the model centre.

For the most brittle type of material ($\varepsilon_f = 0.03$ and $G_f = 0.01$ mJ/mm^2), the images display minimal blue areas and a distinct red line indicating that a crack propagates. In contrast, for a high fracture strain ($\varepsilon_f = 0.12$), regardless of the G_f value, a large blue zone indicating damage initiation and significant plastic deformation can be observed. Lastly, when the material is brittle ($\varepsilon_f = 0.03$) but requires a lot of energy to break completely ($G_f = 1$ mJ/mm^2), green areas appear which means that elements quickly reach the degradation phase but do not have time to break completely because of the high damage evolution energy value.

Furthermore, when a half-circular hole is present, the blue and green zones tend to spread and fit to the shape of the hole as they approach it.
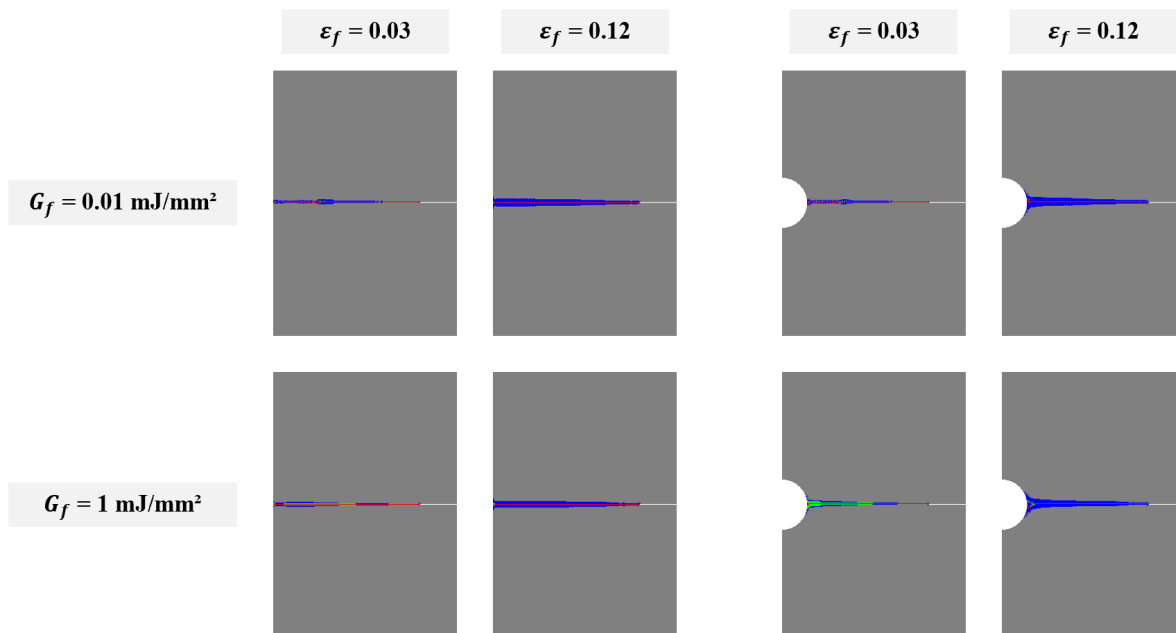
Figure 2.9: Comparison of fracture patterns between the full and hole models for two values of fracture strain (ε_f), two values of damage evolution energy (G_f) and an initial crack length corresponding to 20% of the model width, positioned at 0.15 mm. Grey areas correspond to intact elements (DUCTCRT = 0), blue areas to damage initiation (0 < DUCTCRT < 1), green areas to damage evolution (SDEG > 0) and red areas to the crack path (SDEG = 1).

2.2.2 Fracture modelling parameters analysis

The aim of these two subsections is to study the parameters of the ductile damage plasticity modelling approach: firstly the influence of the damage evolution energy (G_f) and secondly the influence of the fracture strain (ε_f).

Damage evolution energy influence

First, a model with a large fracture strain ($\varepsilon_f = 0.12$, from our initial Grey60 material) is examined. Three values of damage evolution energy ($G_f = 0.01$, 0.1 and 1 mJ/mm^2) are tested across varying notch lengths (5%, 10%, 20%, 30%, 40% and 50% of the model width).

The peak force vs. crack length curves (Fig. 2.10) follow an expected pattern: the peak force decreases as the initial crack length increases. However, despite varying the damage evolution energy values by two orders of magnitude, minor differences are observed between curves. This observation suggests that the damage evolution energy has a limited impact due to the high plasticity of the material. This finding is not straightforward because increasing the damage evolution energy should make the material more resistant to damage. Moreover, the curves for $G_f = 0.01$ and 0.1 mJ/mm^2 are surprisingly exactly the same. This can be partially explained by the nominal stress-strain curves shown in Fig. 2.7b, where increasing G_f from 0.01 to 0.1 mJ/mm^2 slightly increases the strain at complete failure of the material (from $\varepsilon_{tot} = 0.124$ to 0.163), resulting in a similar fracture energy. In contrast, increasing G_f from 0.01 to 1 mJ/mm^2 increases much more ε_{tot} from 0.124 to 0.552.

To get a better idea of what is happening to the mechanical response of the model, reaction force vs. displacement curves are plotted for each notch length, separating cases with and without the hole and focusing on the extreme values of damage evolution energy ($G_f = 0.01$ and 1 mJ/mm^2) (Fig. 2.11). For the full model, when G_f increases from 0.01 to 1 mJ/mm^2, the curves indicate a slight increase in peak forces (by 6.4%, 8%, 9.2%, 9.6%, 9.7% and 9.7% for increasing notch lengths, respectively) and in the displacement required to fracture the models (by 6.7%, 8.4%, 9.4%, 10%, 10.2% and 10.3%, respectively). These variations remain roughly constant in the hole model. In addition, the results show that introducing a larger notch decreases the stiffness of the model and the total energy dissipated during failure, as expected.

Compared to the full model, for both G_f, introducing a hole increases the displacement required to fracture the models (by 6.4%, 4.7%, 3.2%, 2.4%, 1.5% and 1.2% for increasing notch lengths, respectively) but decreases the peak forces (by 0%, 0.7%, 1.9%, 3%, 3.8% and 4.8%, respectively). This suggests that the hole does not have much influence and thus this reduced cross-section does not significantly weaken the structure (Fig. 2.12). In addition, the minor reduction in the curve slope (*i.e.*, stiffness, modulus of elasticity or Young's modulus) due to the hole does not lead to substantial changes in the overall strength of the system. One possible explanation is that the crack propagates straight directly towards the hole, similar to the behaviour in the full model (Fig. 2.9), suggesting that the hole influence is minimal for this notch vertical position.
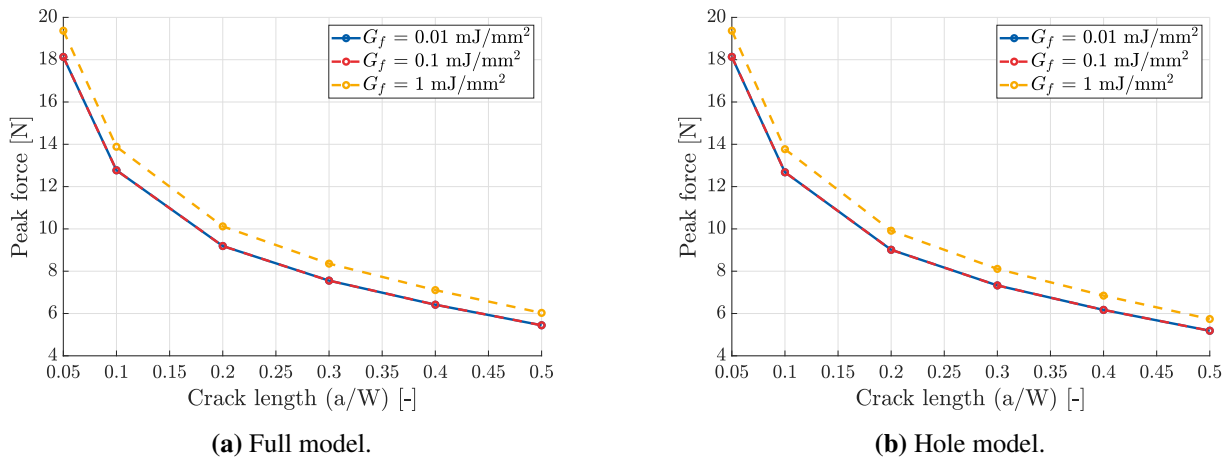

(a) Full model. **(b)** Hole model.

Figure 2.10: Peak force vs. initial crack length (a/W) curves for three different values of damage evolution energy (G_f), with a constant fracture strain of $\varepsilon_f = 0.12$, across two different models.
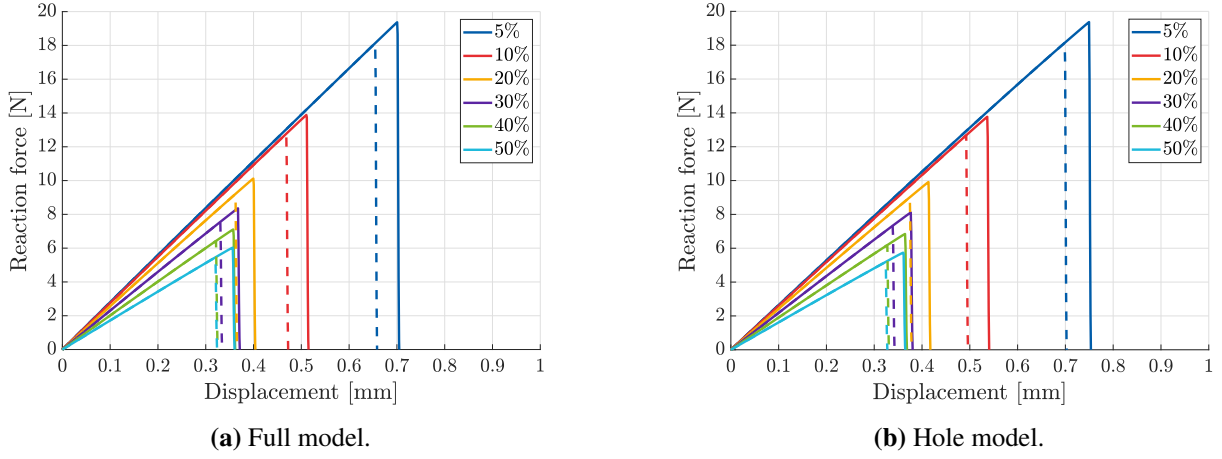
30

(a) Full model.

(b) Hole model.

Figure 2.11: Investigation of the damage evolution energy influence across two different models using $G_f = 0.01$ mJ/mm^2 (- -) and $G_f = 1$ mJ/mm^2 (-). Reaction force vs. displacement curves for six different initial crack length values, with a constant fracture strain of $\varepsilon_f = 0.12$.
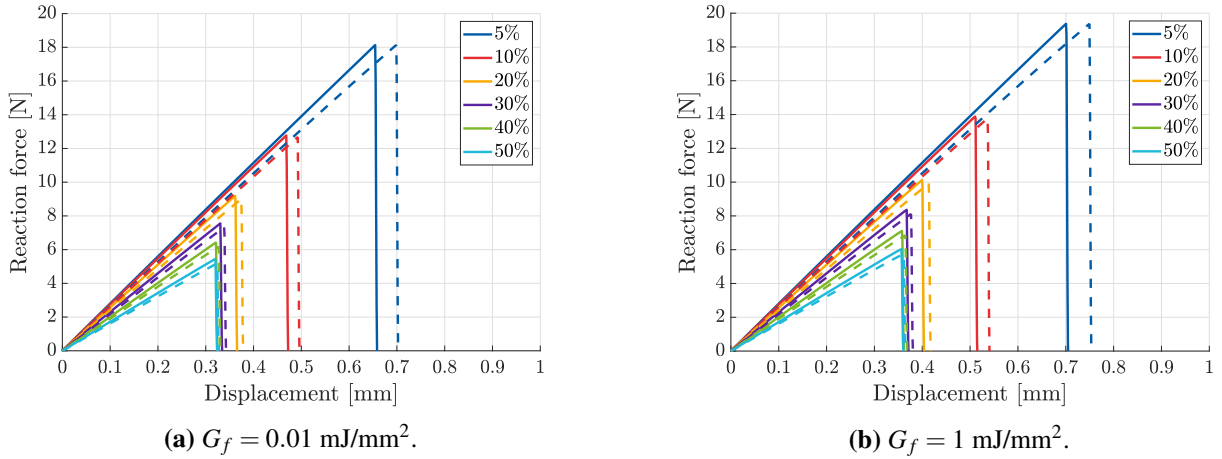

(a) $G_f = 0.01$ mJ/mm^2.

(b) $G_f = 1$ mJ/mm^2.

Figure 2.12: Investigation of the hole influence using both the hole model (- -) and the full model (-). Reaction force vs. displacement curves for six different initial crack length values and two values of damage evolution energy (G_f), with a constant fracture strain of $\varepsilon_f = 0.12$.

Fracture strain influence

The second set of simulation aims to explore the effect of a reduced fracture strain ($\varepsilon_f = 0.03$), keeping the same stress hardening. The objective is to better understand the interplay between damage initiation and damage evolution, still considering both model geometries. To maintain consistency with the previous section, the same notch lengths as well as two values of damage evolution energy ($G_f = 0.01$ and 1 mJ/mm^2) are considered.

As observed in Figs. 2.13 and 2.14, a reduced fracture strain seems to create more pronounced differences in peak forces between the two G_f values. For the full model, when G_f increases from 0.01 to 1 mJ/mm^2, the curves indicate a significant increase in peak forces (by 32.7%, 35.8%, 37.4%, 38%, 38% and 37.6% for increasing notch lengths, respectively) and in the displacement required to fracture the models (by 37.6% for a notch length of 20%). These variations remain again roughly constant in the hole model. Hence, these values are 4 times higher than the ones for $\varepsilon_f = 0.12$. As a result, the influence of the damage evolution energy becomes more significant for a smaller fracture strain value. However, the curves for a high fracture strain remains higher (*i.e.*, having larger forces and displacements at fracture) than the ones for a low fracture strain.

Moreover, the notch sensitivity defines how the peak force varies with different initial crack lengths (a/W). The percentage drop in peak force between the two extreme notch lengths (5% and 50%) remains relatively similar regardless of the combination of fracture strain and damage evolution energy. This suggests that the notch sensitivity is uniform across all combinations (Table 2.3).

In conclusion, G_f alone does not have much influence, but it is really the interplay between the energy in plastic deformation and energy in fracture.

In this case, introducing the half-hole still does not seem to significantly influence the results (Fig. 2.15). Indeed, the observations made in the previous subsection for a high fracture strain ($\varepsilon_f = 0.12$) are also true here for a smaller fracture strain value ($\varepsilon_f = 0.03$). Specifically, for $\varepsilon_f = 0.03$ and both G_f values, introducing a hole increases the displacement required to fracture the models by 3.4% but decreases the peak force by 2% for a notch length of 20%. These values are quite similar to those observed for $\varepsilon_f = 0.12$.

| | **Full model** | | **Hole model** | |
	$G_f = 0.01$ mJ/mm^2	$G_f = 1$ mJ/mm^2	$G_f = 0.01$ mJ/mm^2	$G_f = 1$ mJ/mm^2
$\varepsilon_f = 0.03$	70.37%	68.06%	72.05%	68.72%
$\varepsilon_f = 0.12$	69.97%	68.87%	71.41%	70.38%

Table 2.3: Percentage drop in peak force between the two extreme notch lengths (5% and 50%) for both fracture strain values (ε_f) and damage evolution energy values (G_f).

(a) Full model.

(b) Hole model.
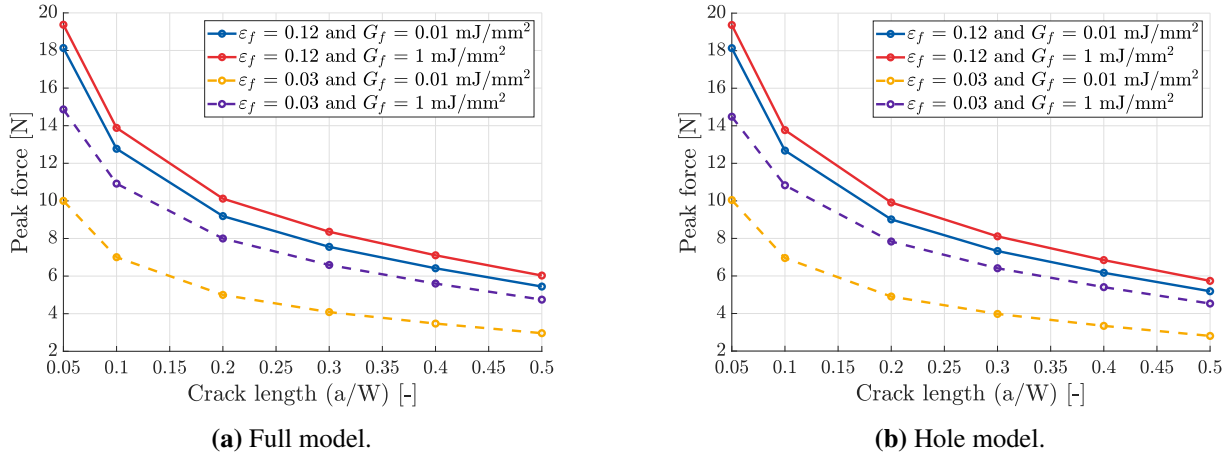
Figure 2.13: Comparison between two fracture strain values ($\varepsilon_f = 0.03$ and 0.12). Peak force vs. initial crack length (a/W) curves for two different values of damage evolution energy (G_f), across two different models.

(a) Full model.

(b) Hole model.

Figure 2.14: Comparison between two fracture strain values ($\varepsilon_f = 0.03$ and 0.12) and investigation of the damage evolution energy influence across two different models using $G_f = 0.01$ mJ/mm^2 (- -) and $G_f = 1$ mJ/mm^2 (-). Reaction force vs. displacement curves for an initial crack length corresponding to 20% of the model width.
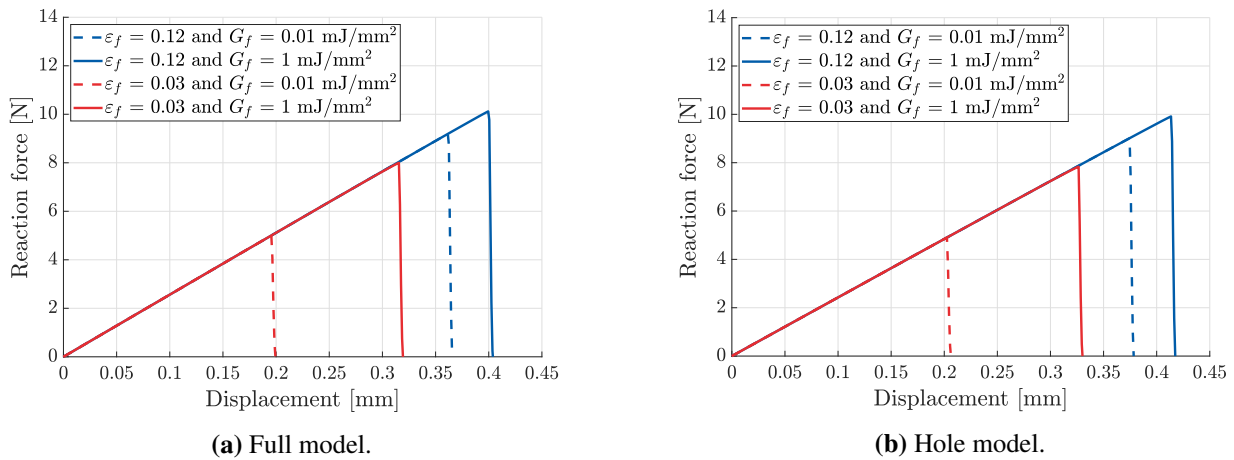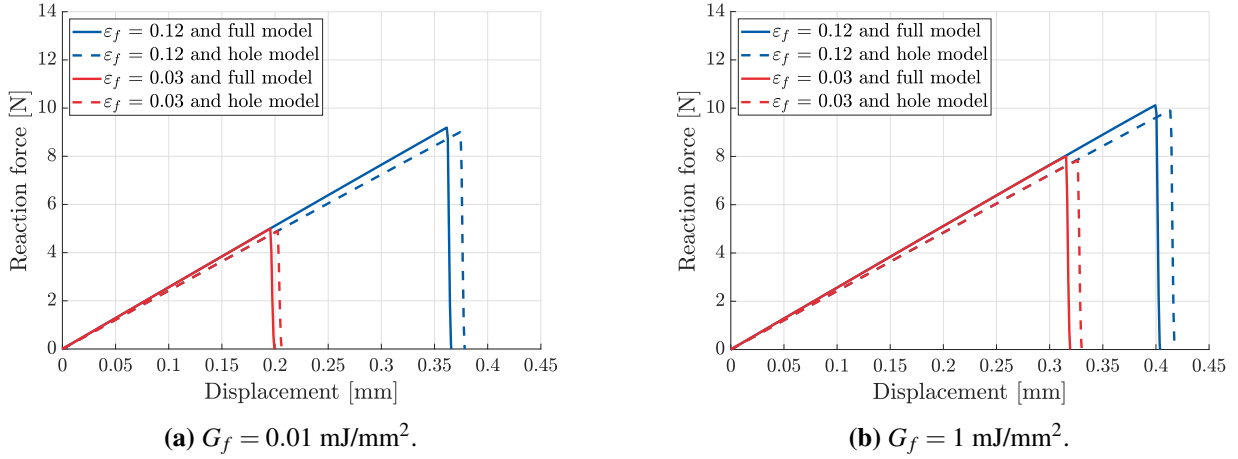
(a) $G_f = 0.01$ mJ/mm^2.

(b) $G_f = 1$ mJ/mm^2.

Figure 2.15: Comparison between two fracture strain values ($\varepsilon_f = 0.03$ and 0.12) and investigation of the hole influence using both the hole model (- -) and the full model (-). Reaction force vs. displacement curves for an initial crack length corresponding to 20% of the model width and two values of damage evolution energy (G_f).

2.2.3 Interplay between the weak spot and the notch parameters

For only the model including a half-hole, the aim is now to evaluate the interaction between this weak spot, and the initial length and vertical position of the notch.

Interplay weak spot - notch length

In this second approach, the notch is moved up vertically to 6.3 mm above the model middle side. This specific position was previously identified by T. Volders, in his PhD framework, as the critical notch position for the crack to feel the hole if present. On the basis of this new challenging position, we want to re-evaluate how the crack now propagates with respect to the combinations of fracture strain and damage evolution energy precedently studied. Those include: two values for fracture strain ($\varepsilon_f = 0.03$ and 0.12) and damage evolution energy ($G_f = 0.01$ and 1 mJ/mm^2). However, we only consider the model configuration with a hole.

As can be seen in Fig 2.16, moving the notch position up has minimal impact on peak forces, regardless of fracture strain values. Nevertheless, what is more interesting here are the fracture patterns produced by the crack propagation (Figs. 2.17 and 2.18). These crack paths vary greatly depending on the combination of parameters.

For a small fracture strain, the crack does not appear to be attracted to the hole for a small damage evolution energy, but does so for a larger energy (Fig. 2.17). In fact, this behaviour can be understood by considering the proportion between the plastic strain energy (ω_{DI}) and fracture energy (ω_{DE}) (Fig. 2.7). With $G_f = 0.01$ mJ/mm^2, both energies are similar and notably small, indicating high brittleness and minimal energy dissipation. In contrast, with $G_f = 1$ mJ/mm^2, the material can dissipate much more energy during fracture, meaning that the crack has more time to be attracted to the hole, which is not the case for a small G_f because the fracture is very brittle and so occurs very quickly. In addition, the crack deviation towards the hole seems to be more influenced by the reduction in the possible travel distance of the crack as the notch length increases and the material brittleness (because we do not see this phenomenon for $\varepsilon_f = 0.03$ and $G_f = 0.01$ mJ/mm^2). Therefore, the more the crack is attracted and deviated to the hole, the greater the influence of G_f.

For a large fracture strain, the crack seems to be attracted to the hole in all cases, except for a notch length of 20% and $G_f = 1$ mJ/mm^2 (Fig. 2.18). In fact, the increased fracture strain allows the material to dissipate much more energy during plastic deformation, as indicated by the larger damage initiation zone. This allows the crack to be attracted to the hole for both G_f values due to better damage redistribution in the model. We can also see that the larger the notch, and therefore the shorter the possible travel distance of the crack, the lower the capacity to create damage initiation (*i.e.*, lower amount of blue areas) that spreads along the fracture pattern.

Moreover, it is interesting to notice that for all parameter combinations, a 5% notch length creates quite different crack patterns, often leading to a catastrophic failure of the model. Here, the expression of the crack pattern nature is reinforced. For $\varepsilon_f = 0.03$ and $G_f = 0.01$ mJ/mm^2, we observe very brittle crack paths that spread throughout the model. For $\varepsilon_f = 0.03$ and $G_f = 1$ mJ/mm^2, a large green zone appears, indicating that many elements surpass the damage initiation phase but do not break due to the high G_f. For $\varepsilon_f = 0.12$ and $G_f = 0.01$ mJ/mm^2, we see a large blue area of damage-initiated elements with brittle crack paths. Lastly, for $\varepsilon_f = 0.12$ and $G_f = 1$ mJ/mm^2, a significant green zone is also present in addition to the large blue zone.

(a) $\varepsilon_f = 0.03$.

(b) $\varepsilon_f = 0.12$.
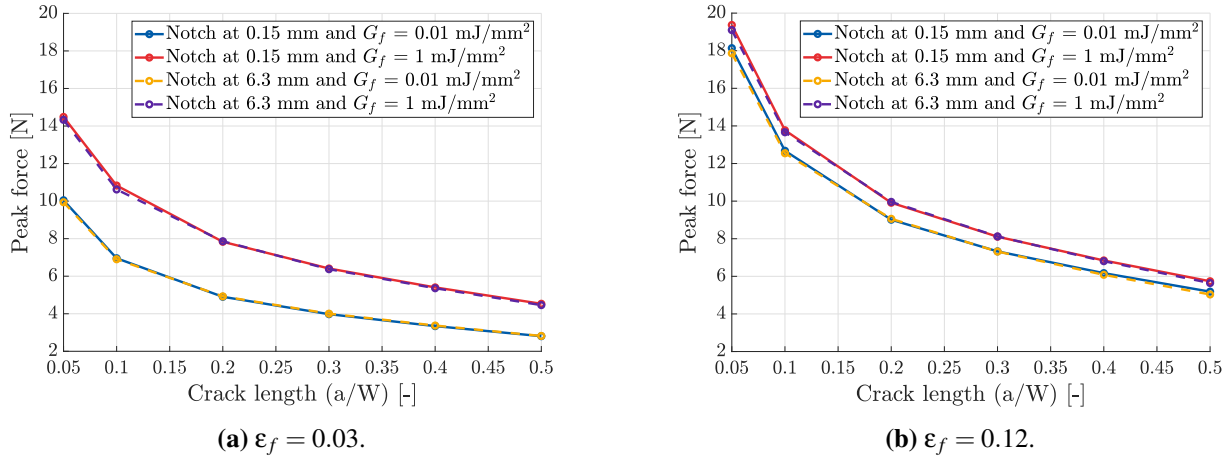
Figure 2.16: Comparison between two notch vertical positions (0.15 mm and 6.3 mm). Peak force vs. initial crack length (a/W) curves for two values of fracture strain (ε_f) and two values of damage evolution energy (G_f).
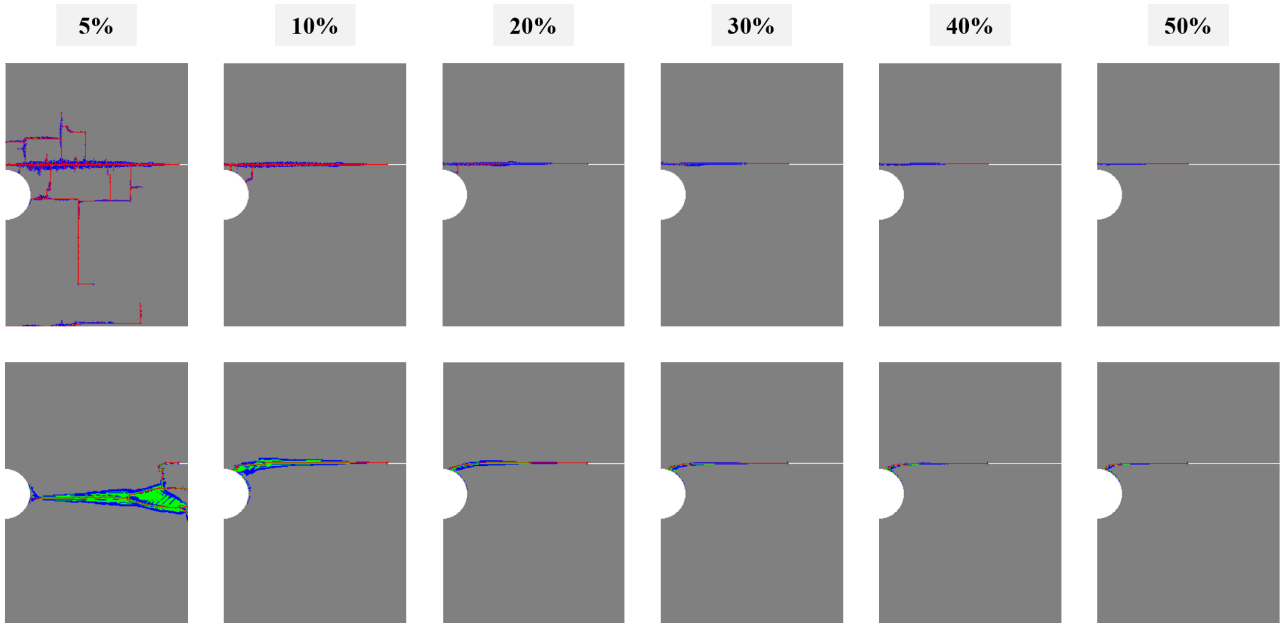
Figure 2.17: Fracture patterns of the hole model investigated for a fracture strain ($\varepsilon_f = 0.03$), two values of damage evolution energy (up: $G_f = 0.01$ mJ/mm^2, down: $G_f = 1$ mJ/mm^2) and an initial crack length corresponding to 20% or 50% of the model width, positioned at 6.3 mm. Grey areas correspond to intact elements (DUCTCRT = 0), blue areas to damage initiation (0 < DUCTCRT < 1), green areas to damage evolution (SDEG > 0) and red areas to the crack path (SDEG = 1).

Figure 2.18: Fracture patterns of the hole model investigated for a fracture strain ($\varepsilon_f = 0.12$), two values of damage evolution energy (up: $G_f = 0.01$ mJ/mm^2, down: $G_f = 1$ mJ/mm^2) and an initial crack length corresponding to 20% or 50% of the model width, positioned at 6.3 mm. Grey areas correspond to intact elements (DUCTCRT = 0), blue areas to damage initiation (0 < DUCTCRT < 1), green areas to damage evolution (SDEG > 0) and red areas to the crack path (SDEG = 1).

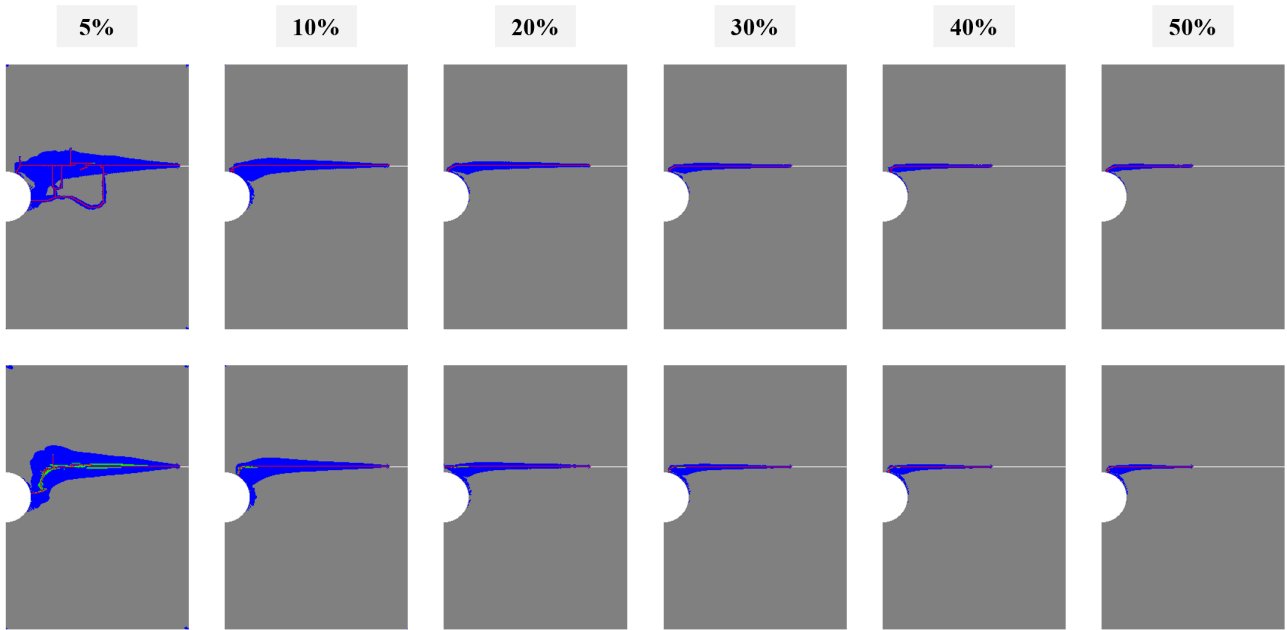**Interplay weak spot - notch vertical position**

For the final series of simulations performed in this first part of the thesis, our aim is to determine the critical vertical position of the notch at which the crack is no longer attracted by the hole. Two notch lengths have been selected for this study: 20% and 50% of the model width, also considering the same previous combinations of fracture strain (ε_f) and damage evolution energy (G_f).

The notch position indicated in Fig. 2.19 marks the occurrence of the crack not reaching the hole. These critical values certainly depend on the interplay between the damage evolution energy, the fracture strain and the notch length.

First, the notch length does not have much of an effect, because as the notch length more or less doubles, the critical vertical position changes by less than 5% (except for $\varepsilon_f = 0.03$ and $G_f = 1$ mJ/mm^2).

Furthermore, two opposite trends appear for the two fracture strain values. With $\varepsilon_f = 0.03$, as the damage evolution energy increases, the critical notch position can go higher for both notch lengths. With $\varepsilon_f = 0.12$, the behaviour seems to be switched. As the damage evolution energy increases, the critical notch position is lower for both notch lengths.

Finally, the strongest hole attraction occurs with the combination of $\varepsilon_f = 0.03$ and $G_f = 1$ mJ/mm^2. Even if the notch vertical position reaches 7.2 mm, the hole still attracts the crack. In this case, the material does not dissipate much energy during plastic deformation (small ε_f), but it needs a lot of energy to fracture (large G_f). Consequently, the damage evolution energy has a huge influence because there is the possibility that the crack deviates or curves a little more. However, it is important to remember that in practice, the goal is to shield this hole. Despite this case stands out from the rest, it is therefore the least likely to provide fast shielding when the notch is moved up.
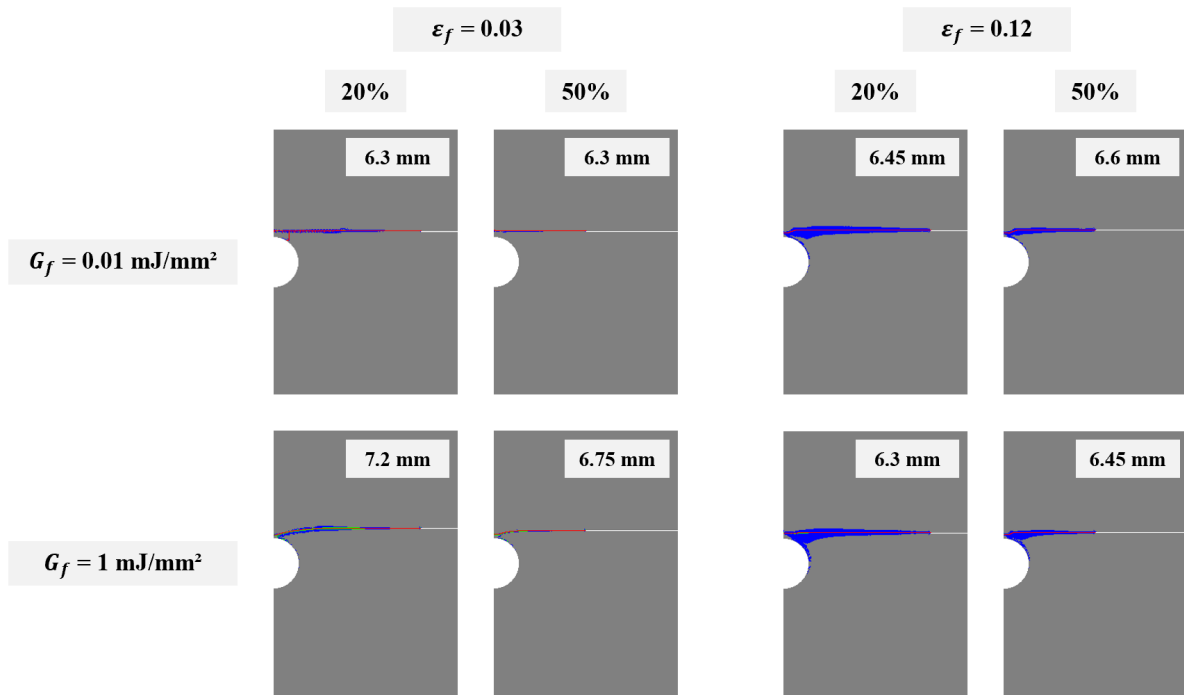
Figure 2.19: Fracture patterns of the hole model investigated for two values of fracture strain (ε_f), two values of damage evolution energy (G_f) and an initial crack length corresponding to 20% or 50% of the model width. The notch positions indicated in the models mark the first time that the crack does not reach the hole. Grey areas correspond to intact elements (DUCTCRT = 0), blue areas to damage initiation (0 < DUCTCRT < 1), green areas to damage evolution (SDEG > 0) and red areas to the crack path (SDEG = 1).

2.3   Discussion and conclusions

Simulations on simplified model geometries revealed several critical insights into the material behaviour under varying conditions of fracture strain, damage evolution energy, notch length and notch vertical position. The objective was to understand their individual and combined effects on the model fracture behaviour.

The results demonstrated a notable dependency of the peak force on the combination of fracture strain and damage evolution energy. Specifically, for a low fracture strain ($\varepsilon_f = 0.03$), increasing the damage evolution energy significantly raised the peak forces and the displacement required to fracture the models. This effect was 4 times less pronounced for higher fracture strains ($\varepsilon_f = 0.12$), indicating that the damage evolution energy had more substantial influence at lower fracture strain values. This observation aligns with expectations and external studies. H. Razi et al. suggested a difference of less than one-half between peak forces with a small fracture strain and a similar order of magnitude variation in damage evolution energy, although for different geometries [64]. Moreover, the difference in peak force variation between the two fracture strain values when G_f increases from 0.01 to 1 mJ/mm^2 might be because a high fracture strain allows the system to develop much more plasticity before failure, limiting the impact of the damage evolution energy.

Then, for both fracture strain values, the presence of a half-hole in the model increased the displacement required to fracture the model and slightly decreased the peak force. This indicates a minor influence of the hole on the overall model fracture behaviour for a notch vertical position near the middle of the model side.

After that, we moved the notch to an upper vertical position, that we knew it was on the verge of no longer attracting the crack to the hole for a combination of $\varepsilon_f = 0.12$ and $G_f = 0.01$ mJ/mm^2 (based on T. Volders's PhD framework). Verification through our simulations showed that this was true for an initial notch length of 20% of the model width but not for other notch lengths. Overall, the objective of shielding the hole was not achieved at this notch vertical position, as the crack was still attracted to the hole for three combinations of ε_f and G_f (except for the most brittle material). While moving the notch vertically significantly altered the crack paths, it had minimal impact on peak forces. This is because the distance the crack must travel remained nearly

the same for each initial notch length, regardless of the notch vertical position, requiring the same amount of energy for its propagation.

Our analysis then highlighted critical notch vertical positions for two specific notch lengths where the crack was no longer attracted to the hole. These positions varied depending on the interplay between ε_f, G_f and notch length. For instance, in the case of $\varepsilon_f = 0.03$ and $G_f = 1$ mJ/mm^2, a high critical position for both notch lengths were observed. However, the hole still had influence on the crack to a slight degree. One possible explanation for this behaviour is that the high damage evolution energy assigned to this initially brittle material during plastic deformation allows it to dissipate more energy during fracture. This suggests that G_f contributes more significantly over time acting on the crack path. Conversely, with a higher fracture strain, the material undergoes more plastic deformation, which reduces the effectiveness of a higher damage evolution energy.

Overall, these results collectively provided a comprehensive understanding of how different parameters affect the material behaviour under loading in highly simplified model geometries, especially in terms of crack propagation, damage evolution and fracture resistance. The key takeaway message is that both fracture strain and damage evolution energy play crucial roles, but their influence is highly dependent on their interplay rather than on absolute values.

Chapter 3

Porous interface study

This chapter is dedicated to study the addition of a weak interface (*i.e.*, a porosity pattern) in the previous models featuring the same material parameters space. To progressively understand the influence of this interface on crack propagation, three steps are considered. First, the interface is placed horizontally (at 0°) to evaluate its relative toughness regarding the bulk version model, depending on the pore spacing as well as the fracture modelling parameters. Then, the interface is tilted with respect to the horizontal axis and we study its influence on the model mechanical response as well as the fracture patterns, regarding the same parameters. Finally, we add our last level of complexity, the weak spot (*i.e.*, the half-hole), trying to answer our main research question about the interplay between the hole and the interface.

As before, the methods are outlined, focusing primarily on the geometry and meshing process definition. Following this, the results of these three approaches are presented and discussed.

3.1 Methods

3.1.1 Modelling approach

Our current numerical study continues to employ the ductile damage plasticity modelling approach, as discussed in Section 2.1.1.

3.1.2 Geometries

The basic models on which porosity is grafted are the same as those described in Chapter 2. To recap, the full model is a rectangle with dimensions of $H = 54$ mm (height) and $W = 37.5$ mm (width), including a pre-existing notch. The hole model is similar but includes an additional half-circular hole with a radius of $r = 5.1$ mm. The porosity pattern is then modelled as a straight line of pores, with a set of spacing distances (Fig. 3.1). This has been implemented using an extension of the previous MATLAB code with a linear mathematical function.

Figs. 3.1a–b are now described from right to left. For all simulations, we consistently use a notch length of 20% of the width (*i.e.*, 7.5 mm), positioned one element above the midpoint of the right boundary (*i.e.*, 0.15 mm). Then, we also maintain a distance of five elements between the notch tip and the first pore of the pattern. Finally, the line along which porosity is introduced is rotated at angles of 0°, 10°, 20°, 30° or 40°. In case of the hole model, due to the additional geometrical feature, only three of them are considered (20°, 30° or 40°) to avoid the pattern to directly make contact with it. Rotating the line at angles greater than 45° causes it to intersect the upper boundary of the model and so exit the model space. Each pore is represented by a square perforation, created by removing one element from the model. The spacing distance in between pores is computed as a number of elements in a range of one element to eleven elements. Indeed, we should bear in mind that if the pores are too far away, the crack cannot be guided effectively. Conversely, if they are too close, the crack will follow the pores but the material may become excessively weakened.
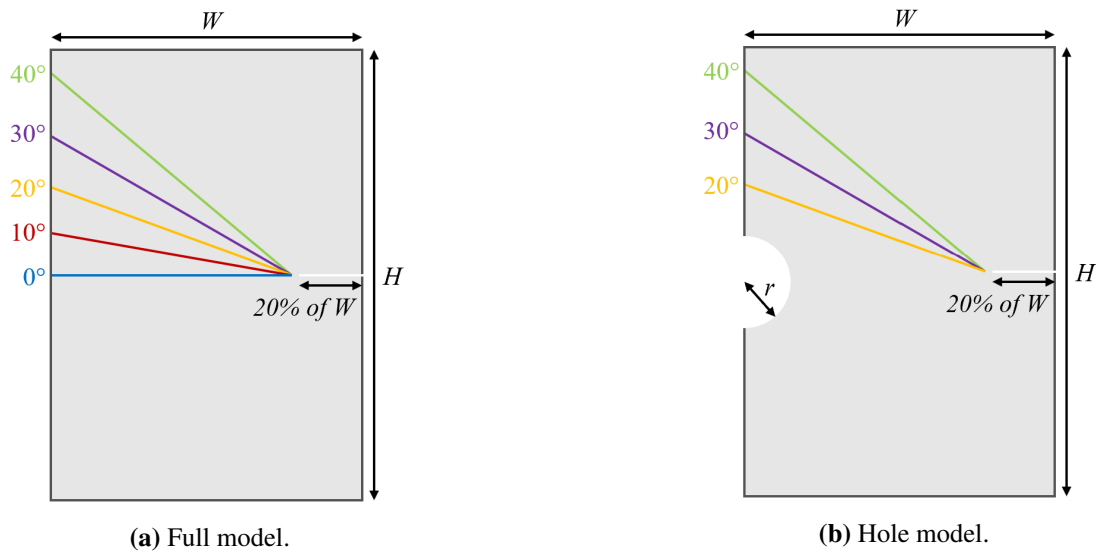
(a) Full model.

(b) Hole model.

Figure 3.1: Schemes of the two different types of model geometry. Porosity is arranged along a line rotated at angles of 0°, 10°, 20°, 30° or 40°.

Furthermore, a second approach for creating a porosity pattern involves using a smooth elliptical design. Although this method is not covered in this report, a brief explanation is provided in Appendix B.

3.1.3 Meshing

The same meshing procedure developed in Chapter 2 is used to create both models. As a reminder, this method aims to generate a mesh composed of identical square elements with a side length of 0.15 mm. This element type, referred to CPS4R in ABAQUS, represents four-node plane stress elements. The intermediate step involves creating sets of four nodes, with their corresponding *x*- and *y*-coordinates, that are associated with the elements. This enables to create a node list and an element list. In addition, the introduction of the half-circular hole in the hole model is achieved through a specific condition based on the circle radius.

Moreover, the porosity must now be included that makes the meshing process more intricate. Multiple steps are required to create the porosity pattern, as explained in Fig. 3.2.

First, a straight horizontal line is drawn using the *x*- and *y*-coordinates of the nodes. This line extends beyond the model limits and ends at the bottom right corner of the element corresponding to the first pore near the notch.

Next, this line needs to be rotated around the aforementioned corner. Since the centre of rotation is not at the origin, the line must first be translated so that the rotation point aligns with the origin of the Cartesian plane. This translation is applied to all the points of the line. Then, the line is rotated according to the rotation matrix, taking into account a clockwise rotation by using a negative angle (θ). Finally, the inverse translation is applied.

After rotation, the line must be shortened to fit within the rectangle defined by the model boundaries, the *y*-position of the notch and the *x*-coordinate of the bottom right corner of the element corresponding to the first pore near the notch. Simultaneously, the porosity coordinates are stored in a matrix, with an additional set of coordinates ensuring that the porosity pattern always starts at the same point.

Finally, a fixed distance between consecutive pores is defined and replicated along the line. This process starts from the notch and extends to the left side of the model, ensuring consistent placement of the first pore. In the end, the result is a matrix containing the *x*- and *y*-coordinates of the bottom right corner of the elements that need to be removed.
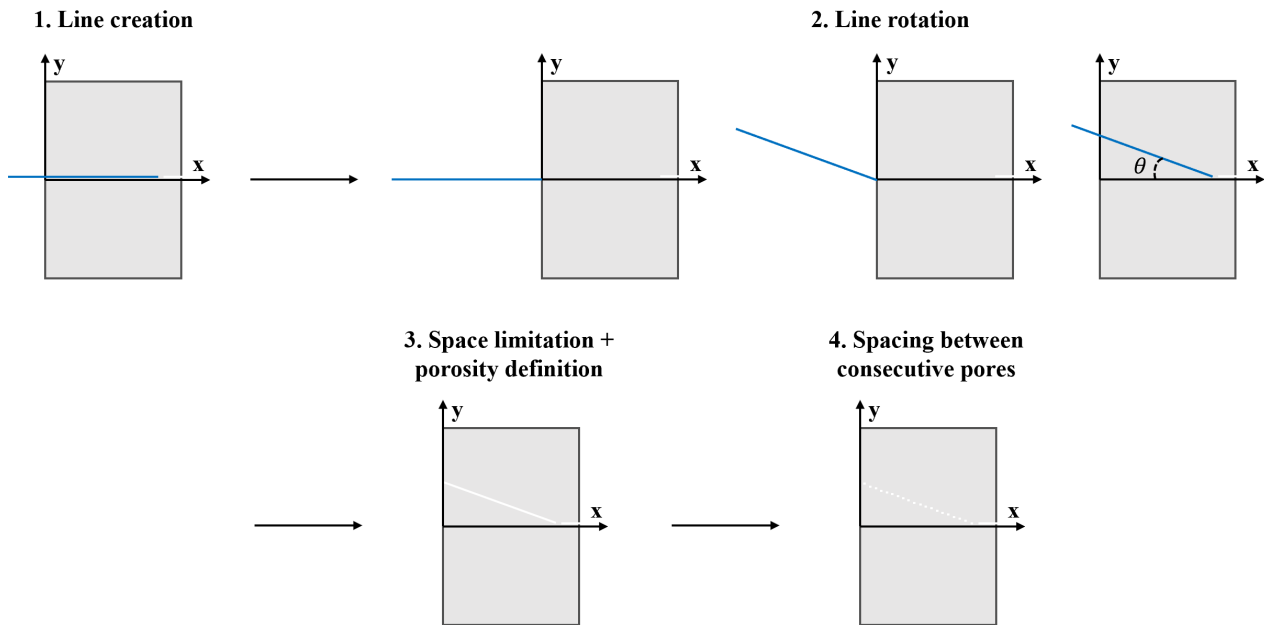
Figure 3.2: Porosity generation principle.

3.1.4 Material properties

The same material properties for the Grey60, detailed in Table 2.1, are used. Specifically, two values for the fracture modelling parameters are again considered for both the fracture strain ($\varepsilon_f = 0.03$ or 0.12) and the damage evolution energy ($G_f = 0.01$ or 1 mJ/mm^2). These parameter combinations allow us to simulate a very brittle, a very ductile and two intermediate types of material behaviour. Lastly, Poisson's ratio ($\nu = 0.3$) and density ($\rho = 1.18 \times 10^{-9}$ t/mm^3) are again considered globally constant in all the models.

3.1.5 Boundary conditions

The boundary conditions for this analysis are defined in the same manner as in our previous study. As a reminder, the plane stress condition is once again applied to the 2D models. The bottom boundary is completely fixed, preventing any movement, while the top boundary is constrained solely in the *x*-direction. Furthermore, a uniform prescribed displacement of $u_y = 1$ mm/s is applied to the top boundary nodes. This consistent setup ensures that our results remain comparable and any variations in the outcomes can be attributed to changes in material properties or other variables under investigation.

3.1.6 Solver features

The FE models are still created using MATLAB scripts, which generate input files (`.inp`). Tables 3.1 and 3.2 provide the number of elements and pores contained in each meshed geometry, considering an unchanged number of nodes compared to the models without porosity (90 611 for the full model and 88 825 for the hole model). These models are then processed once again using ABAQUS software on the same computer as in the previous chapter. This computer is equipped with an AMD Ryzen Threadripper PRO 5955WX processor with a base speed of 4.00 GHz, 16 cores and 32 GB of installed RAM. The resulting output files (`.odb`) are finally obtained, with sizes ranging from 2 to 4.5 GB.

For all simulations, a dynamic explicit step is employed with a time period of 1 second and a maximum of 1000 intervals. Furthermore, the `Nlgeom` setting in ABAQUS is activated to account for geometric non-linearities resulting from large displacements and deformations under loading conditions.

Typically, one simulation requires an average CPU time of 3 hours, depending mainly on the fracture strain and damage evolution energy values. In total, 112 simulations were conducted for the first approach and 38 for the second. However, it is important to note that these CPU times do not include the time needed for the software to read and compute the mesh elements and to extract the results, which is more or less around 5 minutes per simulation.

Pore spacing [mm]	Number of elements	Number of pores
0.15	89 902	98
0.30	89 935	65
0.45	89 951	49
0.60	89 961	39
0.75	89 967	33
0.90	89 972	28
1.05	89 975	25
1.20	89 978	22
1.35	89 980	20
1.50	89 982	18
1.65	89 983	17
Full model	90 000	0

Table 3.1: Total number of elements and inserted pores for each spacing between successive pores in the full model.

Pore spacing [mm]	Number of elements	Number of pores
0.15	88 099	81
0.30	88 126	54
0.45	88 139	41
0.60	88 147	33
Hole model	88 180	0

Table 3.2: Total number of elements and inserted pores for each spacing between successive pores in the hole model.

3.1.7   Outputs exportation

In this chapter, the same outputs as the previous study are extracted for visualisation purposes. The results are still presented in terms of crack and damage propagation. Specifically, regions experiencing damage initiation ($0 <$ DUCTCRT < 1), damage evolution (SDEG < 1) and cracking (SDEG $= 1$) are represented in blue, green and red, respectively. In addition, global reaction force (normalised by the width) versus displacement curves can also be generated once again.

3.2   Results

As a reminder, our objective is to reproduce the initial phase of the stepwise study conducted by F. Barthelat et al. [6] using our model configurations. Its motivation was to overcome the brittleness of glass by improving its toughness and its ability to deform. Instead of allowing a crack to propagate straight through the material, their goal was to channel the crack into a weak interface that would redirect it in a different direction. This weak interface was created using laser-engraved defects, where the fracture toughness of the interface can be tuned by varying the spacing between these defects. Afterwards, they fixed a defect spacing that did not reduce too much the toughness and investigated the influence of the interface inclination (θ).

With this context in mind, we first study the influence of the weak interface on crack propagation in the full model, considering the fracture modelling parameters and playing with two factors: the fracture toughness of the interface (given by the number of elements removed from our model) and the slope of the line along which the porosity is introduced (*i.e.*, the interface inclination). Subsequently, using the hole model, we investigate the interaction between the weak spot and this interface.

3.2.1 Interface toughness analysis

The fracture toughness of the interface ($K_I^{(i)}$) for the planar configuration (with a line of pores at 0°) and of the bulk material (*i.e.*, the full model without any pores) ($K_I^{(b)}$) can be calculated in two ways for each combination of fracture strain and damage evolution energy, and for different spacing between consecutive pores (ranging from one to eleven elements). The first method uses the formula: $K_I = \sqrt{\pi a}\, \sigma_c$, where fracture toughness depends on the notch length (a) and the critical stress (σ_c) at which the crack begins to propagate. In our case, the notch length is constant and the critical stress is given by the peak force normalised by the model width. Then, the energy absorption (*EA*) can also be computed as the area under the force-displacement curve until the peak load.

Looking at the shape of the reaction force vs. displacement curves (see Appendix C, Fig. A.5), we anticipate that these two methods for calculating fracture toughness will give similar trends. This expectation is based on the principle that higher peak forces should provide higher absorbed energies, while the Young's modulus only slightly varies. Fig. 3.3 validates this hypothesis. It depicts the ratio between the fracture toughness/energy absorption of the interface and that of the bulk material as a function of the pore spacing. Although the curves show respectively similar trends, the range of values differ by a factor of two.

Fig. 3.3a shows that in all the configurations, the relative fracture toughness increases with pore spacing until it reaches a plateau. In fact, the greater the spacing, the fewer pores in the interface, and therefore the greater the toughness of the interface (and vice versa).

The largest variation in fracture toughness occurs between pore spacing of one and two elements (*i.e.*, 0.15 to 0.3 mm), as well as between spacing of two and three elements (*i.e.*, 0.3 to 0.45 mm) when $\varepsilon_f = 0.12$ and $G_f = 1$ mJ/mm². Beyond them, larger spacing distances do not seem to significantly affect the interface toughness anymore and therefore, will not further be considered in our investigation.

When the pore spacing increases from 0.15 to 0.45 mm, the relative interface fracture toughness increases by 1.15% for $\varepsilon_f = 0.03$ and $G_f = 0.01$ mJ/mm², 2.01% for $\varepsilon_f = 0.03$ and $G_f = 1$ mJ/mm², 4.06% for $\varepsilon_f = 0.12$ and $G_f = 0.01$ mJ/mm², and 5.97% for $\varepsilon_f = 0.12$ and $G_f = 1$ mJ/mm². The pores are thus less felt in a very brittle material than in a more ductile material, since it has less impact on the fracture toughness. In fact, the behaviour of the most brittle material is close to that of its bulk model, as the plastic phase and energy dissipation during fracture are low. However, understanding the influence of the fracture strain itself is challenging. Increasing the fracture strain seems to induce greater variation in fracture toughness for low pore spacing values.

Consequently, the fracture toughness of the weak plane is influenced by the combination of the model material properties. Therefore, removing one element in each case is different. Quantitatively, the results show that introducing one pore between each element (*i.e.*, 98 pores in total) reduces the interface toughness by 3.4% ($\varepsilon_f = 0.03$ and $G_f = 0.01$ mJ/mm²), 7.3% ($\varepsilon_f = 0.03$ and $G_f = 1$ mJ/mm²), 6.7% ($\varepsilon_f = 0.12$ and $G_f = 0.01$ mJ/mm²) and 11.6% ($\varepsilon_f = 0.12$ and $G_f = 1$ mJ/mm²), compared to the bulk material. This suggests that, with the same pore spacing, the interface is more stronger/less weak for $G_f = 0.01$ mJ/mm² and more weaker for $G_f = 1$ mJ/mm², regarding additionally the entire curves evolution in Fig. 3.3. In addition, the interface appears slightly stronger for $\varepsilon_f = 0.03$ compared to $\varepsilon_f = 0.12$. In summary, increasing the ductility of the material and the energy required for its complete degradation tends to weaken the interface, making it easier to break and follow. This should be taken into account in the following analysis.
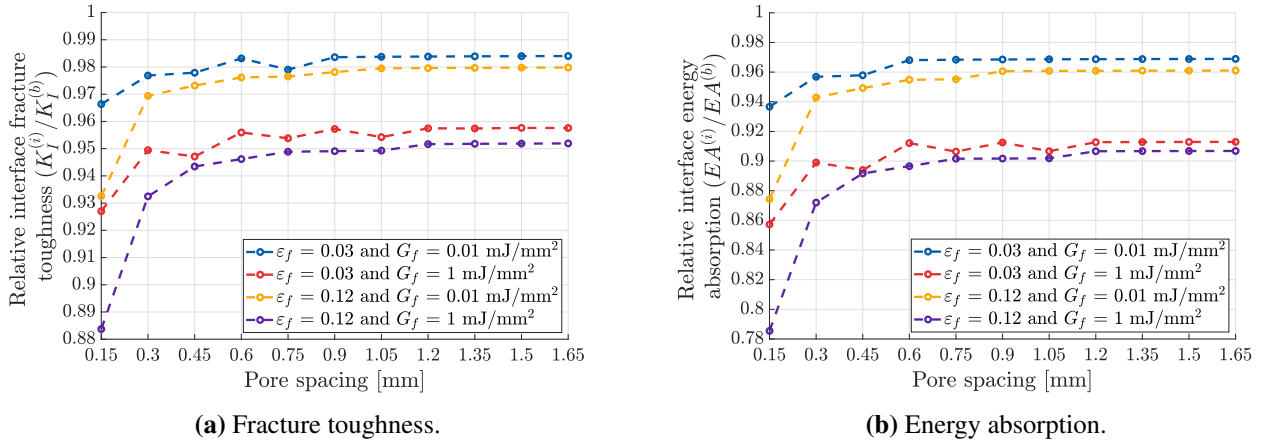
(a) Fracture toughness.

(b) Energy absorption.

Figure 3.3: Relative interface (a) fracture toughness or (b) energy absorption as a function of the pore spacing for each combination of fracture strain (ε_f) and damage evolution energy (G_f), and an interface inclined at 0°.

3.2.2 Impact of the interface inclination on its toughness

The next step is to tilt the pattern with respect to the horizontal axis to observe the interface angle influence on the relative model toughness as well the fracture propagation with respect to the pore spacing and fracture modelling parameters. The goal is to compare the relative fracture toughness of the interface with three different pore spacing and five different interface inclinations.

Fig. 3.4 presents various fracture patterns corresponding to different combinations of fracture modelling parameters and interface angles. Notably, three distinct modes of crack propagation when intersecting a weak interface at a certain angle are observed: complete crack trapping through the weak interface, partial trapping and unimpeded crack propagation straight into the material.

For the most brittle type of material ($\varepsilon_f = 0.03$ and $G_f = 0.01$ mJ/mm^2), the pictures show minimal blue areas and a distinct red line, indicating crack propagation (Figs. 3.4a–b). In this scenario, the crack is fully trapped in the pores only with a spacing of one element at either a 10° or 20° inclination. Increasing the pore spacing and, more significantly, the interface inclination (from 10° to 20°) appears to reduce the distance over which the crack follows the porosity pattern. Ultimately, for a spacing of three elements and a 20° inclination, the crack propagates almost through the centre of the model.

For brittle material with high damage evolution energy ($\varepsilon_f = 0.03$ and $G_f = 1$ mJ/mm^2), the crack remains completely trapped in the pores up to a pore spacing of two elements, even at a 30° inclination (Fig. 3.4c). Further increasing the pore spacing results in a huge drop in the proportion of the interface that the crack follows. In addition, green areas appear which indicates again that elements rapidly reach the degradation phase but do not completely break due to the high G_f value.

In contrast, for a high fracture strain but a low damage evolution energy ($\varepsilon_f = 0.12$ and $G_f = 0.01$ mJ/mm^2), a large blue zone indicating damage initiation and significant plastic deformation is observed under the crack path when fully trapped in the porosity pattern, and around it when the crack propagates straight, as seen in Fig. 2.9 (Fig. 3.4d). Therefore, when the crack is not deviated, the material retains its fracture behaviour as if no pores were added to the model. Increasing the damage evolution energy reduces the proportion of blue areas when the crack is deviated (Fig. 3.4e). Similar to the previous case, materials with $\varepsilon_f = 0.12$ exhibit a significant decrease in the extent of the interface that the crack follows once the pore spacing exceeds the limit that traps the crack.

These first observations suggest that increasing both the fracture strain and damage evolution energy facilitates crack guidance through the weak interface. These results are expected as this interface in these cases is more weaker and so more easier for the crack to follow.
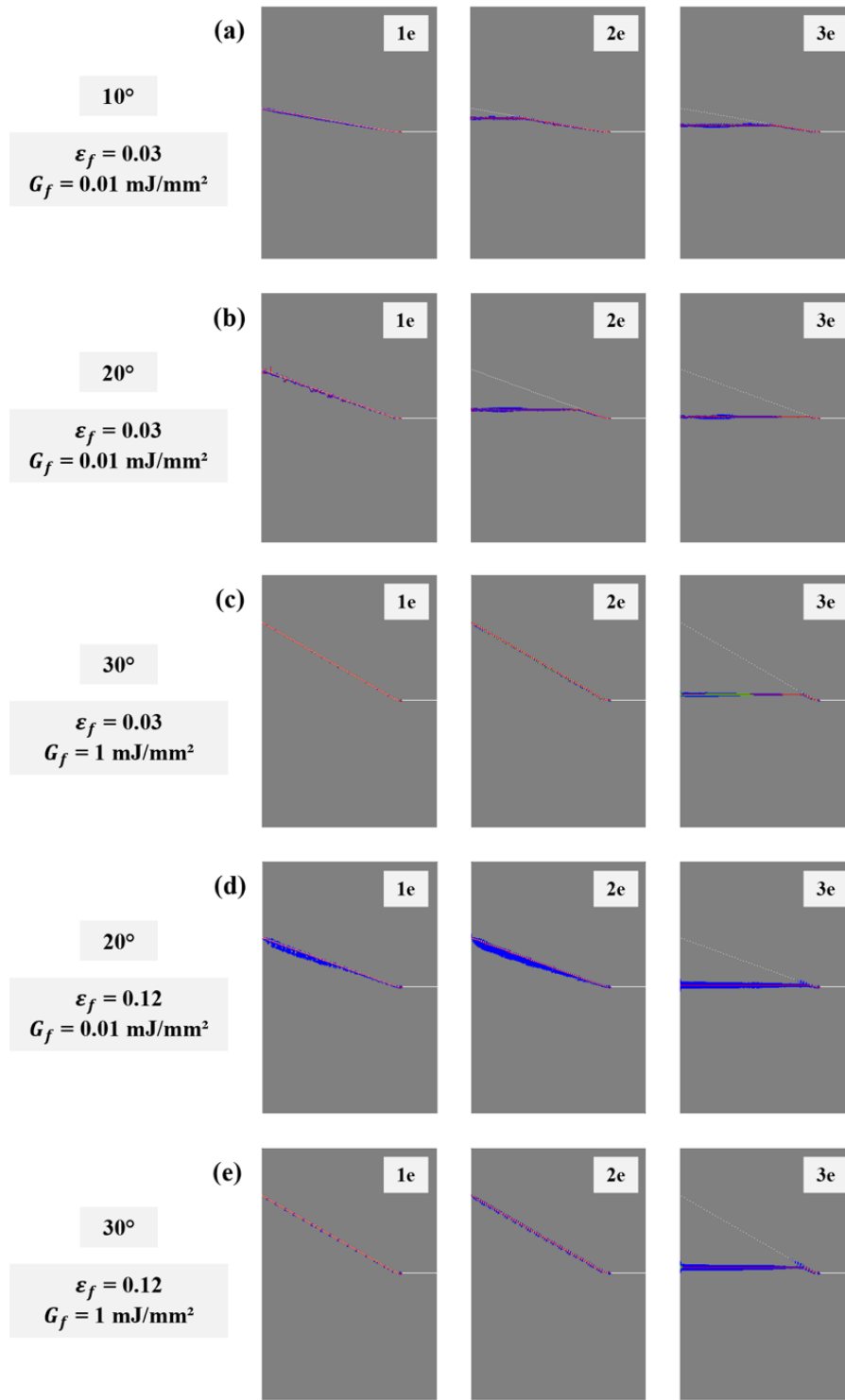
Figure 3.4: Fracture patterns of the full model investigated for two values of fracture strain (ε_f), two values of damage evolution energy (G_f), different weak interface inclinations, three pore spacing (one, two and three elements) and an initial crack length corresponding to 20% of the model width, positioned at 0.15 mm. Grey areas correspond to intact elements (DUCTCRT = 0), blue areas to damage initiation (0 < DUCTCRT < 1), green areas to damage evolution (SDEG > 0) and red areas to the crack path (SDEG = 1).

Fig. 3.5 displays the toughness ratio between the tilted interface and bulk material as a function of the interface tilt angle, for a given combination of fracture strain and damage evolution energy, and pore spacing. The graphs clearly demonstrate that the percentage increase in fracture toughness, previously computed for a porosity pattern inclined at 0°, as the pore spacing increases from 0.15 to 0.45 mm (*i.e.*, from one to three elements), is generally maintained for small inclinations (up to 20°) for each combination of material properties (gap between the blue and yellow curves).

Furthermore, the relative toughness varies with the interface inclination. In the most brittle case (Fig. 3.5a), the inclination has very little influence on toughness for each pore spacing ($\pm$ 0.3% in variation). In contrast, for the other cases (Figs. 3.5b–d), the inclination seems to more influence the toughness for pores spaced by one element, with a marked increase in toughness from 20° to 40° ($\pm$ 2–3% in variation). However, the inclination has less impact on toughness for pores spaced by two or three elements in these cases (max 1% in variation).

In a second time, the three modes of crack propagation observed in Fig. 3.4 are expressed here using symbols: ◯ where the crack is completely trapped, ◇ where the crack is partially trapped, and □ where the crack is not trapped and propagates straight into the material. This enables us to gain a complete overview of when crack deviation may occur or not. Globally, the results suggest that effective crack trapping can be achieved if the pore spacing and interface angle are not too large. However, with significant increases in inclination or pore spacing, the pore pattern loses its ability to fully guide the crack.

Specifically, simulations reveal that for a pore spacing of one element, the crack can be fully trapped in the weak interface for all inclinations in the most ductile material, and only partially trapped at 40° for the two intermediate cases and from 30° for the most brittle material. With a pore spacing of two elements, crack trapping is only partially achieved at 40° for the most ductile material and when $\varepsilon_f = 0.03$ and $G_f = 1$ mJ/mm^2, from 30° when $\varepsilon_f = 0.12$ and $G_f = 0.01$ mJ/mm^2, and from 10° for the most brittle material. For a spacing of three elements, the crack is partially trapped at 30° for the most ductile material and when $\varepsilon_f = 0.03$ and $G_f = 1$ mJ/mm^2, 20° when $\varepsilon_f = 0.12$ and $G_f = 0.01$ mJ/mm^2, and 10°–20° for the most brittle material. Crack trapping is not achieved at 40° for the most ductile material and when $\varepsilon_f = 0.03$ and $G_f = 1$ mJ/mm^2, and from 30° when $\varepsilon_f = 0.12$ and $G_f = 0.01$ mJ/mm^2 and for the most brittle material.
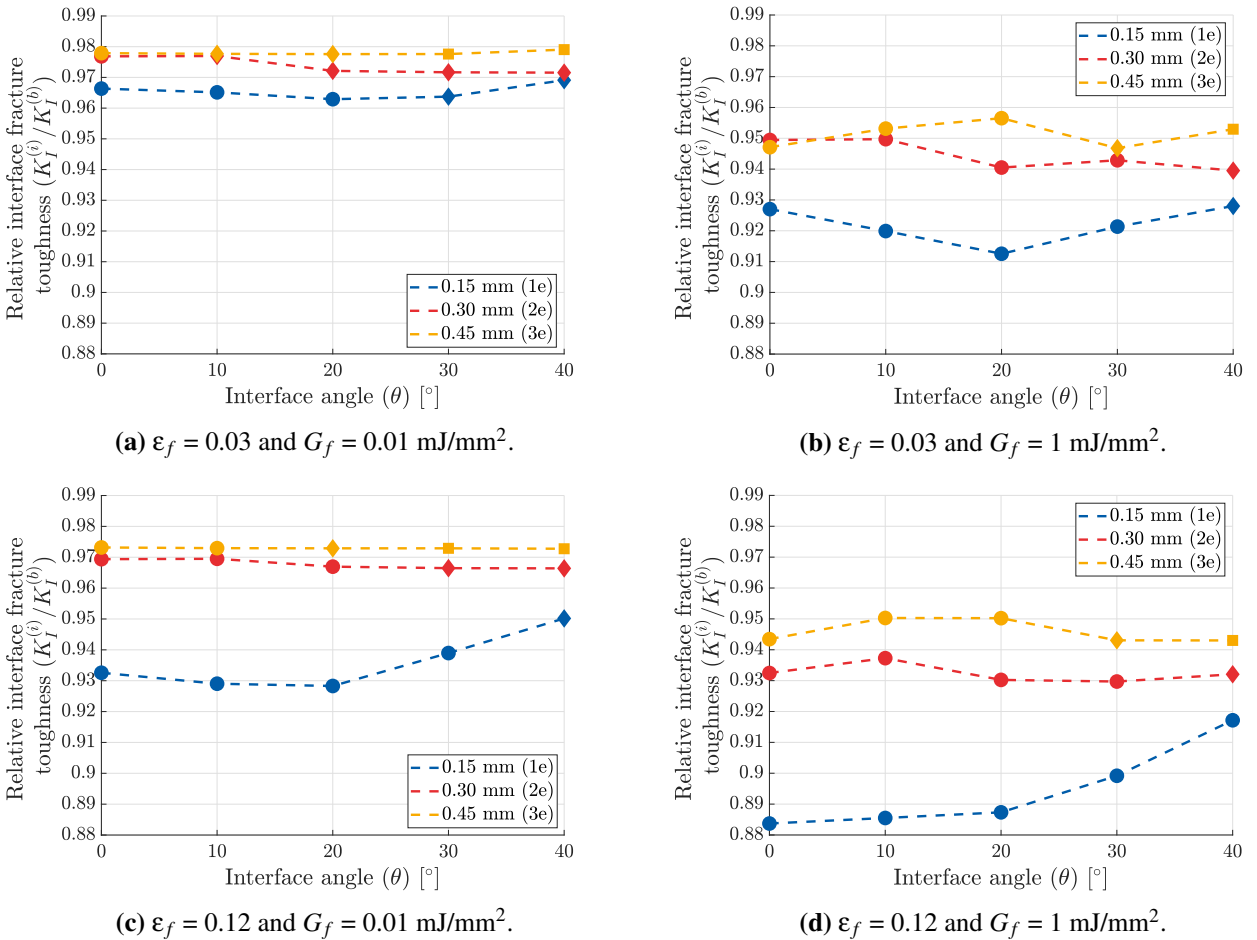

(a) $\varepsilon_f = 0.03$ and $G_f = 0.01$ mJ/mm^2.

(b) $\varepsilon_f = 0.03$ and $G_f = 1$ mJ/mm^2.

(c) $\varepsilon_f = 0.12$ and $G_f = 0.01$ mJ/mm^2.

(d) $\varepsilon_f = 0.12$ and $G_f = 1$ mJ/mm^2.

Figure 3.5: Relative interface fracture toughness as a function of the interface inclination (θ) for each combination of fracture strain (ε_f) and damage evolution energy (G_f). Consecutive pores are spaced by one, two or three elements (*i.e.*, 0.15, 0.3 or 0.45 mm respectively). The graphs reveal three distinct zones: ◯ where the crack is completely trapped, ◇ where the crack is partially trapped and □ where the crack is not trapped.

An additional data computed is the quantification of the total distance the crack follows through the interface (Fig. 3.6). First observations show that, as the interface angle increases, the proportion of crack deviation through porosity generally decreases. In addition, smaller spacing between pores (0.15 and 0.30 mm) tends to maintain higher proportions of crack deviation through porosity compared to larger spacing (0.45 mm) as the interface angle increases.

Generally speaking, the greater the pore spacing, the shorter the distance covered by the crack when the interface inclination is increased. This effect is very marked for a brittle material (Fig. 3.6a), with a significant reduction in this distance from an interface angle of 10° and a pore spacing of 0.3 mm. Specifically, the proportion of crack deviation through porosity is reduced by 96.4% at 30° and 98.5% at 40° for one element spacing; by 39.5%, 81%, 96.4% and 98% for increasing angles and two elements spacing; and by 68.7% at 10°, 95.4% at 20°, 100% at 30°–40° for increasing angles and three elements spacing. In contrast, for the more ductile material with high damage evolution energy (Fig. 3.6d), the crack propagates across the entire interface for a very large proportion of configurations. However, a 40° inclination is still challenging with only the smallest spacing that traps the crack 100% of the distance. Quantitatively, the guiding distance is reduced directly by 97.9% at 40° for two elements spacing, and by 91.3% at 30° and 100% at 40° for three elements spacing. Lastly, the two intermediate cases (Figs. 3.6b–c) exhibit behaviours that fall between those of the previously presented scenarios.

In summary, the inclination thus induces a huge drop in the proportion of porosity that the crack follows (from 100% to 0%), with a gradual decrease for the most brittle material (as shown in Figs. 3.4a–b) and with a steeper decrease in the other cases (as shown in Figs. 3.4c–e). In fact, increasing the damage evolution energy seems to enhance the crack guidance over large distances more effectively compared to an increase in fracture strain.
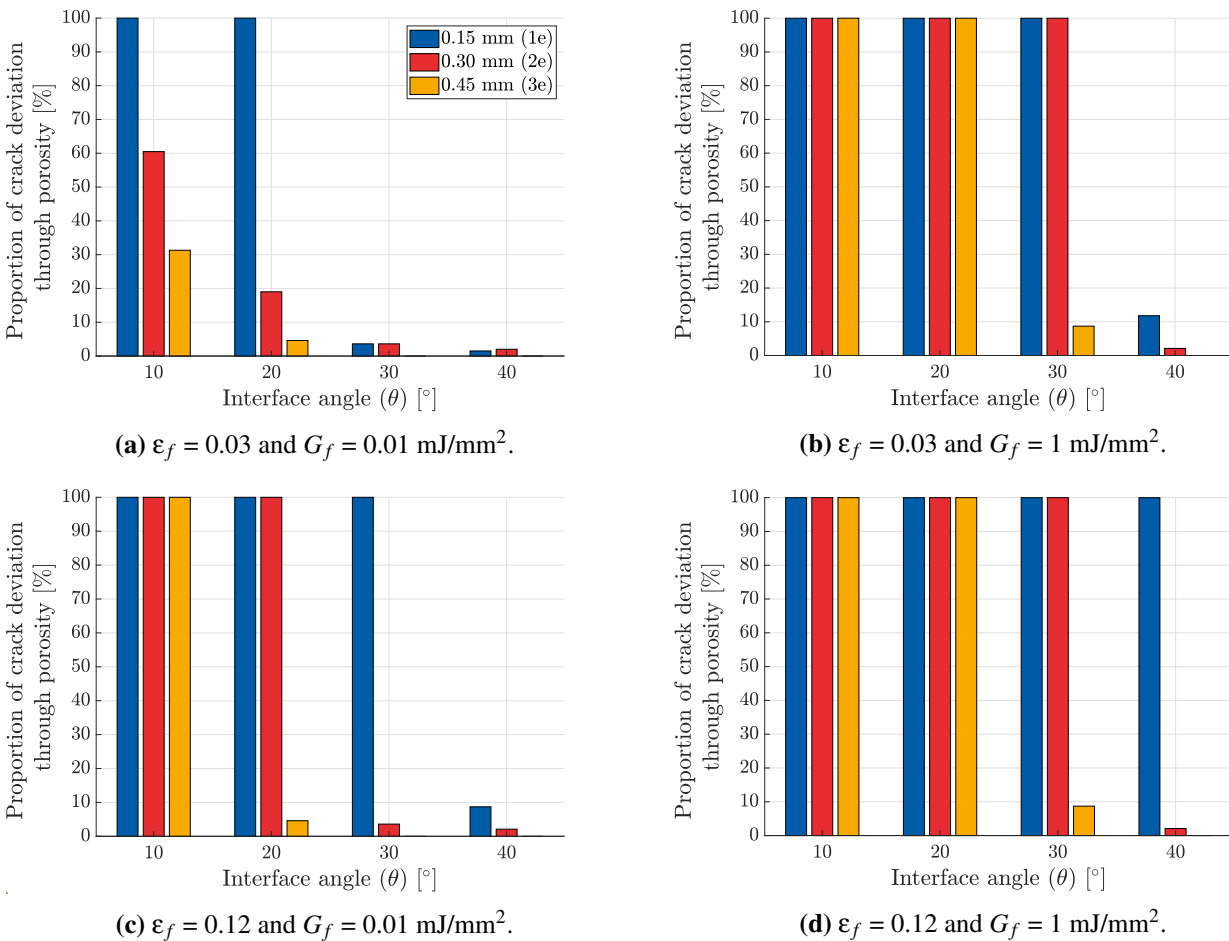

(a) $\varepsilon_f = 0.03$ and $G_f = 0.01$ mJ/mm^2.

(b) $\varepsilon_f = 0.03$ and $G_f = 1$ mJ/mm^2.

(c) $\varepsilon_f = 0.12$ and $G_f = 0.01$ mJ/mm^2.

(d) $\varepsilon_f = 0.12$ and $G_f = 1$ mJ/mm^2.

Figure 3.6: Proportion of crack deviation through the linear porosity pattern as a function of the interface inclination (θ) for each combination of fracture strain (ε_f) and damage evolution energy (G_f). Consecutive pores are spaced by one, two or three elements (*i.e.*, 0.15, 0.3 or 0.45 mm respectively), following the same colour legend as in Fig. 3.5.

3.2.3 Interplay between the weak spot and the interface

In this section, we introduce the last level of complexity, the weak spot (*i.e.*, the half-circular hole), in the model featuring the porosity pattern. Fewer inclination angles are considered to avoid direct intersection between the hole and the pattern (*i.e.*, 20°, 30° or 40°). The purpose is now to study the interplay between the weak spot and the interface under the usual fracture modelling parameters. For that, we gradually increase the spacing between successive pores (element by element) to determine the limit for each angle at which the crack no longer follows the porosity path completely.

Figs. 3.7–3.9 illustrate again three modes of crack propagation for the three investigated interface inclinations: (A) the crack is fully trapped within the interface, (B) the crack is partially attracted by the hole after partially crossing the interface, and (C) the crack is completely attracted by the hole, ignoring the interface.

Overall, regarding the fracture behaviour (indicated by different colours in the images), the same conclusions apply as those drawn for the full model. To summarise, brittle materials ($\varepsilon_f = 0.03$) show fewer blue areas compared to more ductile materials ($\varepsilon_f = 0.12$). These blue areas are typically found under the crack path when it propagates through the porous interface, and around the crack path when it goes straight to the hole. Increasing the damage evolution energy can introduce green regions, especially in materials with low fracture strain. In addition, as noted in Chapter 2, the blue and green zones tend to spread and conform to the shape of the hole as they approach it.

At a 20° interface inclination (Fig. 3.7), all parameter combinations enable to shield the hole except for the most brittle case. Even introducing the weakest plane (with a pore spacing of one element) and a small angle, the large hole has a bigger effect and still attracts the crack. Moreover, deviating a crack when $G_f = 0.01$ mJ/mm^2 is particularly challenging. Increasing the fracture strain allows complete crack deviation only with a pore spacing of one element, while a spacing of two elements allows some branching of the crack towards the hole in addition. In contrast, increasing the damage evolution energy to $G_f = 1$ mJ/mm^2 eases the pore spacing conditions to efficiently deviate the crack through the interface. Indeed, the crack can now be fully deviated by inserting a stronger/less weak interface (*i.e.*, more difficult to follow), with three elements between the pores. For a spacing of four elements, the crack partially follows the pattern before being attracted to the hole. As a result, for this inclination, hole shielding is not possible with $\varepsilon_f = 0.03$ and $G_f = 0.01$ mJ/mm^2, but achievable with the other combinations thanks to a pore spacing of one element for $\varepsilon_f = 0.12$ and $G_f = 0.01$ mJ/mm^2, and a spacing of three elements when $G_f = 1$ mJ/mm^2.

Increasing the interface inclination to 30° makes shielding the hole more difficult (Fig. 3.8). For the most brittle material, the crack does not have the possibility to follow the interface as it is directly attracted to the hole for a pore spacing of one element. Increasing the fracture strain to $\varepsilon_f = 0.12$ allows one-element spacing to still trap the crack but further spacing are no longer effective. However, when $G_f = 1$ mJ/mm^2, the crack can be fully deviated with the pore spacing of two elements, compared to three elements for a 20° inclination. As a result, increasing the interface inclination requires a less consequent spacing between the pores to ensure that the crack follows completely the pores. In other words, higher inclinations necessitate introducing weaker interfaces, which are easier to follow but may excessively weaken the material.

Finally, a 40° interface inclination is generally too steep to achieve effective hole shielding (Fig. 3.9). Only the extreme case of parameters combination (*i.e.*, $\varepsilon_f = 0.12$ and $G_f = 1$ mJ/mm^2) can effectively deviate the crack from the hole, but only with the weakest plane of pores (one-element spacing). Other parameter combinations result in the crack following a very small portion of the porosity pattern or going straight to the hole.
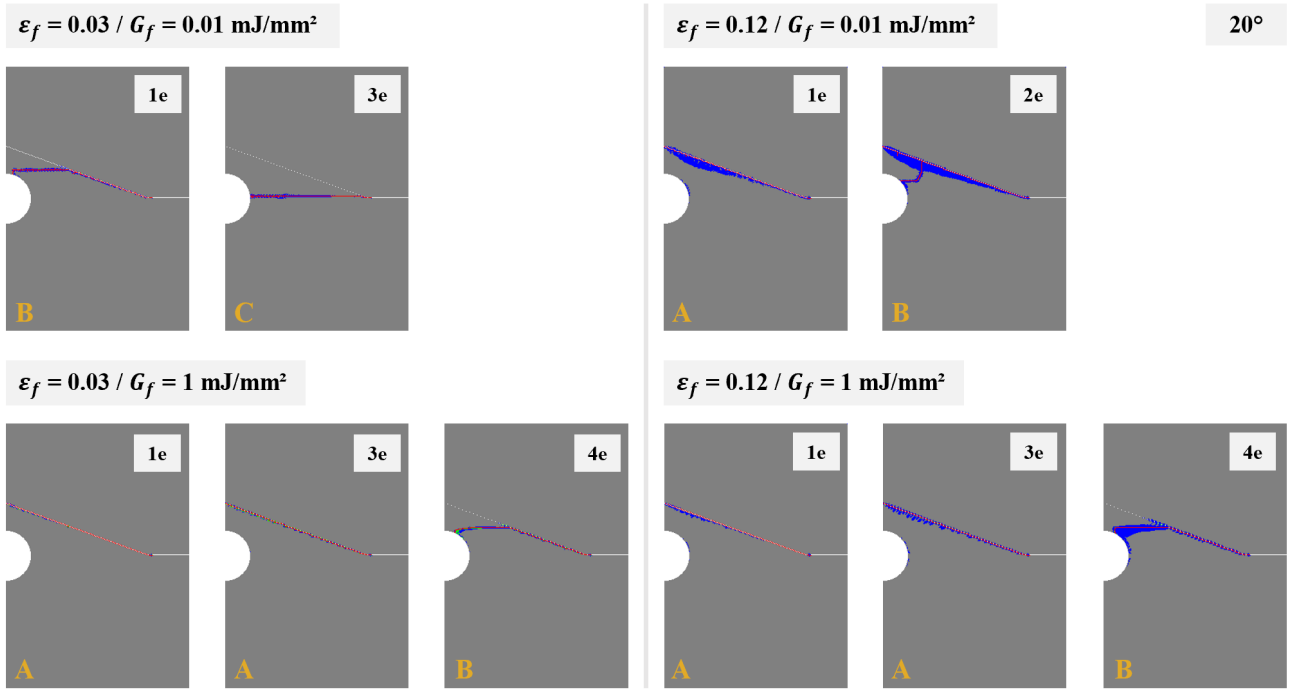
Figure 3.7: Fracture patterns of the hole model investigated for two values of fracture strain (ε_f), two values of damage evolution energy (G_f), a weak interface inclined at 20° and an initial crack length corresponding to 20% of the model width and a notch positioned at 0.15 mm. The number of elements shown in the models indicates the spacing between the pores for each case. Grey areas correspond to intact elements (DUCTCRT = 0), blue areas to damage initiation (0 < DUCTCRT < 1), green areas to damage evolution (SDEG > 0) and red areas to the crack path (SDEG = 1).
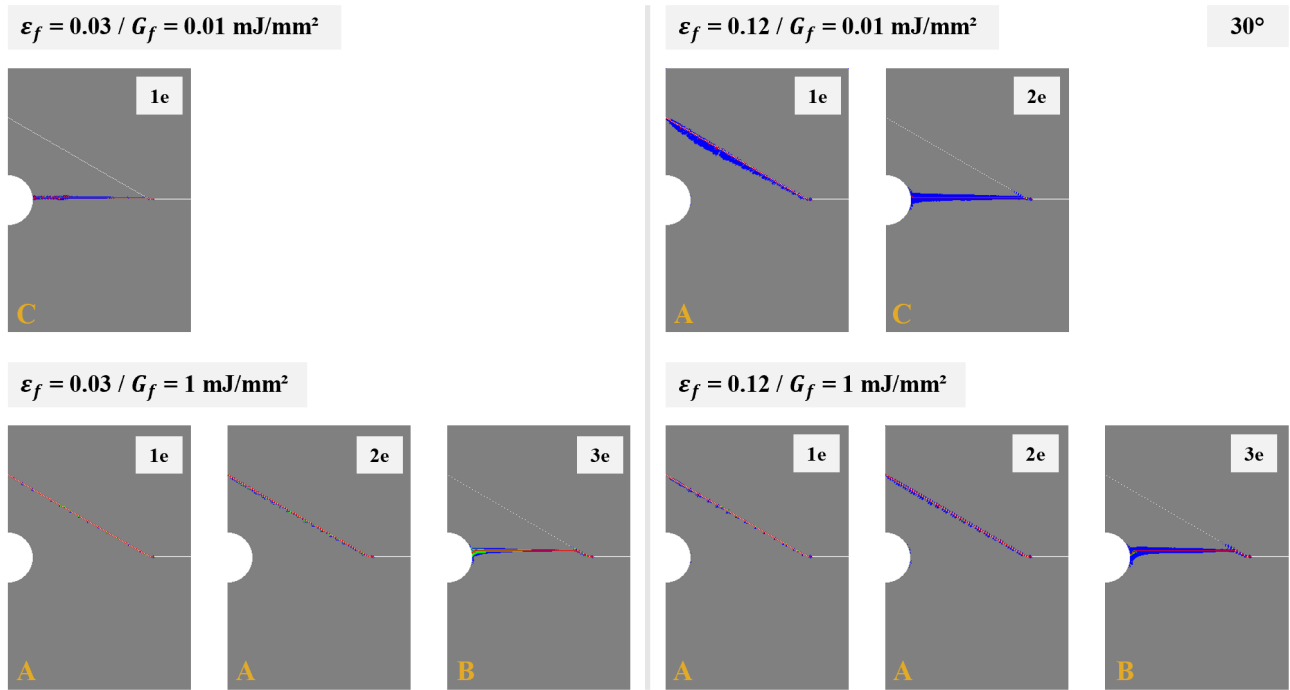

Figure 3.8: Fracture patterns of the hole model investigated for two values of fracture strain (ε_f), two values of damage evolution energy (G_f), a weak interface inclined at 30° and an initial crack length corresponding to 20% of the model width and a notch positioned at 0.15 mm. The number of elements shown in the models indicates the spacing between the pores for each case. Grey areas correspond to intact elements (DUCTCRT = 0), blue areas to damage initiation (0 < DUCTCRT < 1), green areas to damage evolution (SDEG > 0) and red areas to the crack path (SDEG = 1).
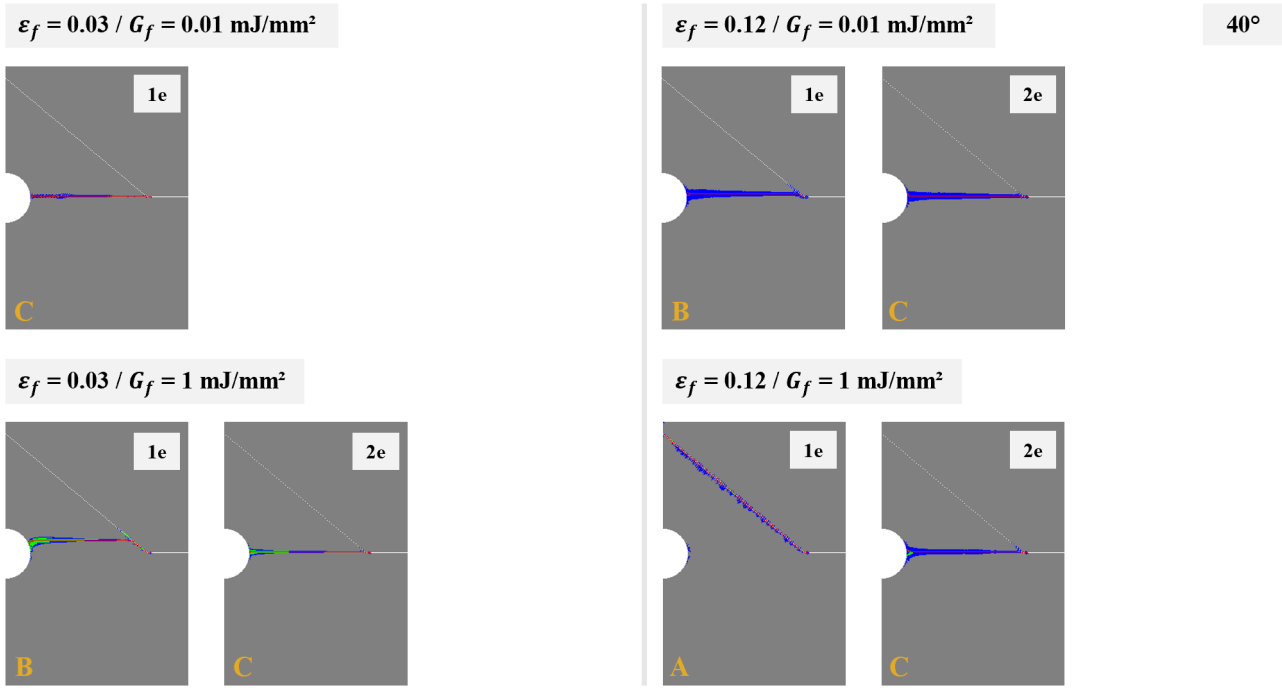
Figure 3.9: Fracture patterns of the hole model investigated for two values of fracture strain (ε_f), two values of damage evolution energy (G_f), a weak interface inclined at 40° and an initial crack length corresponding to 20% of the model width and a notch positioned at 0.15 mm. The number of elements shown in the models indicates the spacing between the pores for each case. Grey areas correspond to intact elements (DUCTCRT = 0), blue areas to damage initiation (0 < DUCTCRT < 1), green areas to damage evolution (SDEG > 0) and red areas to the crack path (SDEG = 1).

3.3   Discussion and conclusions

In this chapter, we explored the complex interactions between porosity and crack propagation across various types of material. Our simulations demonstrated that manipulating the pore spacing and the interface inclination plays a role in guiding cracks and redistributing damage within the material. Reducing the spacing in between pores generally enhanced the ability to guide cracks at the cost of weakening the material, while larger spacing and higher inclination angles reduced this guiding effectiveness.

By varying the fracture strain and damage evolution energy values, notable differences in the relative fracture toughness of the interface were observed. Particularly, the most brittle case ($\varepsilon_f = 0.03$ and $G_f = 0.01$ mJ/mm^2) behaved similarly to the bulk model, meaning that the interface is less weak (*i.e.* more difficult to break and follow) compared to materials with higher fracture strain and damage evolution energy. In addition, compared to [6], our curves in Fig. 3.3 exhibited a similar shape but started at a higher fracture toughness value (0.88 instead of 0). This difference arises because our study was constrained by element size, while F. Barthelat et al. could more freely adjust defect spacing. In theory, the fracture toughness of their entire sample depended on the size of the biggest notch. When the small defects were spaced far apart, they did not interact with each other that made the initial pre-existing notch still predominant. However, when the spacing was reduced, the small defects started to interact and effectively became more important than the single notch.

Overall, introducing a line of pores into the material decreased its fracture toughness (*i.e.*, reduces its strength or peak forces) compared to the bulk material. This finding is counterintuitive when considering strategies in biological materials (see Section 1.2) where introducing an architecture typically improves toughness. Consequently, adding only one weak interface was not enough to enhance toughness. In addition, the pores in our study seemed to be too small to significantly impact fracture toughness. Larger pore sizes (such as two-by-two elements) could be considered to increase their influence. As a result, the study suggested that the size of the introduced pores must be tailored to the material properties: more brittle materials require larger pores to guide the crack properly, while more ductile materials require smaller pores.

In addition, the introduction of the weak spot showed minimal impact compared to the full model results, the crack following more or less the same proportion of the pattern for a same pore spacing. The results indicated that our goal of shielding the hole from the crack is achievable to some extent. In particular, higher damage evolution energy improves the guidance of the crack through the weak interface. However, this observation should be taken with caution. We should bear in mind that achieving this task is initially easier with high fracture strain and high damage evolution energy, as the interface in this case is weaker and easier to follow.

In conclusion, this chapter provides valuable insights into the mechanics of crack propagation in porous materials. Future work could explore other geometric configurations for the porosity pattern and material types, to further validate and extend these findings. By doing so, the principles discovered here could be applied more broadly, potentially leading to the development of materials with tailored fracture properties for various engineering applications.

Chapter 4

Experimental validation

The final part of this thesis serves as a proof-of-concept study to support and hopefully validate computational results. To this end, selected models were fabricated using the PolyJet 3D printer available at the MBBM laboratory. Mechanical testing, specifically tensile tests, was then performed on these samples using an electromechanical testing machine. A camera system was used to record the fracture propagation patterns.

This chapter begins with a presentation of the sample designs, the chosen printing options and the followed testing procedure. Afterwards, the results of this investigation are presented and discussed.

4.1 Methods

4.1.1 Sample design

The goal of this study is to compare the behaviour of hole models with or without pores pattern inclusion at two inclinations: 20° and 30°. Preliminary test samples were printed to find out the adequate pore size and inter pores distance in accordance to the printer resolution and conditions (Fig. 4.1). Indeed, if those two parameters are chosen too small, the printer roller movement could erase the pore when it flattens the ink layer.
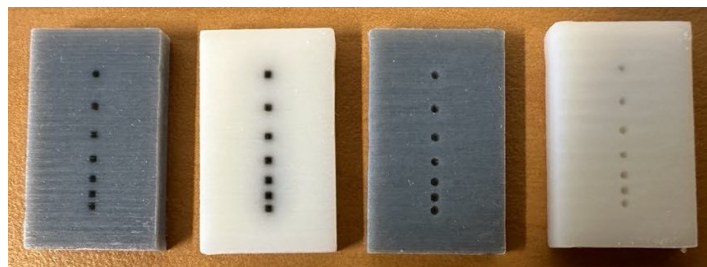

Figure 4.1: Preliminary test samples made of Grey60 or VeroWhite materials. Left: pores filled with TangoBlackPlus. Right: pores left empty.

Consequently, a square pore size of 700 μm is selected, with a pore spacing of 1 mm [81]. The notch width then matches the pore size, while the notch length is equal to 20% of the model width (*i.e.*, 7.5 mm). This notch is positioned 0.15 mm above the centre of the right boundary. An additional 15 mm (later on adjusted to 20 mm for a second batch) on both upper and down samples side have been added to allow their gripping under testing conditions. Finally, the sample thickness is set to 3.75 mm to match previously printed samples by T. Volders. All sample geometries are designed using AUTODESK FUSION 360 software and illustrated in Fig. 4.2.
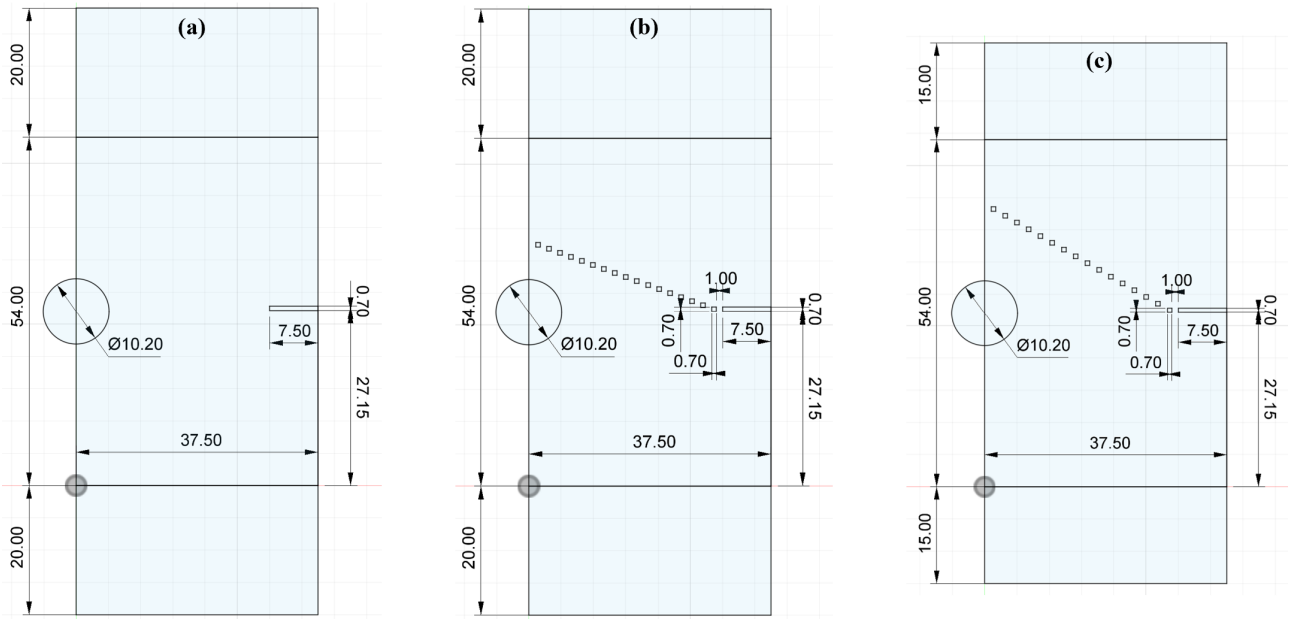
Figure 4.2: Sample designs. (a) Geometry without pores. (b) Geometry with a line of pores inclined at 20°. (c) Geometry with a line of pores inclined at 30° (with dimensions in millimetres).

4.1.2 Sample manufacturing

Samples were fabricated by a multimaterial PolyJet 3D printing (Objet Connex 260, Stratasys), a process explained in detail in Section 1.5.1. As a reminder, this technique deposits droplets of a liquid photopolymer cured by UV-light. The droplets can be of two different inks, allowing to tune the material properties within the same structure by mixing the inks if required. This research will thus use a combination of two distinct materials: VeroWhite (VW) and TangoBlackPlus (TB+). In addition, some support material will also be necessary. They are all integral components of the PolyJet materials portfolio developed by Stratasys.

The gel-like support material is specially designed to provide structural stability during the printing process. It needs to effectively hold the materials together in the desired build direction and to fill empty space that exists in the design. As a result, a notable drawback of the PolyJet printing method is the huge consumption of support material, depending on the sample complexity and printing mode. Nonetheless, the deposited support material can be easily removed post-printing by hand, using a metal scraper or through high-pressure water jet. This ensures a smooth finishing surface [82, 83].

The VW is a white opaque material that stands as a rigid polymer, offering remarkable strength and durability. Conversely, the TB+ is a black opaque material made from a soft polymer with rubber-like elastomeric properties, giving it great flexibility and elasticity [82]. Table 4.1 provides values of the most useful mechanical properties about the VW and TB+ materials. In fact, these two materials have contrasting properties, ranging from brittle-like to tough behaviour, with their respective elastic moduli varying over three orders of magnitude.

Due to the small size of the droplets, the PolyJet process has the ability to finely adjust the proportion of VW and TB+ on a voxel-by-voxel basis (*i.e.*, resolution along $x = 42\,\mu m$, $y = 84\,\mu m$, $z = 32\,\mu m$) in order to create a range of multimaterial composites known as digital materials. These materials manifest as a two-colour dithering pattern that effectively represents a blend between the mechanical properties of VW and TB+.

In our study, the samples were printed using either the rigid glassy polymer (VW) or a digital material (Grey60, called G60), which is composed of 18% TB+ and 82% VW in volume fractions and has an elastic modulus of 1190 MPa at room temperature. In fact, the Young's modulus of G60 represents an average value obtained from a large number of samples, where properties may vary due to manufacturing factors (*e.g.*, ink mixing) or testing conditions (*e.g.*, sample positioning). Using these two materials (VW or G60) allowed us to observe the impact of the pores in both brittle and ductile samples. Furthermore, the pores in the samples were left empty or filled with the rubber-like polymer (TB+).

52

	VeroWhitePlus (VW)	TangoBlackPlus (TB+)
Tensile strength	50–65 MPa	0.8–1.5 MPa
Elongation at break	10–25%	170–220%
Young's modulus	2–3 GPa	0.5–1 MPa
Shore hardness	83–86 (D)	26–28 (A)

Table 4.1: Performance specifications of the VeroWhite and TangoBlackPlus materials [68, 82].

The two batches of samples were fabricated on different trays (Figs. 4.3 and 4.4). The first printed batch aimed to compare bulk samples with samples featuring a linear pattern of empty or TB+ pores inclined at 30°. Afterwards, the goal was to test the performance of the two pore types with a 20° inclination and an increase in the size of the grips. This adjustment was necessary to ensure a secure grip in the machine, as the first G60 bulk sample has failed in this aspect. Both were printed in the vertical direction on the tray using the "matte" surface finish option, meaning that they were fully embedded in support material. This option was selected to maintain the same surface roughness across all faces of the samples. After printing, the gel-like support material was removed using a metal scraper.
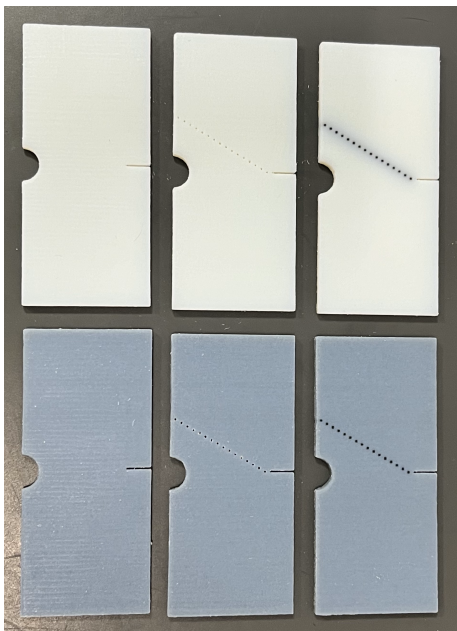

Figure 4.3: Samples before testing. Up: samples in VW. Down: samples in G60. Left: no pores. Middle: line of empty pores inclined at 30°. Right: line of pores filled with TB+ inclined at 30°.
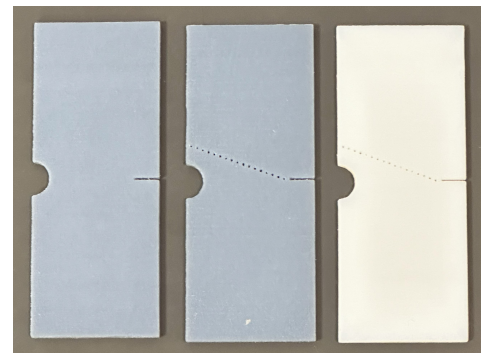

Figure 4.4: Samples before testing. Left: G60 sample without pores. Middle: G60 sample with a line of empty pores inclined at 20°. Right: VW sample with a line of empty pores inclined at 20°.

4.1.3 Sample testing

Mechanical tensile tests were performed on these notched samples using an electromechanical testing machine (MTS Criterion™ C43.304). This equipment comprises several key components including a load frame, a cross-head, a load cell, specimen grips, a drive system and a testing software. The load frame adopts a dual column configuration to withstand the applied force. The cross-head is controlled to move up or down during testing. The load cell serves as a transducer that converts the tensile force applied to the specimen into an electrical signal that can be measured. Grips and fixtures ensure a secure mechanical connection between the specimen and the machine, in order to transfer the cross-head movement to the specimen and the generated force from the specimen to the load cell. The drive system supplies the machine motor with various power levels and frequencies. The testing software enables users to set up the test methods, configure and conduct tests, and present results [84, 85].

In our study, these tests were conducted at room temperature with a cross-head displacement rate of 1 mm/min, a preload of 5 N and a load cell capacity of 30 kN. Fig. 4.5 shows the setup ready to operate, with the sample mounted on the MTS machine. All tested samples were subjected to identical loading conditions. Following the standard protocol used in the MBBM laboratory, each specimen was tested one day after printing. Fabrication, storage and testing were done in a room with controlled humidity and temperature to further minimise experimental variability.

During the tests, data on applied force and cross-head displacement were continuously recorded. In addition, the samples were imaged using a high-definition camera. The recorded movies and measured data were synchronised in time which allowed us to accurately correlate the sample behaviour with the load-displacement curves, integrating qualitative and quantitative information.
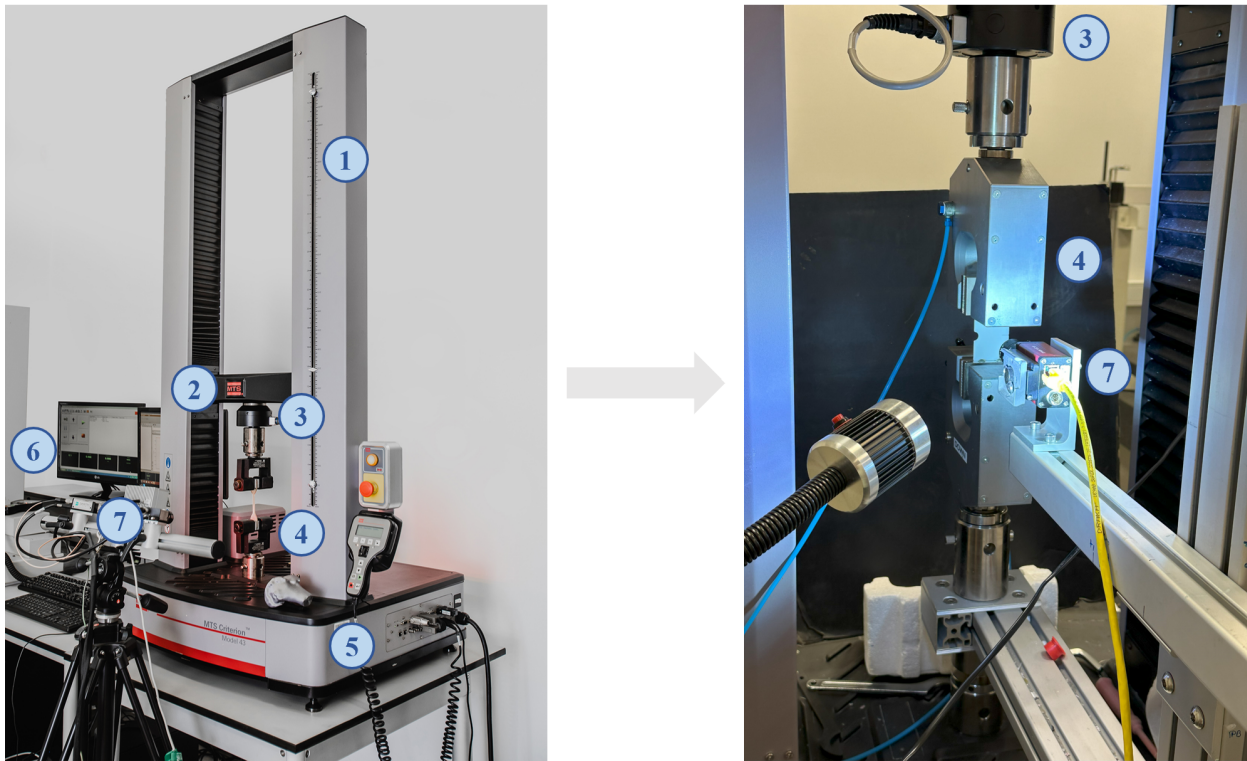

Figure 4.5: Left: universal testing machine with (1) load frame, (2) cross-head, (3) load cell, (4) grips and fixtures, (5) drive system, (6) testing software and (7) HD camera (adapted from [86]). Right: zoom on the testing area in our case.

4.2 Results

The main goal of this section of the thesis is to verify that introducing a linear pattern of pores can successfully deviate a crack from reaching the half-hole. By observing the fracture patterns in the samples after the tensile tests (Fig. 4.6), this task appears to be accomplished in several samples.

The VW and G60 samples without pores show a clean fracture with a single crack running almost directly towards the hole. Introducing a line of empty pores makes, however, the fracture more complex. For the VW samples, a 20° inclination allows the crack to deviate through the porosity until it bifurcates straight near the end. With a 30° inclination, the crack follows much less the pattern before being attracted by the hole. Filling the pores with TB+ helps to increase the distance along which the crack is trapped in the porosity pattern. For the G60 samples, linear patterns of empty pores inclined at either 20° or 30° both allow to completely deviate the crack from one side to the other. However, the pores filled with TB+ in this more ductile model tend to reduce the pattern ability to effectively guide the crack along its length.
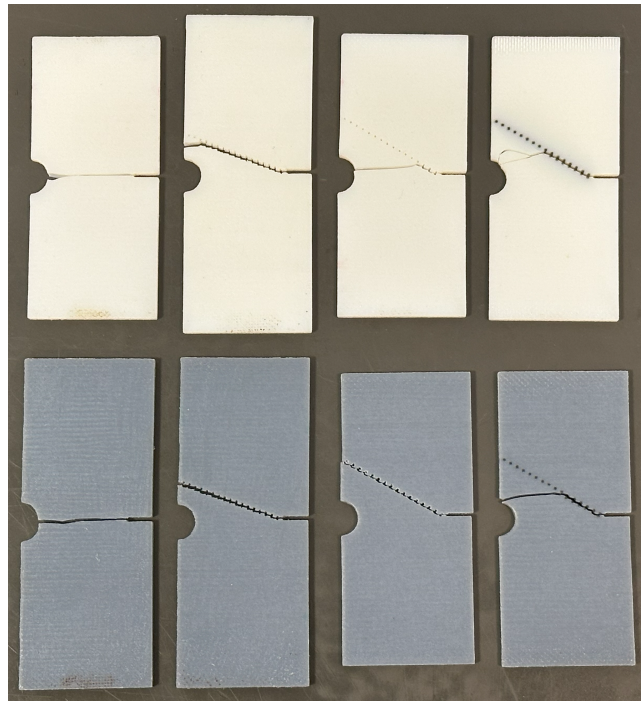
Figure 4.6: Fracture patterns after the tensile tests. Up: samples in VW. Down: samples in G60. Left: no pores. Middle: line of empty pores inclined at 20° and then 30°. Right: line of pores filled with TB+ inclined at 30°. Note that the larger samples are part of the second batch, in which the size of the grips has been increased.

Looking at the load-displacement curves (Fig. 4.7), we observe that VW samples without pores and with empty pores show an initial elastic phase characterised by a steep slope (high stiffness) before reaching a maximum load and experiencing a sudden drop, indicative of a brittle fracture. In contrast, these same G60 samples display a distinct behaviour with less steep curves (lower stiffness), lower maximum loads (except for the one without pores) but higher displacements at fracture, implying a more ductile fracture process. Notably, the G60 sample without pores behaves unusually, as it typically reaches a peak load near 950 N under tension; so its curve is excluded from this quantitative analysis. Specifically, using G60 instead of VW increases the work of fracture by 16.6% for a sample with a line of empty pores inclined at 20° and by 9.7% for a sample with a line of TB+ pores inclined at 30°, but decreases it by 19% for a sample with a line of empty pores inclined at 30°.

Moreover, for both types of materials, the presence of empty pores reduces the load-bearing capacity compared to the samples without pores. A porosity interface inclined at 20° appears to reduce the peak load and displacement at fracture more significantly than a porosity interface inclined at 30°. Quantitatively, for the VW case, the work of fracture of the bulk sample decreases by 68.5% with a 20° inclination and by only 16.5% with a 30° inclination. In addition, transitioning from a 20° to a 30° inclination increases the work of fracture by 62.3% for the VW material and 49.7% for the G60 material.

Conversely, for both materials with a 30° inclination, incorporating TB+ into the pores seems to improve the toughness as it allows to reach higher peak loads, greater ductility (indicated by a more gradual decrease in load after the peak) and a much higher displacement at fracture. For VW, this results in a 45.8% increase in the work of fracture.

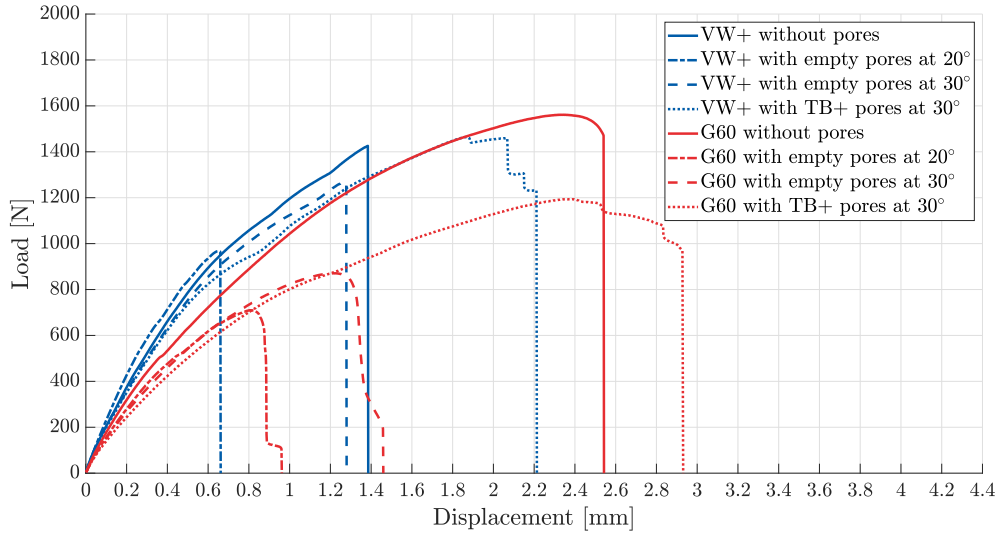These findings are supported by the observed curves and quantitatively verified by Table 4.2.

Figure 4.7: Load-displacement curves for the eight tested samples.

	Peak load [N]	Displacement at fracture [mm]	Work of fracture [mJ]
VW without pores	1426	1.38	1.226
VW with empty pores at 20°	967	0.66	0.386
VW with empty pores at 30°	1268	1.28	1.024
VW with TB+ pores at 30°	1464	2.21	2.26
G60 without pores	1561	2.54	2.749
G60 with empty pores at 20°	710	0.96	0.417
G60 with empty pores at 30°	871	1.46	0.829
G60 with TB+ pores at 30°	1193	2.93	2.503

Table 4.2: Peak load, displacement at fracture and work of fracture computed for the eight tested samples.

The load-displacement curves with their corresponding snapshots (Figs. 4.8– 4.15) clearly illustrate the fracture process of the materials under load. Each snapshot corresponds to specific points on the curve, highlighting key stages in the fracture behaviour of the samples.

In a general case, as the load is initially applied, the material undergoes elastic deformation with no visible cracks. With further increase in load, the plastic zone extends near the crack tip that leads to the initiation of a first small crack, marking the onset of fracture. This crack then propagates until it reaches a critical length at the peak load. The peak load represents the maximum stress that the material can withstand before significant cracking occurs, leading to complete material failure. Following the peak, the load drops sharply as the crack propagates fully through the sample. As a result, the main differences between the samples are in their peak load values and the extent of crack propagation, influenced by the material and pore type.

For the VW sample without pores (Fig. 4.8), there is a gradual opening of the notch (2) before a sudden brittle fracture (3). With the pattern of empty pores (Figs. 4.9 and 4.10), we can observe an extension of the plastic zone near the crack tip with a very limited crack propagation (2), since the material almost breaks instantly (3). In addition, as said before, introducing TB+ into the pores (Fig. 4.11) enhances the sample ductility, allowing for greater elastic deformation (2) and a more gradual crack propagation (3–5) until complete failure (6).

In contrast, all G60 samples (Figs. 4.12–4.15) display a more stepwise and progressive crack propagation. Initially, the notch gradually opens and then the crack slowly advances through the porosity pattern until the piece finally breaks in two. The pores appear to be more deformed in this case, which may influence the fracture dynamics.

Moreover, in both materials and with empty pores, the crack path tends to follow a staircase-like pattern, forming bridges from one pore to the next (Figs. 4.9, 4.10, 4.13 and 4.14).
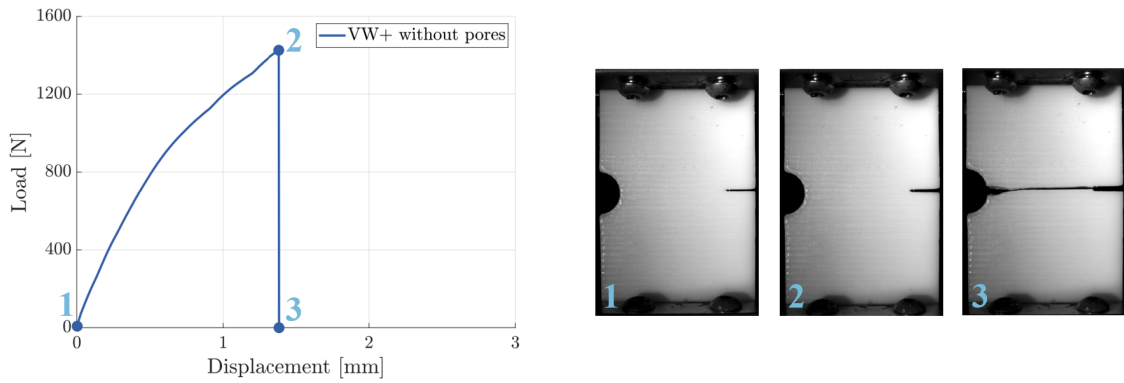

Figure 4.8: Load-displacement curves and some corresponding snapshots from the recorded video for the VW sample without pores.
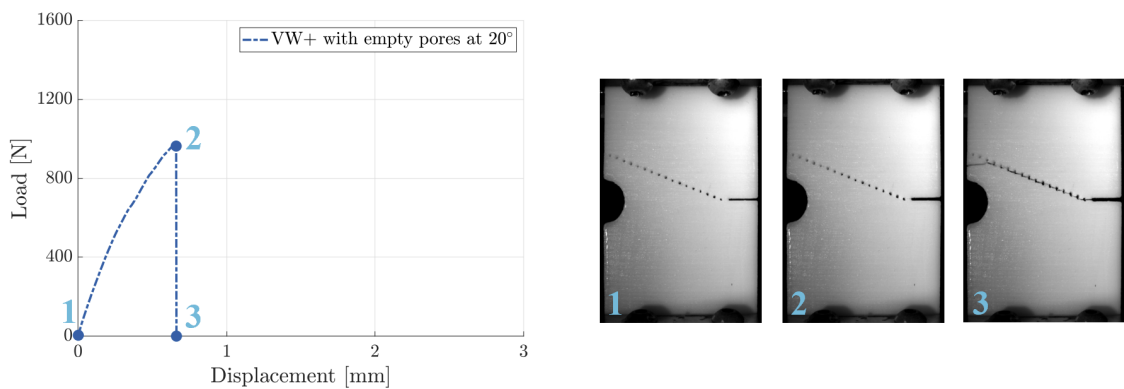

Figure 4.9: Load-displacement curves and some corresponding snapshots from the recorded video for the VW sample with a line of empty pores inclined at 20°.
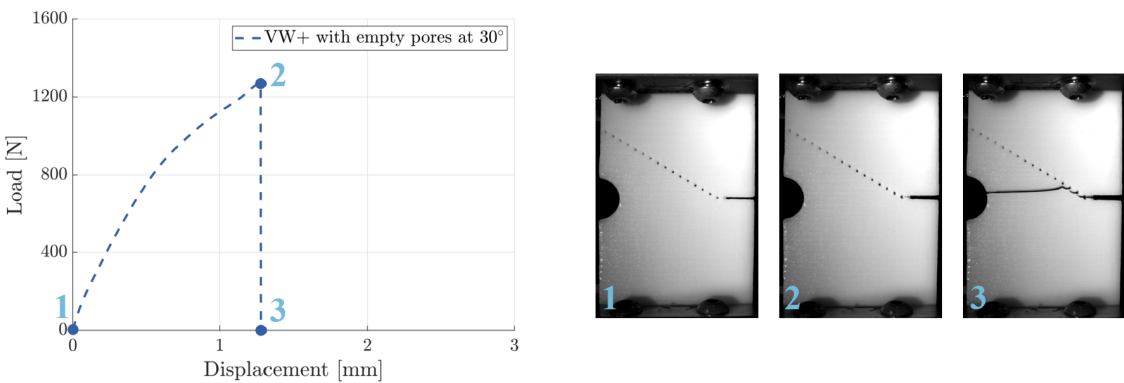

Figure 4.10: Load-displacement curves and some corresponding snapshots from the recorded video for the VW sample with a line of empty pores inclined at 30°.
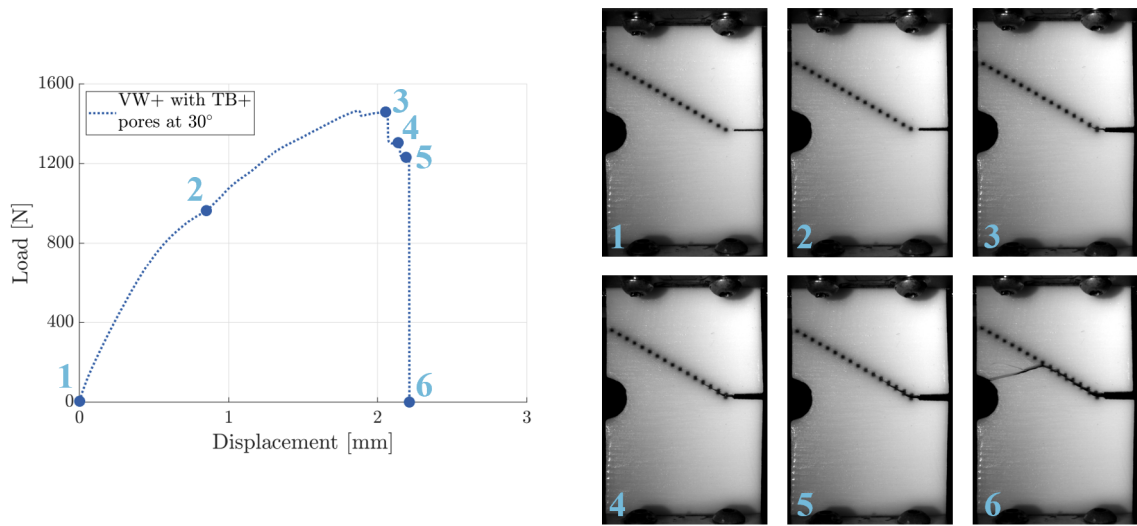
Figure 4.11: Load-displacement curves and some corresponding snapshots from the recorded video for the VW sample with a line of TB+ pores inclined at 30°.
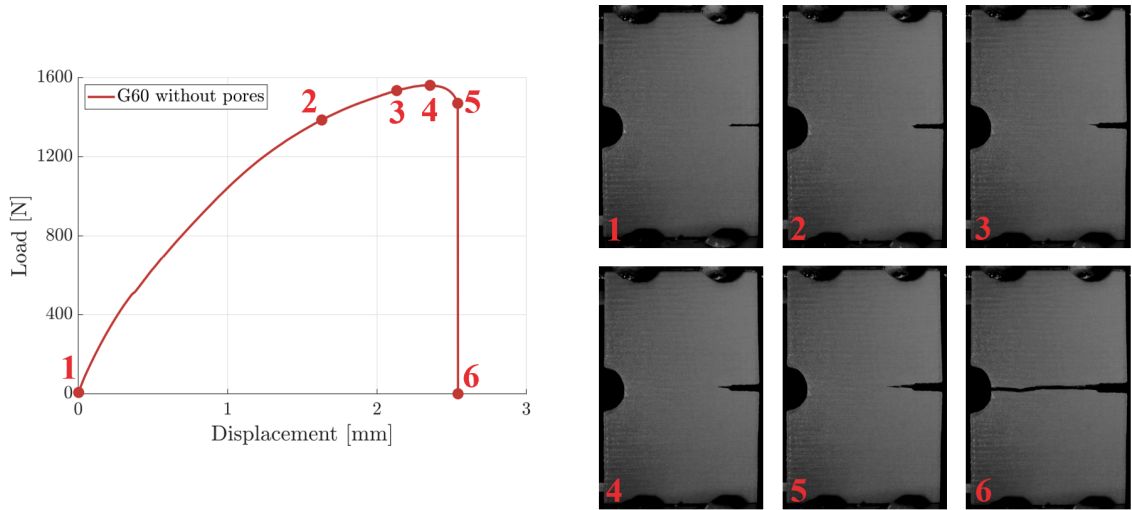

Figure 4.12: Load-displacement curves and some corresponding snapshots from the recorded video for the G60 sample without pores.

Figure 4.13: Load-displacement curves and some corresponding snapshots from the recorded video for the G60 sample with a line of empty pores inclined at 20°.
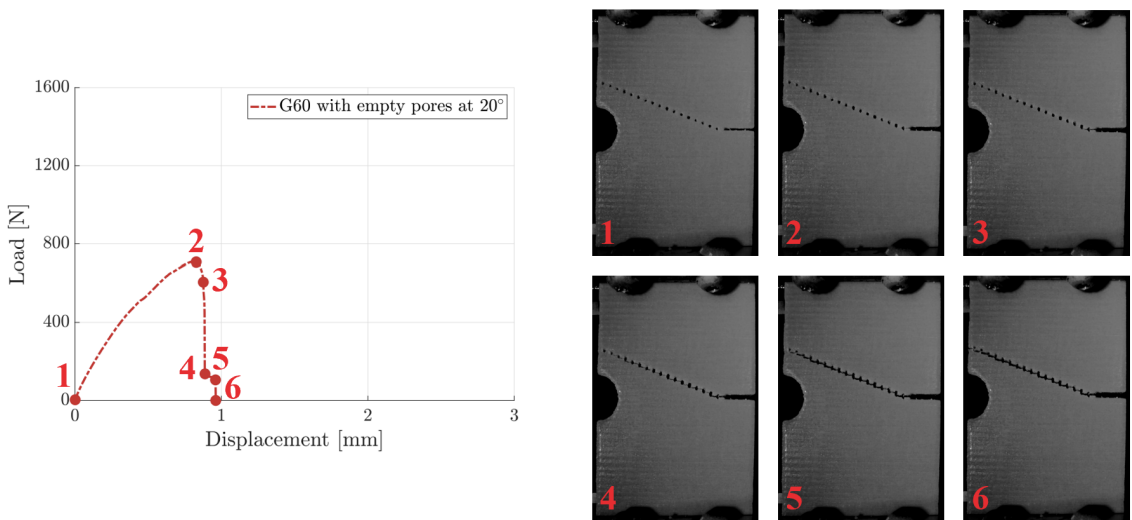
Figure 4.14: Load-displacement curves and some corresponding snapshots from the recorded video for the G60 sample with a line of empty pores inclined at 30°.

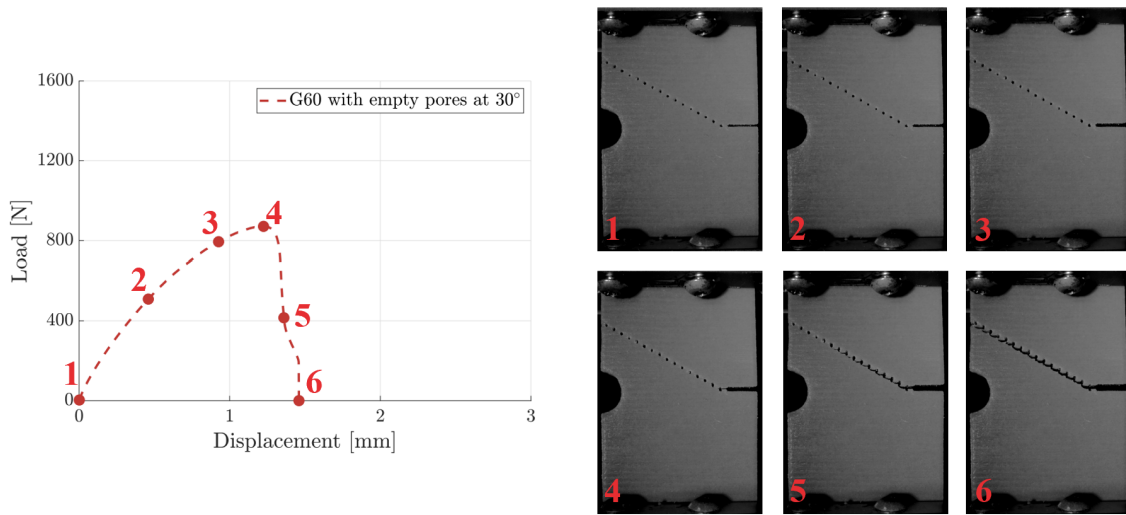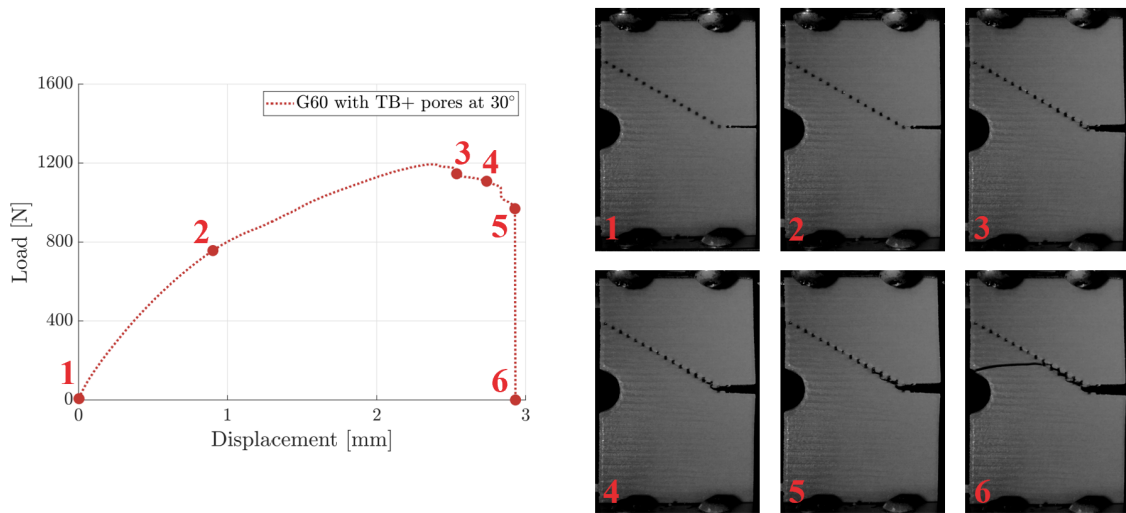

Figure 4.15: Load-displacement curves and some corresponding snapshots from the recorded video for the G60 sample with a line of TB+ pores inclined at 30°.

4.3 Discussion and conclusions

This experimental investigation seems to validate the computational predictions regarding the influence of pore patterns on the crack propagation of 3D printed samples, subjected to tensile tests.

It is first important to note that the initial tensile test for the G60 sample without pores failed, certainly due to the sample slipping between the grips. Several factors could explain this failure. One possibility is that the grip areas added to the sample design were too small to hold the sample securely. The sample could also be badly positioned in the centre of the grips, preventing them from applying maximum force. Lastly, the notch design could be too sharp, necessitating a small curvature at the corners to improve stability. Despite these potential human errors, the second sample was successfully retested with larger grips and more force applied to the grips.

Despite this, this proof-of-concept study demonstrates that the presence of a linear pattern of pores can significantly alter the fracture behaviour, with performance depending on the material used and the inclination of the porosity pattern. In the case of a brittle material (VW), we observed that the largest defect (*i.e.*, the half-circular hole) quickly dominated if the pattern inclination shifted too far away from it. The room for manoeuvre needed to effectively achieved the desired shielding effect was therefore very limited. In contrast, for a more ductile

material (G60), there was greater flexibility in the pattern angle to ensure that crack propagation was deflected. Consequently, the hole had almost no influence and was no longer felt by the crack.

Furthermore, filling the pores with TB+ had opposite effects on both types of material. For the G60 sample, having empty pores was preferable because the presence of TB+ reduced the overall ability of the pattern to trap crack propagation. A possible explanation is that the contrast in material properties between G60 and TB+ became insufficient to make the pattern effective. On the other hand, for the VW sample, the TB+ filled pores had a positive effect, helping to amplify the pattern ability to trap crack propagation. This demonstrates once again that using multimaterial architectured materials, although simple and inexpensive in terms of the amount of soft material used, can greatly improve the control over how a brittle material fractures.

In addition, the incorporation of TB+ into the pores enhanced the strength and toughness of both materials, underlying the potential of multimaterial 3D printing to locally tune mechanical properties. Conversely, the curves for empty pores showed a decrease in peak loads and displacements at fracture. Nevertheless, in a ductile material, empty pores are still preferable to TB+, because the latter reduced the material performance to deviate cracks. Indeed, it is crucial to bear in mind that the shielding of crack propagation by the porosity is a key consideration when designing the sample, as this is the main objective of the research.

These are intriguing designs that pave the way for innovative future applications. However, this study presents some limitations. The experiments were conducted with only one sample for each combination of parameters, which may not fully capture the variability and potential inconsistencies in 3D printing processes. Indeed, the mechanical properties of the printed materials, particularly digital materials like G60, can vary due to factors such as ink mixing, printing conditions and post-processing. For example, the removal of support material can introduce defects into the samples. Repeating the tests with a bigger number of samples could enhance the reproducibility and provide more robust results. Notably, we observed that the G60 bulk sample had a strange behaviour (see load-displacement curve), whereas a behaviour similar to the G60 samples with empty pores was expected. Without testing multiple samples, we cannot thus confirm that this curve represents the true trend.

Finally, the printing direction (*e.g.*, horizontal, vertical or diagonal along the same axis as the porosity) might not significantly influence the fracture pattern behaviour, especially given that we worked with monolithic material samples with pores. However, introducing TB+ into these pores might challenge this assumption, as multiple materials inside the same sample create interfaces. In addition, the printing process inherently produced an anisotropic material by constructing the piece layer by microscopic layer, which could affect the fracture behaviour. Despite this, we believe that the introduction of macroscopic defects, such as the pores, has a more substantial effect on the fracture pattern, resulting in a staircase-like defect, regardless of the printing orientation. Nonetheless, this hypothesis warrants further investigation, and it would be insightful to print samples at different orientations, such as 90° or tilted, to study their impact on the fracture behaviour.

From another perspective, future research could explore new pore designs by modifying variables such as pore size, pore patterns (including more complex patterns beyond linear arrangements) and pore spacing. Different initial notch lengths could also be considered, but they must be carefully planned in accordance with pore spacing to introduce enough pores and ensure the interface effectiveness. This approach could lead to new discoveries and further enhance the material fracture performance.

Chapter 5

Conclusion and perspectives

The main goal of this thesis was to investigate how structural and material properties influence the fracture behaviour of bio-inspired materials, with a particular focus on replicating the toughening mechanisms observed in natural materials such as bone. A particular focus was placed on understanding the effect of a porosity pattern on the interaction between a weak spot and a propagating crack, through a combination of 2D damage finite element simulations and mechanical testing of 3D-printed samples.

Firstly, an extensive parametric study revealed that variations in material properties (especially fracture strain and damage evolution energy), notch length and notch vertical position significantly affected crack propagation and fracture patterns. Specifically, higher fracture strains typically resulted in higher peak forces and displacements at fracture, underlying the role of material ductility in enhancing toughness. In addition, increasing the damage evolution energy by two orders of magnitude had less influence at a higher fracture strain value, maybe due to the high plasticity of the material.

The study also demonstrated that introducing porosity patterns within the material could effectively trap and deviate crack propagation, thereby enhancing the material ability to protect its weak spot. This effectiveness mainly depended on the inclination of the porosity interface and the distance between consecutive pores. In fact, closer pore spacing improved the ability to guide cracks at the cost of the material strength, while larger spacing and higher inclination angles reduced this crack-guiding capability. Among others, this biomimetic approach highlighted the potential of structural design to improve the fracture resistance of brittle materials.

Mechanical tests on 3D-printed samples largely supported the computational results. The samples precisely replicated the porosity pattern, adjusting pore size and spacing to match the printer resolution. The tests demonstrated that crack shielding is more effective in ductile materials than in brittle ones, and with small interface inclinations. Filling pores with an elastomeric-like material (TangoBlackPlus) also had varying effects depending on the base material. For ductile materials (Grey60), empty pores were more beneficial, whereas for more brittle materials (VeroWhite), filled pores enhanced toughness. This finding underscored the importance of material compatibility and the potential of multimaterial 3D printing to locally tune mechanical properties. However, some discrepancies, likely due to limitations in the 3D printing process, highlighted the need for further experimentation with larger sample sizes to ensure the robustness and reproducibility of these findings

The results of this thesis thus suggest several directions for future research and practical applications. Future studies could first explore more complex pore geometries and arrangements, as well as varying pore sizes and spacing, to identify optimal crack propagation pathways. Expanding the range of material properties could also potentially lead to new fracture behaviours. Then, enhancing the computational models to include more complex biological structures, involved in other toughening mechanisms, could improve their predictive accuracy and applicability. Additionally, further investigation into the effects of printing orientation on fracture behaviour is necessary. Printing samples at various angles and orientations could provide deeper insights into how anisotropy introduced by the printing process influences material performance.

In conclusion, drawing inspiration from nature ingenious designs can advance future research in the field of bio-inspired materials, leading to innovative solutions with superior mechanical performance and the development of novel damage-tolerant materials.

Appendices

Appendix A: Material property conversion

The contents of this section are sourced from [87]. It details how the material properties derived from experimental data are converted into true values for ABAQUS inputs in theory.

In general, true strain (ε) is determined by considering the limit as the change in length (Δl) approaches infinitesimally small ($\Delta l \to dl \to 0$). The associated true stress (σ) is defined as the force (F) per unit area (A) acting on a material. Mathematically, these are expressed as follows

$$d\varepsilon = \frac{dl}{l} \quad \Rightarrow \quad \varepsilon = \int_{l_0}^{l} \frac{dl}{l} = \ln \frac{l}{l_0} \quad \text{and} \quad \sigma = \frac{F}{A}, \tag{A.1}$$

where l is the current length and l_0 is the original length.

However, material test data often provide values of nominal stress and strain. In such cases, it is necessary to convert the material data from nominal to true stress and strain values using the following expressions.

The relationship between true strain and nominal strain (ε_{nom}) is found by adding unity to both sides of the expression for nominal strain and taking the natural logarithm.

$$\varepsilon_{nom} = \frac{l - l_0}{l_0} = \frac{l}{l_0} - 1 \quad \Rightarrow \quad \boxed{\varepsilon = \ln\left(1 + \varepsilon_{nom}\right)} \tag{A.2}$$

The relationship between true stress and nominal stress (σ_{nom}) is derived considering the incompressible nature of plastic deformation and assuming that the elasticity is also incompressible. The current area (A) is related to the original area (A_0) as

$$l_0 A_0 = lA \quad \Leftrightarrow \quad A = A_0 \frac{l_0}{l}. \tag{A.3}$$

Substituting this definition into the expression for true stress yields

$$\sigma = \frac{F}{A} = \frac{F}{A_0} \frac{l}{l_0} \quad \Rightarrow \quad \boxed{\sigma = \sigma_{nom}(1 + \varepsilon_{nom})} \tag{A.4}$$

Lastly, it is important to note that the strains recorded in material test data employed to define the plastic behaviour usually represent total strains in the material. These total strain values (ε^t) need to be decomposed into elastic (ε^{el}) and plastic strain (ε^{pl}) components. The plastic strain is thus obtained by subtracting the elastic strain, which is calculated as the true stress divided by the Young's modulus (E), from the total strain.

$$\boxed{\varepsilon^{pl} = \varepsilon^t - \varepsilon^{el} = \varepsilon^t - \frac{\sigma}{E}} \tag{A.5}$$

As illustrated in Fig. A.1, ABAQUS approximates the stress-strain behaviour of the material by connecting the provided data points with straight lines.
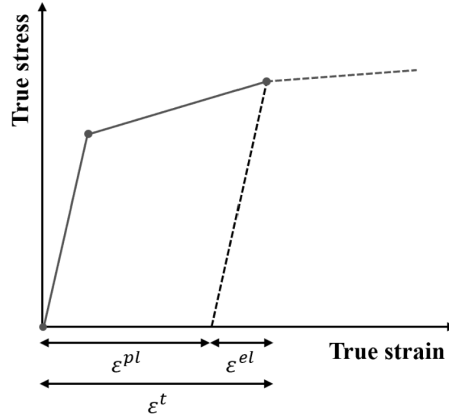
Figure A.1: True stress-strain behaviour with the decomposition of the total strain.

Appendix B: Porosity introduction - Ellipse case

As mentioned earlier in Chapter 3, an alternative method for creating a pattern of pores involves following a segment of an ellipse (Fig. A.2). This approach is applied to the full model, which is a rectangle with dimensions of $H = 54$ mm (height) and $W = 37.5$ mm (width), including a pre-existing notch. The same material and notch parameters used for the linear pattern are employed here. The ellipse on which porosity is grafted has a major axis of $2a = 120$ mm and a minor axis of $2b = 53.7$ mm (Fig. A.3). Although these dimensions are arbitrarily chosen, the centre of the ellipse must be on the upper boundary of the model. This has been implemented using an extension of the previous MATLAB code with the mathematical function provided in Eq. (A.6).

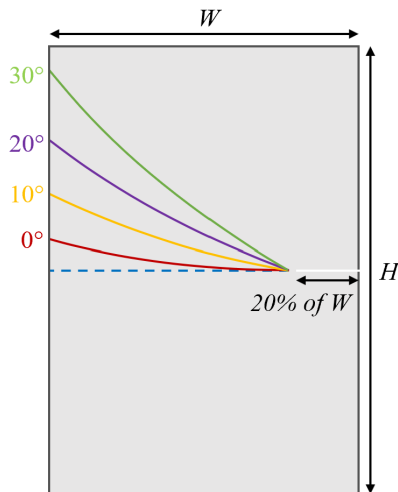$$\frac{x^2}{a^2} + \frac{y^2}{b^2} = 1 \tag{A.6}$$

Figure A.2: Model geometry. Porosity is arranged along an elliptical pattern rotated at angles of 0°, 10°, 20° or 30°.
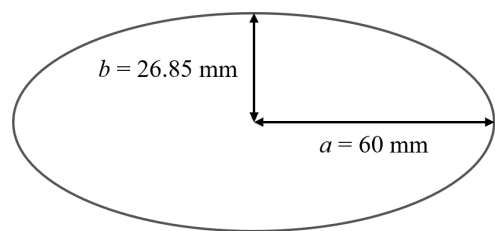

Figure A.3: Ellipse definition.

In this second more innovative approach, a total of 39 simulations were conducted. Each simulation typically requires an average of 3 hours of CPU time, depending mainly on the fracture strain and damage evolution energy values. Fig. A.4 illustrates four fracture patterns corresponding to different combinations of fracture strain and damage evolution energy across four different interface angles. The goal is to demonstrate that with an alternative porosity pattern, the crack can also be trapped and guided in a different direction. However, due to time constraints, further analysis is needed to extract clear key messages and potentially evaluate its better performance against a linear pattern.
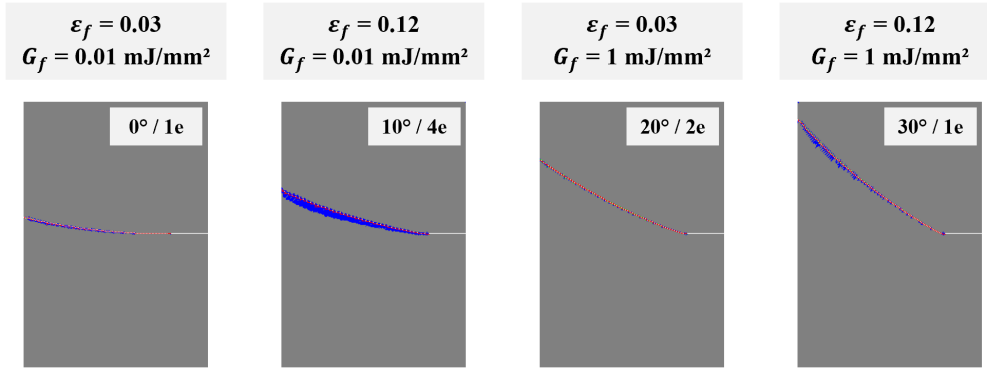
Figure A.4: Fracture patterns of the full model investigated for two values of fracture strain (ε_f), two values of damage evolution energy (G_f), four interface inclinations and an initial crack length corresponding to 20% of the model width and a notch positioned at 0.15 mm. The number of elements shown in the models indicates the spacing between consecutive pores. Grey areas correspond to intact elements (DUCTCRT = 0), blue areas to damage initiation (0 < DUCTCRT < 1), green areas to damage evolution (SDEG > 0) and red areas to the crack path (SDEG = 1).

Appendix C: Porosity interface toughness study
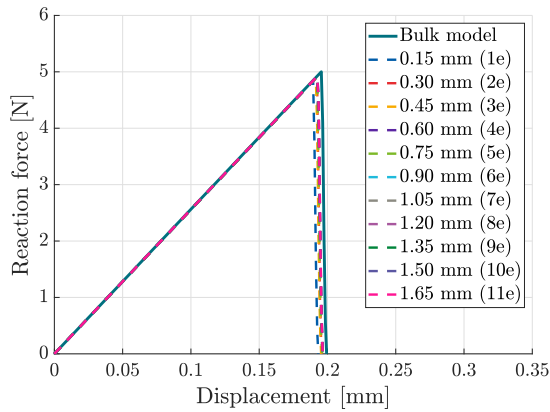
(a) $\varepsilon_f = 0.03$ and $G_f = 0.01$ mJ/mm^2.
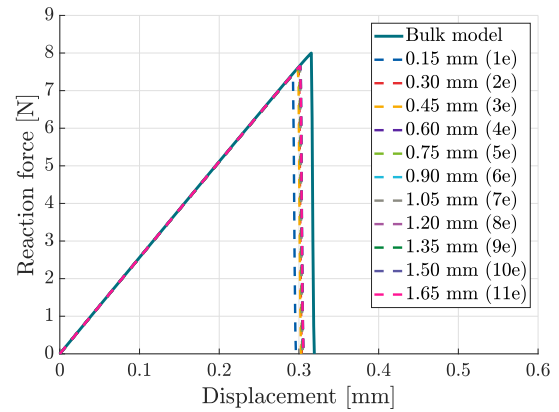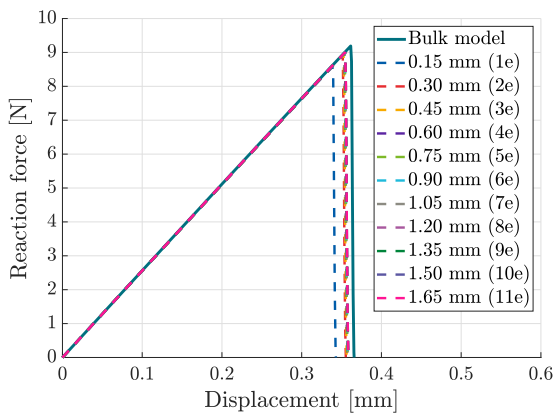
(b) $\varepsilon_f = 0.03$ and $G_f = 1$ mJ/mm^2.

(c) $\varepsilon_f = 0.12$ and $G_f = 0.01$ mJ/mm^2.
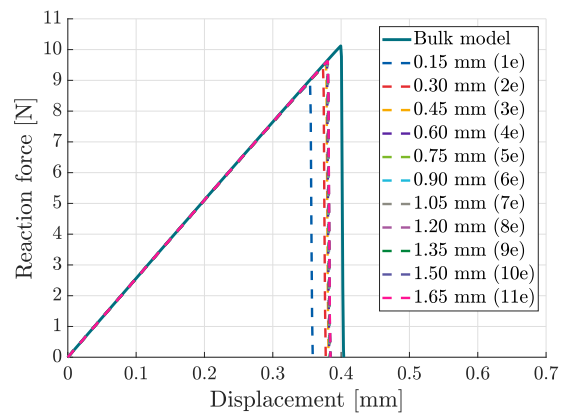
(d) $\varepsilon_f = 0.12$ and $G_f = 1$ mJ/mm^2.

Figure A.5: Reaction force vs. displacement curves for each combination of fracture strain (ε_f) and damage evolution energy (G_f). Comparison between the bulk model and models including a porosity interface inclined at 0°. Consecutive pores are spaced by one to eleven elements (*i.e.*, 0.15 to 1.65 mm respectively).

Bibliography

[1] U.G.K. Wegst, H. Bai, E. Saiz, A.P. Tomsia and R.O. Ritchie, *Bioinspired structural materials*. Nature Materials, **14**(1) (2015), pp. 23–36.

[2] P-Y. Chen, A.Y.M. Lina, Y-S. Linb, Y. Sekia, A.G. Stokesb, J. Peyrasa, E.A. Olevskyc, M.A. Meyersa and J. McKittrick, *Structure and mechanical properties of selected biological materials*. Journal of the Mechanical Behavior of Biomedical Materials, **1**(3) (2008), pp. 208–226.

[3] R.O. Ritchie, *The conflicts between strength and toughness*. Nature Materials, **10** (2011), pp. 817–822.

[4] F. Donaldson, D. Ruffoni, P. Schneider, A. Levchuk, A. Zwahlen, P. Pankaj and R. Müller, *Modeling microdamage behavior of cortical bone*. Biomechanics and Modeling in Mechanobiology, **13**(6) (2014), pp. 1227–1242.

[5] B.L. Smith, T.E. Schaeffer, M. Viani, J.B. Thompson, N.A. Frederick, J. Kindt, A. Belcher, G.D. Stuckyk, D.E. Morse and P.K. Hansma, *Molecular mechanistic origin of the toughness of natural adhesives, fibres and composites*. Nature, **399**(673) (1999), pp. 761–763.

[6] M. Mirkhalaf, A. Khayer Dastjerdi and F. Barthelat, *Overcoming the brittleness of glass through bio-inspiration and micro-architecture*. Nature Communications, **5** (2014), 3166.

[7] D. Ruffoni, *GBIO0012-2 Biomechanics – Chapter: Bones*. University of Liège, (2022-2023).

[8] B. Clarke, *Normal bone anatomy and physiology*. Clinical Journal of the American Society of Nephrology, **3** (2008), pp. S131–S139.

[9] T.L.N. Järvinen, H. Sievänen, J. Jokihaara and T.A. Einhorn, *Revival of bone strength: the bottom line*. Journal of Bone and Mineral Research, **20**(5) (2005), pp. 717–720.

[10] R.S. Taichman, *Blood and bone: two tissues whose fates are intertwined to create the hematopoietic stem-cell niche*. Blood, **105**(7) (2005), pp. 2631–2639.

[11] P. Fratzl, H.S. Gupta, E.P. Paschalis and P. Roschger, *Structure and mechanical quality of the collagen-mineral nano-composite in bone*. Journal of Materials Chemistry, **14** (2004), pp. 2115–2123.

[12] P. Fratzl and R. Weinkamer, *Nature's hierarchical materials*. Progress in Materials Science, **52**(8) (2007), pp. 1263–1334.

[13] C.R. Jacobs, *The mechanobiology of cancellous bone structural adaptation*. Journal of rehabilitation research and development, **37**(2) (2000), pp. 209–216.

[14] S.H. Ralston, *Bone structure and metabolism*. Elsevier - Medicine, **41**(10) (2013), pp. 581–585.

[15] P. Augat and S. Schorlemmer, *The role of cortical bone and its microstructure in bone strength*. Age and Ageing, **35**(S2) (2006), pp. ii27–ii31.

[16] F.F. Safadi, M.F. Barbe, S.M. Abdelmagid, M.C. Rico, R.A. Aswad, J. Litvin and S.N. Popoff, *Bone structure, development and bone biology*. Humana Press, (2009), pp. 1–50.

[17] P.G. Bullough, *Atlas of orthopedic pathology: with clinical and radiologic correlations*. New York - Gower Medical Publishing, (1992).

[18] J.D. Currey, *Bones: Structure and Mechanics*. Princeton University Press, (2002).

[19] E.F. Eriksen, D.W. Axelrod and F. Melsen, *Bone histomorphometry*. New York - Raven Press, (1994), pp. 1–12.

[20] J. Duro-Royo, K. Zolotovsky, L. Mogas-Soldevila, S. Varshney, N. Oxman, M.C. Boyce and C. Ortiz, *MetaMesh: A hierarchical computational model for design and fabrication of biomimetic armored surfaces*. Computer-Aided Design, **60** (2015), pp. 14–27.

[21] W. Wagermaier, H.S. Gupta, A. Gourrier, M. Burghammer, P. Roschger and P. Fratz, *Spiral twisting of fiber orientation inside bone lamellae*. Biointerphases, **1** (2006), pp. 1–5.

[22] S. Weiner, W. Traub and H.D. Wagner, *Lamellar bone: structure-function relations*. Journal of Structural Biology, **126**(3) (1999), pp. 241–255.

[23] A.J. Hodge and J.A. Petruska, *Recent studies with the electron microscope on ordered aggregates of the tropocollagen molecule*. G.N. Ramachandran Ed., Aspects of Protein Structure, Academic Press, New York (1963), pp. 289–300.

[24] K.E. Kadler, D.F. Holmes, J.A. Trotter and J.A. Chapman, *Collagen fibril formation*. Biochemical Journal, **316** (1996), pp. 1–11.

[25] W.J. Landis, *The strength of a calcified tissue depends in part on the molecular structure and organization of its constituent mineral crystals in their organic matrix*. Bone, **16**(5) (1995), pp. 533–544.

[26] J-Y. Rho, L. Kuhn-Spearing and P. Zioupos, *Mechanical properties and the hierarchical structure of bone*. Medical Engineering & Physics, **20** (1998), pp. 92–102.

[27] M.E. Launey, M.J. Buehler and R.O. Ritchie, *On the mechanistic origins of toughness in bone*. Annual Review of Materials Research, **40** (2010), pp. 25–53.

[28] H. Peterlik, P. Roschger, K. Klaushofer and P. Fratzl, *From brittle to ductile fracture of bone*. Nature Materials, **5**(1) (2006), pp. 52–55.

[29] R.O. Ritchie, *Mechanisms of fatigue crack propagation in metals, ceramics and composites: Role of crack tip shielding*. Materials Science and Engineering - A, **103**(1) (1988), pp. 15–28.

[30] M.E. Launey and R.O. Ritchie, *On the fracture toughness of advanced materials*. Advanced Materials, **21**(20) (2009), pp. 2103–2110.

[31] G.E. Fantner, T. Hassenkam, J.H. Kindt, J.C. Weaver, H. Birkedal, L. Pechenik, J.A. Cutroni, G.A.G. Cidade, G.D. Stucky, D.E. Morse and P.K. Hansma, *Sacrificial bonds and hidden length dissipate energy as mineralized fibrils separate during bone fracture*. Nature Materials, **4**(8) (2005), pp. 612–616.

[32] R.O. Ritchie, *Mechanisms of fatigue-crack propagation in ductile and brittle solids*. International Journal of Fracture, **100** (1999), pp. 55–83.

[33] K.J. Koester, J.W. Ager III and R.O. Ritchie, *The true toughness of human cortical bone measured with realistically short cracks*. Nature Materials, **7**(8) (2008), pp. 672–677.

[34] R.K. Nalla, J.S. Stölken, J.H. Kinney and R.O. Ritchie, *Fracture in human cortical bone: local fracture criteria and toughening mechanisms*. Journal of Biomechanics, **38**(7) (2005), pp. 1517–1525.

[35] E.A. Zimmermann, M.E. Launey, H.D. Barth and R.O. Ritchie, *Mixed-mode fracture of human cortical bone*. Biomaterials, **30**(29) (2009), pp. 5877–5884.

[36] G.P. Parsamian and T.L. Norman, *Diffuse damage accumulation in the fracture process zone of human cortical bone specimens and its influence on fracture toughness*. Journal of materials science - Materials in medicine, **12**(9) (2001), pp. 779–783.

[37] H. Alijani and T.J. Vaughan, *Exploring the hierarchical structure of lamellar bone and its impact on fracture behaviour: A computational study using a phase field damage model*. Journal of the Mechanical Behavior of Biomedical Materials, **153** (2024), 106471.

[38] R.K. Nalla, J.J. Kruzic and R.O. Ritchie, *On the origin of the toughness of mineralized tissue: microcracking or crack bridging?*. Bone, **34**(5) (2004), pp. 790–798.

[39] J.D. Currey and J.D. Taylor, *The mechanical behavior of some molluscan hard tissues*. Journal of Zoology, **173**(3) (1974), pp. 395–406.

[40] M. Rousseau, E. Lopez, P. Stempflé, M. Brendlé, L. Franke, A. Guette, R. Naslain and X. Bourrat, *Multiscale structure of sheet nacre*. Biomaterials, **26**(31) (2005), pp. 6254–6262.

[41] M. Sarikaya and I.A. Aksay, *Biomimetics, Design and Processing of Materials. Polymers and Complex Materials*. American Institute of Physics, (1995).

[42] H.D. Espinosa, J.E. Rim, F. Barthelat and M.J. Buehler, *Merger of structure and material in nacre and bone – Perspectives on de novo biomimetic materials*. Progress in Materials Science, **54** (2009), pp. 1059–1100.

[43] M.A. Meyers, P-Y. Chen, A. Yu-Min Lin, Y. Seki, *Biological materials: Structure and mechanical properties*. Progress in Materials Science, **53**(1) (2008), pp. 1–206.

[44] U.G.K. Wegst and M. Ashby, *The mechanical efficiency of natural materials*. Philosophical Magazine, **84**(21) (2004), pp. 2167–2186.

[45] M.A. Meyers and P-Y. Chen, *Biological Materials Science*. Cambridge University Press, (2014).

[46] F. Barthelat, H. Tang, P.D. Zavattieri, C.M. Li and H.D. Espinosa, *On the mechanics of mother-of-pearl: A key feature in the material hierarchical structure*. Journal of the Mechanics and Physics of Solids, **55**(2) (2007), pp. 306–337.

[47] M.A. Meyers, A. Yu-Min Lin, P-Y. Chen and J. Muyco, *Mechanical strength of abalone nacre: role of the soft organic layer*. Journal of the mechanical behavior of biomedical materials, **1**(1) (2008), pp. 76–85.

[48] F. Barthelat and R. Rabiei, *Toughness amplification in natural composites*. Journal of the Mechanics and Physics of Solids, **59**(4) (2011), pp. 829–840.

[49] A.G. Evans, Z. Suo, R.Z. Wang, I.A. Aksay, M.Y. He and J.W. Hutchinson, *Model for the robust mechanical behavior of nacre*. Journal of Materials Research, **16**(9) (2001), pp. 2475–2484.

[50] F. Song and Y. Bai, *Effects of nanostructures on the fracture strength of the interfaces in nacre*. Journal of Materials Researchs, **18**(8) (2003), pp. 1741–1744.

[51] M. Sarikaya, H. Fong, N. Sunderland, B.D. Flinn, G. Mayer, A. Mescher and E. Gaino, *Biomimetic model of a sponge-spicular optical fiber—mechanical properties and structure*. Journal of Materials Research, **16**(5) (2001), pp. 1420–1428.

[52] T. Saito, I. Uchida and M. Takeda, *Skeletal growth of the deep-sea hexactinellid sponge Euplectella oweni, and host selection by the symbiotic shrimp Spongicola japonica (Crustacea: Decapoda: Spongicolidae)*. Journal of Zoology, **258**(4) (2006), pp. 521–529.

[53] J. Aizenberg, J.C. Weaver, M.S. Thanawala, V.C. Sundar, D.E. Morse and P. Fratzl, *Skeleton of Euplectella sp.: structural hierarchy from the nanoscale to the macroscale*. Science, **309**(5732) (2005), pp. 275–278.

[54] H. Chai, J. J-W Lee, P.J. Constantino, P.W. Lucas and B.R. Lawn, *Remarkable resilience of teeth*. Proceedings of the National Academy of Sciences of the United States of America, **106**(18) (2009), pp. 7289–7293.

[55] M. Yahyazadehfar, D. Bajaj and D.D. Arola, *Hidden contributions of the enamel rods on the fracture resistance of human teeth*. Acta Biomaterialia, **9**(1) (2013), pp. 4806–4814.

[56] A.R. Studart, *Biological and bioinspired composites with spatially tunable heterogeneous architectures*. Advanced Functional Materials, **23** (2013), pp. 4423–4436.

[57] V. Imbeni, J.J. Kruzic, G.W. Marshall, S.J. Marshall and R.O. Ritchie, *The dentin-enamel junction and the fracture of human teeth*. Nature Materials, **4**(3) (2005), pp. 229–232.

[58] J.J. Kruzic, R.K. Nalla, J.H. Kinney and R.O. Ritchie, *Crack blunting, crack bridging and resistance-curve fracture mechanics in dentin: effect of hydration*. Biomaterials, **24**(28) (2003), pp. 5209–5221.

[59] A.E. Vellwock and F. Libonati, *XFEM for composites, biological, and bioinspired materials: A Review*. Materials, **17** (2024), 745.

[60] S. Li, A. Abdel-Wahab, E. Demirci and V.V. Silberschmidt, *Fracture process in cortical bone: X-FEM analysis of microstructured models*. International Journal of Fracture, **184** (2013), pp. 43–55.

[61] D. Yin, B. Chen and S. Lin, *Finite element analysis on multi-toughening mechanism of microstructure of osteon*. Journal of the Mechanical Behavior of Biomedical Materials, **117** (2021), 104408.

[62] Z. Zhang, K. Zheng, E. Li, W. Li, Q. Li and M.V. Swain, *Mechanical benefits of conservative restoration for dental fissure caries*. Journal of the Mechanical Behavior of Biomedical Materials, **53** (2016), pp. 11–20.

[63] Y. Zhang, Y. Liu, Y. She, Y. Liang, F. Xu and C. Fang, *The effect of endodontic access cavities on fracture resistance of first maxillary molar using the extended finite element method*. Journal of Endodontics, **45**(3) (2019), pp. 316–321.

[64] H. Razi, J. Predanb, F.D. Fischerc, O. Kolednikd and P. Fratzl, *Damage tolerance of lamellar bone*. Bone, **130** (2020), 115102.

[65] S. Yin, H. Chen, R. Yang, Q. He, D. Chen, L. Ye, Y-W. Mai, J. Xu and R.O. Ritchie, *Tough nature-inspired helicoidal composites with printing-induced voids*. Cell Reports Physical Science, **1** (2020), 100109.

[66] R. Udroiu and I.C. Braga, *Polyjet technology applications for rapid tooling*. MATEC Web of Conferences, **112** (2017), 03011.

[67] A.H. Espera, J.R.C. Dizon, Q. Chen and R.C. Advincula, *3D-printing and advanced manufacturing for electronics*. Progress in Additive Manufacturing, (2019).

[68] D. Ruffoni, *MECA0516-1 Mechanical properties of biological and bioinspired materials*. University of Liège, (2023-2024).

[69] SMG3D - Commercial 3D printers & additive manufacturing solutions, *Objet260 CONNEX2 3D Printer*. `https://www.smg3d.co.uk/#undefined2` (accessed February 29, 2024).

[70] M. Lang, S. Hirner, F. Wiesbrock and P. Fuch, *A review on modeling cure kinetics and mechanisms of photopolymerization*. Polymers, **14** (2022), 2074.

[71] F. Libonati, G.X. Gu, Z. Qin, L. Vergani and M.J. Buehler, *Bone-inspired materials by design: Toughness amplification observed using 3D printing and testing*. Advanced Engineering Materials, **18** (2016), no. 8.

[72] G. Grezzana, H-C. Loh, Z. Qin, M.J. Buehler, A. Masic and F. Libonati, *Probing the role of bone lamellar patterns through collagen microarchitecture mapping, numerical modeling, and 3D-printing*. Advanced Engineering Materials, **22** (2020), 2000387.

[73] F. Libonati, V. Cipriano, L. Vergani and M.J. Buehler, *Computational framework to predict failure and performance of bone-inspired materials*. ACS Biomaterials Science & Engineering, **3**(12) (2017), pp. 3236–3243.

[74] L.S. Dimas, G.H. Bratzel, I. Eylon and M.J. Buehler, *Tough composites inspired by mineralized natural materials: Computation, 3D printing, and testing*. Advanced Functional Materials, **23**(36) (2013), pp. 4629–4638.

[75] G.X. Gu, F. Libonati, S.D. Wettermark and M.J. Buehler, *Printing nature: Unraveling the role of nacre's mineral bridges*. Journal of the mechanical behavior of biomedical materials, **76** (2017), pp. 135–144.

[76] L. Zorzetto and D. Ruffoni, *Wood-inspired 3D-printed helical composites with tunable and enhanced mechanical performance*. Advanced Functional Materials, **29**(1) (2019), 1805888.

[77] G. Hunter, L. Djumas, L. Brassart and A. Molotnikov, *Controlling failure regimes in brick-and-mortar structures*. Extreme Mechanics Letters, **51** (2021), 101596.

[78] J.P. Ponthot, *MECA0036-2 Finite Element Method*. University of Liège, (2022-2023).

[79] F. Li, H. Yuan and H. Liu, *Implementation of metal ductile damage criteria in Abaqus FEA*. Journal of Physics: Conference Series, **1906** (2021), 012058.

[80] Abaqus Version 6.6 Documentation, *19.2 Damage and failure for ductile metals*. `https://classes.engineering.wustl.edu/2009/spring/mase5513/abaqus/docs/v6.6/books/usb/default.htm` (accessed March 9, 2024).

[81] L. Zorzetto and D. Ruffoni, *Wood-inspired 3D-printed helical composites with tunable and enhanced mechanical performance*. Advanced Functional Materials, **29**(1) (2019), 1805888.

[82] Stratasys – Support Center. `https://support.stratasys.com/en` (accessed February 25, 2024).

[83] R. Tomar and F. Ulu, *Investigation of digital computer aided design assembly and tessellation effects on digital ABS part quality in polyjet-3D additive printing*. Conference: SAMPE 18 - Long Beach, (2018).

[84] Instron, *Tensile testing - An introduction*. `https://www.instron.com/en-us/resources/test-types/tensile-test` (accessed March 13, 2024).

[85] Zwick/Roell, *Tensile testing machines and testers*. `https://www.zwickroell.com/products/static-materials-testing-machines/universal-testing-machines-for-static-applications/tensile-tester/` (accessed March 13, 2024).

[86] Silesian University of Technology - Department of Biomechatronics, *Strength of materials laboratory - MTS Criterion model 43*. `https://www.polsl.pl/rib3/en/laboratory/strength-of-materials-laboratory/mts-criterion-model-43/` (accessed March 13, 2024).

[87] Abaqus Version 6.5 Documentation, *10.2 Plasticity in ductile metals*. `https://classes.engineering.wustl.edu/2009/spring/mase5513/abaqus/docs/v6.5/books/gsa/default.htm?startat=ch10s02.html` (accessed March 9, 2024).